Magnetic induction healing of thermoplastic elastomer composites : Multi-physics characterization

Pablo Griffiths Alfaro

N°d'ordre NNT : 2022LYSEI061

THESE de DOCTORAT DE L'UNIVERSITE DE LYON
opérée au sein de
l'Institut National des Sciences Appliquées de Lyon

Ecole Doctorale N° 34
Matériaux de Lyon

Spécialité/ discipline de doctorat : Matériaux

Soutenance prévue le 30/06/2022, par :
Pablo Griffiths

Magnetic induction healing of thermoplastic elastomer composites: multi-physics characterization

---

Devant le jury composé de :

Schmidt, Annette	Professeur	University of Köln	Rapporteure
Beaugnon, Eric	Professeur	Université Grenoble Alpes	Rapporteur
Creton, Costantino	Directeur de recherche	ESPCI Paris	Examinateur
Genix, Anne Caroline	Maître de conférences HDR	Université de Montpellier	Examinatrice
Meille, Sylvain	Professeur	INSA Lyon	Directeur de thèse
Baeza, Guilhem	Maître de conférences	INSA Lyon	Co-directeur de thèse
Coativy, Gildas	Maître de conférences	INSA Lyon	Examinateur
Méchin, Françoise	Chargée de recherche	INSA Lyon	Examinatrice

Département FEDORA – INSA Lyon - Ecoles Doctorales

SIGLE	ECOLE DOCTORALE	NOM ET COORDONNEES DU RESPONSABLE
CHIMIE	**CHIMIE DE LYON** **https://www.edchimie-lyon.fr** Sec. : Renée EL MELHEM Bât. Blaise PASCAL, 3e étage secretariat@edchimie-lyon.fr	**M. Stéphane DANIELE** C2P2-CPE LYON-UMR 5265 Bâtiment F308, BP 2077 43 Boulevard du 11 novembre 1918 69616 Villeurbanne **directeur@edchimie-lyon.fr**
E.E.A.	**ÉLECTRONIQUE, ÉLECTROTECHNIQUE, AUTOMATIQUE** **https://edeea.universite-lyon.fr** Sec. : Stéphanie CAUVIN Bâtiment Direction INSA Lyon Tél : 04.72.43.71.70 secretariat.edeea@insa-lyon.fr	**M. Philippe DELACHARTRE** INSA LYON Laboratoire CREATIS Bâtiment Blaise Pascal, 7 avenue Jean Capelle 69621 Villeurbanne CEDEX Tél : 04.72.43.88.63 **philippe.delachartre@insa-lyon.fr**
E2M2	**ÉVOLUTION, ÉCOSYSTÈME, MICROBIOLOGIE, MODÉLISATION** **http://e2m2.universite-lyon.fr** Sec. : Bénédicte LANZA Bât. Atrium, UCB Lyon 1 Tél : 04.72.44.83.62 secretariat.e2m2@univ-lyon1.fr	**Mme Sandrine CHARLES** Université Claude Bernard Lyon 1 UFR Biosciences Bâtiment Mendel 43, boulevard du 11 Novembre 1918 69622 Villeurbanne CEDEX **sandrine.charles@univ-lyon1.fr**
EDISS	**INTERDISCIPLINAIRE SCIENCES-SANTÉ** **http://ediss.universite-lyon.fr** Sec. : Bénédicte LANZA Bât. Atrium, UCB Lyon 1 Tél : 04.72.44.83.62 secretariat.ediss@univ-lyon1.fr	**Mme Sylvie RICARD-BLUM** Institut de Chimie et Biochimie Moléculaires et Supramoléculaires (ICBMS) - UMR 5246 CNRS - Université Lyon 1 Bâtiment Raulin - 2ème étage Nord 43 Boulevard du 11 novembre 1918 69622 Villeurbanne Cedex Tél : +33(0)4 72 44 82 32 **sylvie.ricard-blum@univ-lyon1.fr**
INFOMATHS	**INFORMATIQUE ET MATHÉMATIQUES** **http://edinfomaths.universite-lyon.fr** Sec. : Renée EL MELHEM Bât. Blaise PASCAL, 3e étage Tél : 04.72.43.80.46 infomaths@univ-lyon1.fr	**M. Hamamache KHEDDOUCI** Université Claude Bernard Lyon 1 Bât. Nautibus 43, Boulevard du 11 novembre 1918 69 622 Villeurbanne Cedex France Tél : 04.72.44.83.69 **hamamache.kheddouci@univ-lyon1.fr**
Matériaux	**MATÉRIAUX DE LYON** **http://ed34.universite-lyon.fr** Sec. : Yann DE ORDENANA Tél : 04.72.18.62.44 yann.de-ordenana@ec-lyon.fr	**M. Stéphane BENAYOUN** Ecole Centrale de Lyon Laboratoire LTDS 36 avenue Guy de Collongue 69134 Ecully CEDEX Tél : 04.72.18.64.37 **stephane.benayoun@ec-lyon.fr**
MEGA	**MÉCANIQUE, ÉNERGÉTIQUE, GÉNIE CIVIL, ACOUSTIQUE** **http://edmega.universite-lyon.fr** Sec. : Stéphanie CAUVIN Tél : 04.72.43.71.70 Bâtiment Direction INSA Lyon mega@insa-lyon.fr	**M. Jocelyn BONJOUR** INSA Lyon Laboratoire CETHIL Bâtiment Sadi-Carnot 9, rue de la Physique 69621 Villeurbanne CEDEX **jocelyn.bonjour@insa-lyon.fr**
ScSo	**ScSo*** **https://edsciencessociales.universite-lyon.fr** Sec. : Mélina FAVETON INSA : J.Y. TOUSSAINT Tél : 04.78.69.77.79 melina.faveton@univ-lyon2.fr	**M. Christian MONTES** Université Lumière Lyon 2 86 Rue Pasteur 69365 Lyon CEDEX 07 **christian.montes@univ-lyon2.fr**

*ScSo : Histoire, Géographie, Aménagement, Urbanisme, Archéologie, Science politique, Sociologie, Anthropologie

Résumé

Au cours du XXe siècle, les polymères se sont développés à une vitesse très importante, due à leur facilité de production et à leur versatilité, permettant le développement de différentes classes de matériaux suivant l'application visée. En raison de leur popularité, la production de polymères a entraîné une énorme quantité de déchets. En particulier, les élastomères vulcanisés ont récemment souffert d'une mauvaise réputation à cause de leur incapacité à être refondus ou réutilisés. Sur de longues périodes, leur dégradation mécanique se fait par des sollicitations cycliques et l'effet de l'environnement. Cependant, ils restent très largement utilisés dans plusieurs secteurs industriels en raison de leurs propriétés physiques uniques. Un défi majeur consiste donc à trouver des matériaux alternatifs capables d'être réutilisés, réparés et recyclés, répondant à des exigences très élevées en termes de module d'élasticité, de ténacité, de résistance à l'usure, de stabilité chimique et de coût.

Les élastomères thermoplastiques, basés sur des copolymères à blocs multiples, possèdent les propriétés mécaniques requises pour des applications structurelles et peuvent être réutilisés ou recyclés. La réparation de ces matériaux est possible, au-dessus de leur température de fusion, à travers la dissociation des segments rigides, qui déclenche la transition solide-liquide. Nous proposons d'atteindre cette température en chargeant une matrice élastomère thermoplastique avec des (nano)particules générant de la chaleur par induction magnétique à haute fréquence, pour un traitement thermique rapide et sans contact.

D'abord, la caractérisation multi-physique a permis une compréhension complète des mécanismes agissant sur le composite sous un champ magnétique oscillatoire. Ensuite, la capacité de réparation de ces matériaux a été évaluée, en étudiant leur comportement mécanique via des expériences de traction uniaxiale jusqu'à leur rupture. Finalement, l'optimisation du processus de cicatrisation magnétique a été effectuée afin de maximiser la récupération des propriétés mécaniques et minimiser les défauts structurels induits.

Contents

Contents

Contents

List of Figures

List of Tables

General Introduction

Context

Over the 20th century, polymers have become essential in a wide range of domains. On top of the economic advantages of their production, their versatile nature allows for the tuning of different classes of polymers according to the intended application. Because of their popularity, the immense amount of polymer produced has subsequently led to an unprecedented generation of waste. In particular, elastomers, whose vulcanization process provides unrivalled mechanical properties, have recently suffered from a bad reputation for being one of the prominent materials in waste generation on land and in the oceans, because they are incapable of flowing and thus, they cannot be reshaped or reused. This is the case for tires, shoe soles, seals and wire sheaths whose inevitable disintegration happens through cyclic solicitations and environmental degradation over long periods of time. The production of elastomers shall remain of the utmost importance in several industrial sectors because of their unique physical properties. A major challenge resides therefore in finding an alternative solution capable of being reused, repaired and recycled, satisfying highly demanding requirements in terms of modulus, toughness, wear resistance, chemical stability and cost.

Research has recently been oriented towards the development of different reusable materials. Self-healing materials are appealing to both scientific community and industrial companies for their ability to repair themselves, recovering a relevant part of their mechanical properties after damage. However, their mechanic properties (post-healing strength in the range 10^3-10^7 Pa), their chemical endurance (sensible to humidity) and time needed for this recovery (10^2-10^6 s) present a limit to this approach. Therefore, on top of the material's capacity to heal, a new solution should also satisfy specific mechanics and processing requirements.

Strong and phase-changing thermoplastic elastomers (such as thermoplastic polyurethanes TPUs) possess the mechanical properties required for structural applications (*i.e.*, high strength and toughness in service) and are capable of being reused or recycled through their thermoreversible characteristics. The repairing of these materials is possible through the dissociation of semi-crystalline hard-segments encompassed within the soft matrix, enabling chain diffusion and the subsequent healing of the material through the macroscopic solid-to-liquid transition. Cooling down the material at service temperature allows for the hard-segments

to gather back from the liquid state providing solid-like properties. This dual behavior eases the processing of thermoplastic elastomers and enables their reuse, repair, and recycling.

While this phenomenon is most often controlled through resistive heating, in this thesis, we propose to use magnetic induction as an alternative stimulus offering fast, controlled, contactless, and localized heating. Induction heating requires the use of magnetic particles as fillers and originates from different magnetic relaxation mechanisms that depend on the particles' nature, size, as well as on the viscosity of the environment surrounding them. Through this study, we seek to understand and optimize the healing of magnetic composite materials, made of commercially available products.

Magnetic induction heating is often associated with biomedical research fields for applications in cancer treatment through therapeutic hyperthermia, due to the aforementioned advantages. Triggering the solid-to-liquid phase transition of magneto-responsive thermoplastic rubbers is a process which remains to be optimized for healing or post-processing treatment. As the heating mechanisms depends on the content of particles in the composite, on the properties of the magnetic particles as well as on those of the matrix surrounding them, a thorough multi-physics study is needed.

Objectives of the PhD

The primary objective of this thesis is to the produce and characterize magnetic composite materials made of a thermoplastic elastomer matrix filled with magnetic (nano)particles. The multi-physics characterization (*i.e.*, microstructural, mechanical, rheological and magnetic) should lead to a full understanding of the composite's behavior under an oscillatory magnetic field. A particular attention should be paid on the comprehension of the magnetic heating mechanisms at the origin of heat generation depending on the magnetic particles (content, nature, size…) and their interaction with the polymer matrix. The composites will be subjected to an alternating magnetic field to reach the range of temperature needed for triggering the solid-to-liquid transition. Then, the mechanical behavior of the composites will be determined through uniaxial tensile experiments on native tensile dumbbell-shaped samples and samples healed through magnetic induction after being cut in two halves. The stress/strain curves will be measured up to the mechanical failure, which will be used to evaluate the mechanical recovery between native and healed samples. With the project being conceived for upscaling to

the industry level, another objective lies in the optimization of the magnetic healing to maximize the recovery of mechanical properties, and minimize structural defects.

Scientific content

This thesis is part of the POMMADE (POlyMer MAterials inDuction hEaling) project was funded by the Institut Carnot Ingénierie@Lyon, involving the collaboration of three laboratories in Lyon, France: "Matériaux: Ingénierie et Science" (MATEIS), "Ingénierie des Matériaux Polymères" (IMP) and "Laboratoire Génie Electrique et Ferroélectricité" (LGEF). The thesis work was mainly conducted at MATEIS laboratory within the "Polymères, Verres et Matériaux Hétérogènes" (PVMH) team. Because of the multi-physics nature of this work, collaborations were also built up with different research laboratories such as "Institut des Nanotechnologies de Lyon" (INL), "Institut Lumière Matière" (ILM) and European Synchrotron Radiation Facility (ESRF).

The introduction of magnetic induction heating to the MATEIS laboratory has led to multiple new projects. Through the previous years, student projects, internships and post-doctoral fellowships have relied on magnetic induction and its advantages for heat generation and for sensing particular structural changes. The works on supramolecular superparamagnetic nanocomposites (Falco *et at.*, *Macromolecules*, 2020), on anisotropic ferromagnetic composites (Xiang *et al.*, *Materials Today Chemistry*, 2021) and on magneto-responsive metallo-supramolecular networks (Jiang *et al*., *Macromolecules*, 2022 – recently accepted) are notable collaborations. It should then be noted that forthcoming PhD thesis are expected to treat subjects related to magnetic induction heating.

The manuscript starts with a **Literature Review** (Chapter I) describing the main applications and characteristics of thermoplastic elastomers, the basic concepts of magnetism and induction heating, and the state of the art regarding induction heating on polymer-based nanocomposites, as these are the fundamental concepts for understanding this work. Chapter II focuses on the description of the **Materials & Methods**. The experimental results on the **Structure & Thermomechanics of Composites** are presented in Chapter III, detailing the structural, thermal, and rheological behavior, setting the conditions for an efficient repair of the samples. Then, the materials are subjected to **Magnetic Induction Heating** (Chapter IV) and selected formulations are subjected to different **Magnetic Induced Treatments** (Chapter V). Finally, we characterize the **Movement in the Molten State** (Chapter VI) of the magnetic particles

under induction heating, clarifying the fundamental understanding of our material's response to the alternating magnetic field. The manuscript is completed by a **General Conclusions** section gathering the results and the possible outlooks of this work.

Note that the main results presented in Chapters III-V have been recently published as an article (Griffiths *et al.*, "Ultrafast Remote Healing of Magneto-Responsive Thermoplastic Elastomer-Based Nanocomposites", *Macromolecules*, 2022). On top of this, a patent has been submitted in December 2020 (under revision at the time of writing), on the process of repairing a structural defect through magnetic induction healing, illustrated in Chapter V.

Chapter I: Literature Review

Contents

This chapter introduces the fundamental aspects required for a full understanding of the present thesis. First, we will introduce thermoplastic elastomers, some aspects of their structure-properties relationship and their main applications. Then, we will describe the basics of magnetic behavior, the different types of magnetism and the heating mechanisms appearing under an oscillatory magnetic field solicitation. Finally, we will describe major advances in materials-oriented magnetic induction, with a particular focus on stimulus healing and situate our work in this growing literature.

1 Thermoplastic elastomers

1.1 Definition

In the mid-1960s, multiblock copolymers (MBC) based thermoplastic elastomers (TPE) were introduced as a new class of polymers relying on microphase separation, including benefits from both thermoplastic and elastomer materials. [1, 2] They have been widely studied, developed and improved over the years for their relative ease of processing and their specific mechanical properties, making them valuable for fundamental science and direct application in several industrial sectors. In the early 1980s, possible ordered microstructures, such as spherical, cylindrical and lamellar phases, were proposed for diblock copolymers, helping to rationalize the physics of phase separation in more complex MBCs. [3] The understanding of the phase separation process has then been enriched through a variety of experimental and theoretical works performed on amorphous diblock and triblock copolymers in the late 1980s and 1990s, [4-8] further helping the contemporaneous development of MBCs. In this work, TPE are taken as a reliable alternative for rubber-based mass goods, because they can undergo many cycles of processing and can easily be repaired/reshaped. [9, 10]

MBC are often made of crystallizable segmented block copolymers, combining rubber-like properties of elastomers (flexibility) and ease of processing from thermoplastic polymers. They are composed of an alternating arrangement of “soft” amorphous and “hard” crystallizable segments (denoted SS and HS respectively), resulting in hard domains encompassed into a soft flexible matrix. By connecting SS, HS crystallites bestows to the material its elasticity. As long as the HS melting point is not reached, HSs act as permanent nodes in a similar manner as sulfur bridges ensures the elasticity in vulcanized elastomers. Their mechanical performances are, indeed, predominantly driven by the hard phase volume fraction and morphology. [11] On the

other hand, the soft phase provides the material with its flexibility, allowing properties recovery after high deformation. [12] More anecdotally, SS may crystallize slightly at low temperature according to their chemical structure (*e.g.*, around 0°C for PTHF [13]).

The thermoreversible character of TPEs relies on the phase-separation and homogenization respectively upon decreasing or increasing the temperature. According to the molecular topology, the phase separation can either drive or be driven by the crystallization [14] leading to the growth of hard domains ensuring the solid-like behavior. The homogenization temperature of crystallizable TPEs correspond to the melting point of the hard-domains, triggering molecular diffusion and the material's flow at the macroscopic lengthscale (Figure 1.1). The thermoreversible nature of TPEs makes them able to be reused, reshaped, repaired and recycled. [9, 10] Therefore, TPEs can be manufactured through extrusion, injection molding, hot-pressing and even 3D printing. This behavior needs to be considered in contrast with chemically crosslinked elastomers, which have excellent mechanical properties but cannot flow making them (currently) almost impossible to be efficiently recycled. [15]

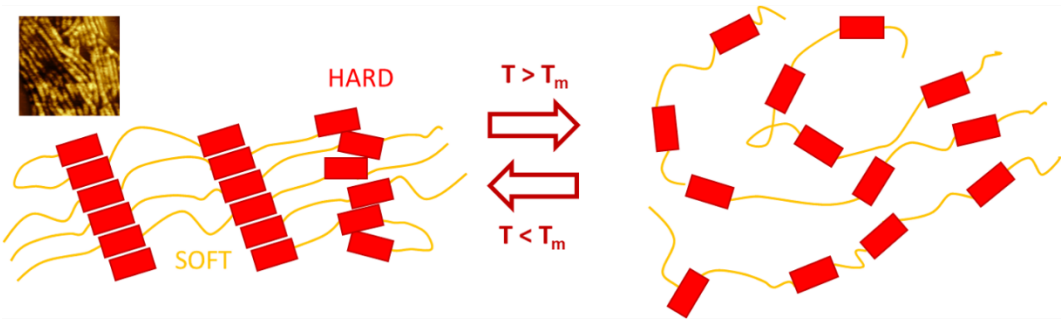

Figure 1.1: Schematic representation of the TPE thermoreversibility. At low temperatures, hard segments (red) gather forming ribbon-like structures while at higher ones homogenization occurs

On one hand, SSs are commonly made of low-T_g polymers such as polybutadiene (PB), [16-18] polyisoprene (PI), [18-20] polyethylene oxide (PEO), [21, 22] polyethylene (PE), [23, 24] polypropylene (PP), [25] polydimethylsiloxane (PDMS), [26] poly-1-octene, [27] polytetramethylene oxide (PTMO), [28-30] or polytetrahydrofuran (PTHF). [31-33]

On the other hand, HSs are made of crystallizable segments such as polystyrene (PS), [16-18] polyethylene terephthalate (PET), [22] polycyclohexylethylene (PCHE), [23, 24] polymethyl methacrylate (PMMA), [26] an orthorhombic form of PE, [27] polybutylene terephthalate (PBT), [28, 29, 34, 35] T4T, [32, 36] T6T, [30] T6A6T, [30, 37] T6T6T, [30, 38] TΦT, [39, 40] polyamide 12 (PA12), [31] polyamide 1012 (PA1012) [41] or oxalamide groups. [33]

While any combination of HS and SS could have possibly led to an interesting material for this study, we decide to focus our attention on a commercial thermoplastic polyurethane (TPU), being a sub-class of TPEs based on diisocyanates and diols. The existing chemical linkage denoted as urethane is: $(-NHCOO-)$ The reasons for having chosen a commercial TPU rely on their low cost and their proven capacity to be scaled up to the industrial scale. Moreover, TPUs are characterized by a good resistance to humidity and suitable mechanical properties for the intended applications. This TPU (*i.e.*, Desmopan 85085A) is made of an association of hexamethylene diisocyanate (HDI) and 1,6-hexanediol (HDO) as HS and of butanediol polyadipate and polypropylene oxide as SS_1 and SS_2 respectively, as shown in Figure 1.2. The weight fractions of HS, SS_1 and SS_2 are 28.0, 49.5 and 22.5 wt.% respectively. We remind the reader that the TPU and the corresponding composites prepared in this work will be submitted to many temperature cycles, and their resistance to oxygen will prevent any undesired reaction with the environment.

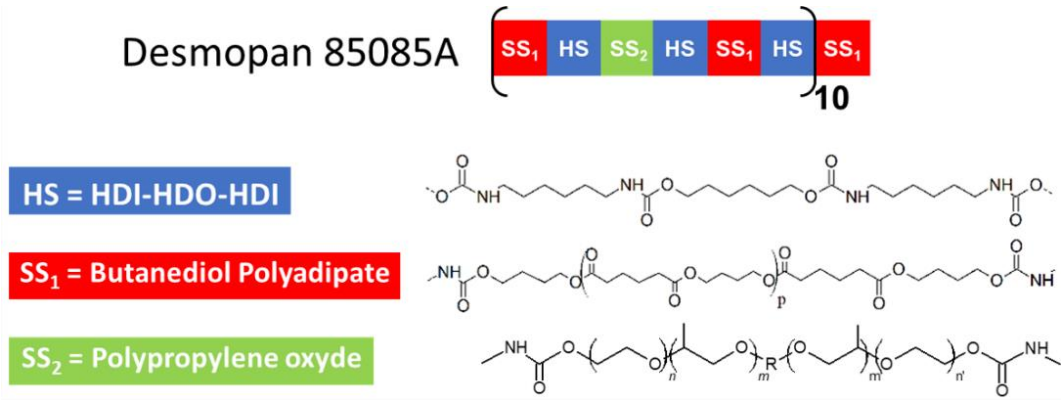

Figure 1.2: Schematic representation of the arrangement between HS/SS_1/SS_2 in the TPU (Desmopan 85085A) architecture and the topological formulae of each if its segments.

1.2 Relation between TPE structure and properties

As presented above, TPEs combine interesting properties of thermoplastic polymers and elastomers through the arrangement and separation of soft and hard phases. Interestingly, the structure of HS aggregates can be modified to tune the mechanical properties of the TPEs. [12] The process used (*e.g.*, drop casting, solvent casting or hot-pressing) influences the structure [42] (see Figure 1.3) impacting *de facto* the mechanical properties. [13] Moreover, different morphologies and physical properties can be obtained by varying the type, the length and the fraction of segments used. [3, 43, 44] Phase separation depends on the interactions between the

respective chemical species and on the mobility of the chains through their capacity to arrange themselves in specific conformations reducing their entropy during the processing. Polymer-oriented self-consistent field theory and numerical resolution methods are reliable procedures able to predict the structure of multiphasic polymers, [45, 46] through the simplification of the problem into the analysis of a single polymer chain.

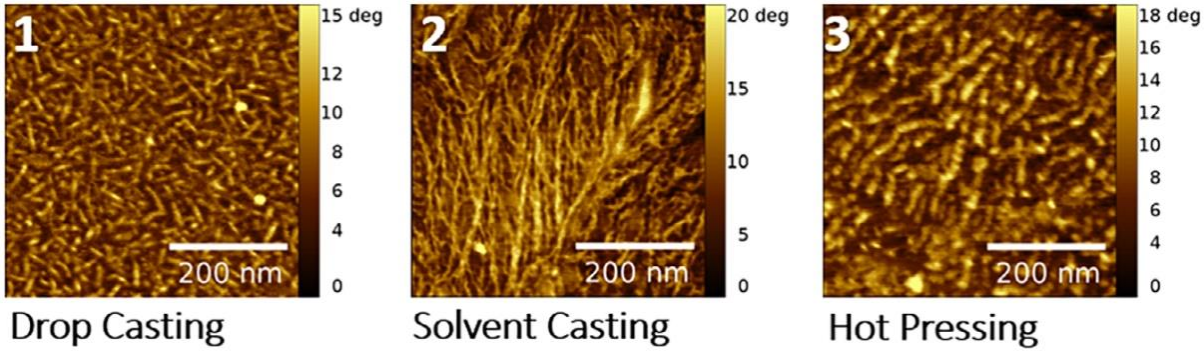

Figure 1.3: AFM micrographs of a PBT-PTHF based TPE containing ca. 30 wt.% in HS (PBT). This TPE was prepared through (1) drop casting, (2) solvent casting and (3) hot-pressing adapted from [42]. The high rigidity phase consisting of HS crystallites appears in "light gold".

A relevant aspect to consider to understand the TPE's structure is its thermal behavior. The relevant characteristic temperatures of a TPE are the glass transition of the SS (and possibly the HSs) (T_g) as well as the melting and crystallization points (T_m and T_c respectively) of both SS and HS (see Figure 1.4). The glass transition T_g designates the transition between the glassy state and the rubbery state in an amorphous polymer. It is related with the motion of chain-segments made of a few repetition units – often called principal or α-relaxation. [47] Importantly, crystallizable MBC can play the role of a TPE on the condition that SS and HS are respectively rubbery and crystalline at service temperature. Differential scanning calorimetry (DSC) thermograms in Figure 1.4 clearly show the effect of different HS content on these transitions. This also prevents the formation of stable SS crystallites, as suggested by the lack of transition peaks in HS65 caused by the impossibility for the short SS (*ca.* 1 kg/mol) to bend. DSC further revealed the effect of **polydispersity** [30] of crystallizable segments on the thermal transitions of the TPE. Indeed, polydisperse segments tend to hinder the formation of crystallites. In contrast, perfectly monodisperse and short segments can lead to high crystallinity. It has been proven that monodisperse T4T HS with well-calibrated sizes can crystallize up to ~70%. [32]

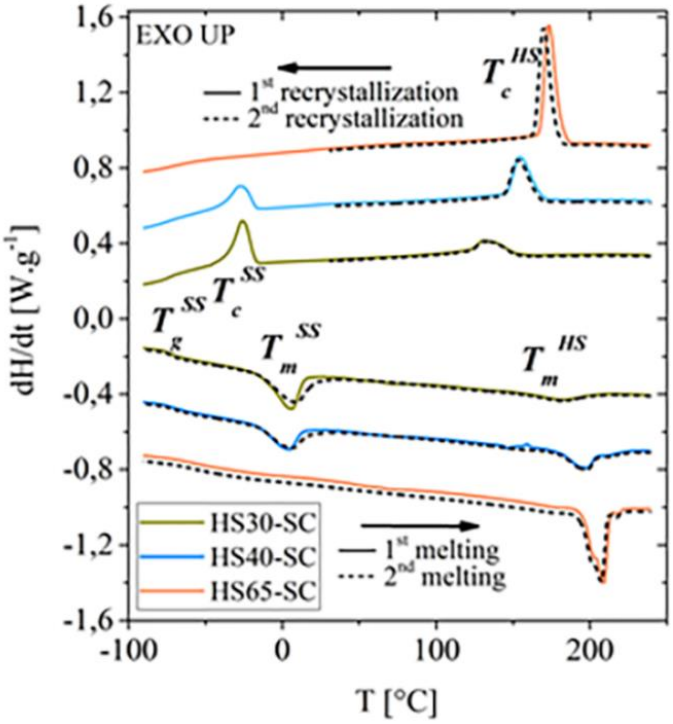

Figure 1.4: DSC thermograms of solvent cast TPEs with different hard segment content, adapted from [42]. HSx-SC designates the HS content in the TPE. T_g^{SS}, T_m^{SS}, T_m^{HS}, T_c^{SS} and T_c^{HS} designate the SS glass transition, melting and crystallization points of SS and HS respectively.

Besides, high mechanical properties are required to compete with strong chemically cross-linked rubbers. The mechanical behavior of TPEs can be adapted and modified by changing the SS length, the chain's molar mass, the ratio between HS and SS and the process used to prepare the material. The uniaxial tensile tests are often used to analyze the material's behavior up to the breaking point. At low deformation, TPEs show a quasi-elastic behavior from which we can access the elastic modulus (initial slope of the $\sigma = f(\varepsilon)$ curves).

Polyurethane-urea (PU) copolymers with **low SS and HS molar mass** (2.0 and 0.9 kg mol^{-1}) and annealed at 60 and at 100°C are shown in Figure 1.5A. They have a well-defined elastomeric behavior, because in both cases SS are completely amorphous with their respective characteristic temperatures being T_g^{SS} = -57.3 and 61.9 °C and T_m^{SS} = 19.9 and 17.6 °C. In these cases, phase separation is relatively weak, therefore chains are expected to diffuse with low mechanical solicitations. This type of response is characterized by low Young's modulus and no yield point present in their tensile curves. The materials dried at 100°C (*i.e.*, PU-X-100 displayed in red) present an enhancement in mechanical properties when compared to those dried at a lower temperature of 60°C (*i.e.*, PU-X-60 displayed in black). This behavior is

explained by the structural and morphological changes, such as the formation of α-complex crystalline structures confining hydrogen bonds within a small region, occurring at higher temperatures of annealing. The densely packed hydrogen bonds allow for an effective load transfer under mechanical solicitation, indicating a more robust elastomeric network.

Two other PU copolymers with the same HS/SS chemistries and ratio of HS content (*i.e.*, 30 wt.%) are presented in Figure 1.5B, however they differ by a **higher molar mass** (*i.e.*, 8.0 and 3.4 kg mol^{-1} for SS and HS respectively) for two different temperatures of annealing. These materials present clear elastoplastic behavior, with an initial elastic response up to a yield point, followed by softening due to the first chain pull-out events and a subsequent hardening due chain alignment. [48] In these cases, phase separation is more relevant, [12, 49] blocking chain diffusion. Mechanical solicitations initially stretch SS up to the pull-out of HS (appearance of a yield point). This process may further result in strain-induced crystallization [21, 28, 50] (see Figure 1.6). The progressive fragmentation of the HS, *i.e.*, the loss of connection of the network ultimately leads to plasticity and ultimately to the macroscopic failure of the material. This is possible because SS are semicrystalline in these materials. Note the values of T_g^{SS} are -49.3 and 68.7°C and those of T_m^{SS} are 51.2 and 45.1°C for PU-8-60 and PU-8-100 respectively.

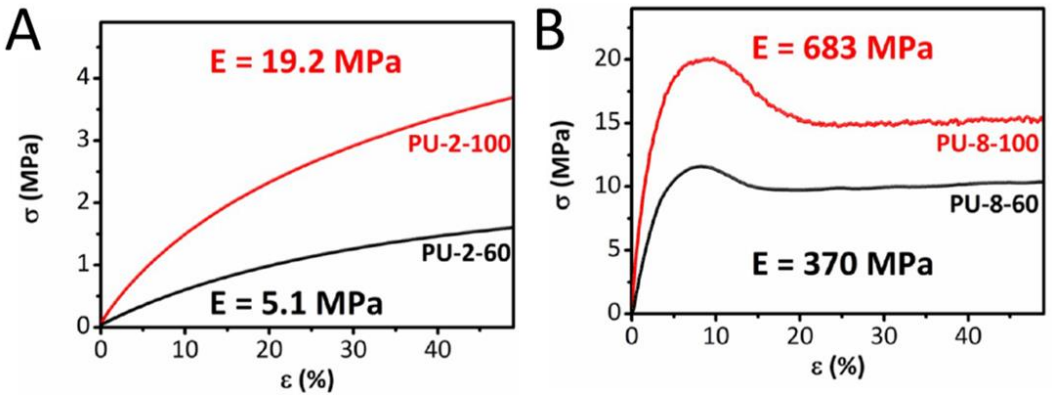

Figure 1.5: Influence of the temperature of annealing on stress-strain curves of polyurethane-urea (PU) copolymers with SS molar mass of (A) 2 kg mol^{-1} and (B) 8 kg mol^{-1}, adapted from [48]. PU-X-60 and PU-X-100 refers to copolymers annealed under vacuum at 60°C and 100°C respectively.

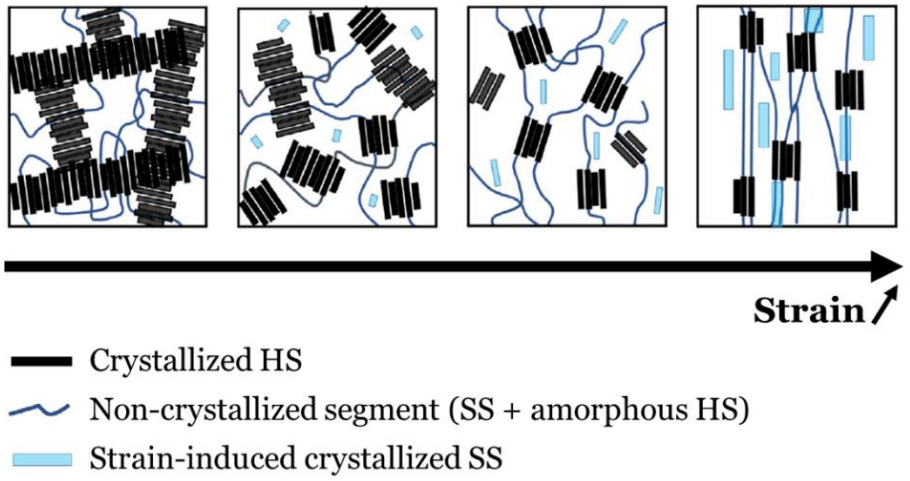

Figure 1.6: Schematic representation of a crystallizable TPE morphology evolving with increasing strain amplitude, showing successively chain pull-out events, chain alignment and strain induced crystallization of SS, adapted from [50].

A set of uniaxial tensile tests performed on copolymers with varying structural parameters is compiled in Figure 1.7. For example, increasing the **HS content** in copolymers leads to a systematic stiffening, caused by a higher crystalline content accompanied with larger crystallites, both effects enhancing the degree of connectivity of the network. However, in the case of short copolymers (*i.e.*, under 15 kg mol^{-1}), each molecule can only form a limited number of topological links through entangling or crystallization, which explains the failure at low strain (see Figure 1.7A). Conversely, increasing the **chain length** leads to the emergent role of bridging segments, with failure at higher strain, indicating a higher connectivity between the chains. For long chains, increasing the HS content leads to larger strain hardening but lowers the strain at failure of the material. Figure 1.7B shows the effect of **temperature** on the mechanical behavior. The reduction in strain at failure of these materials can be predicted depending on the temperature, the chain length and the interactions between HSs by modeling the kinetics of the formation and the breakage of physical bonds between HSs. [51] Finally, Figure 1.7C shows how the strain rate affects mostly the non-linear regime of the mechanical behavior. With higher strain rates (solid lines), chains do not have enough time to relax, thus alignment and stretching of SSs is favored as illustrated by a stiffening at large strain.

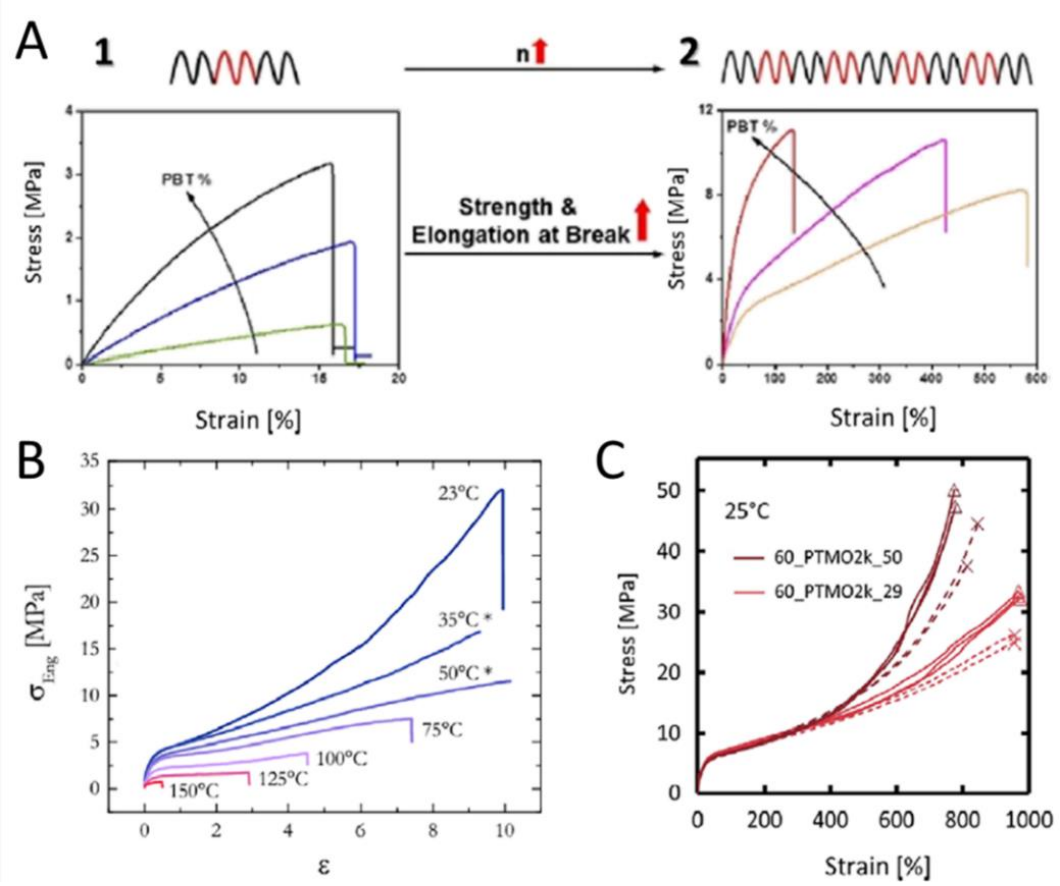

Figure 1.7: Uniaxial tensile tests performed on PBT-PTHF copolymers. (A) The effect of increasing (1) the HS (PBT) content and (2) the number of segments, adapted from [52]. (B) The effect of the temperature, adapted from [51]. (C) The effect of the chain length (50 and 29 kg mol^{-1} represented in red and brown respectively) and the strain rate (0.17 and 0.0017 s^{-1} represented in solid and dashed lines respectively), adapted from [50].

The thermoreversible nature of TPEs makes them easy to handle and to study in the molten state or around the melting temperature. Rheology is the most reliable technique for this type of characterization. The flow regime is related to chain diffusion and is strongly impacted by the phase morphologies. Figure 1.8A shows the storage G' and the loss G'' moduli in the flow regime of a molten TPE, measured through dynamic frequency sweeps and completed with inverted creep measurements at the same temperature. This example does not correspond to a homogenous polymer melt, in which $G' \sim \omega^2$ and $G'' \sim \omega$ are expected (Maxwell fluid). In fact, at low frequencies, MBC also display sources of elasticity, which come from the phase separation persisting in the molten state (see Figure 1.8A). This indicates the possibility of manipulating the polymer in the molten state to engineer useful morphology once solidified. [53] This is notably the case when dealing with **shear-induced crystallization** [53, 54] which provides the possibility to stretch and therefore, the opportunity to tailor the hard domains

structure beyond the use of solvents (see Figure 1.3). The phase transition can be detected through frequency sweeps, temperature sweeps or small amplitude oscillation shear (SAOS) for shear induced crystallization (see Figure 1.8B).

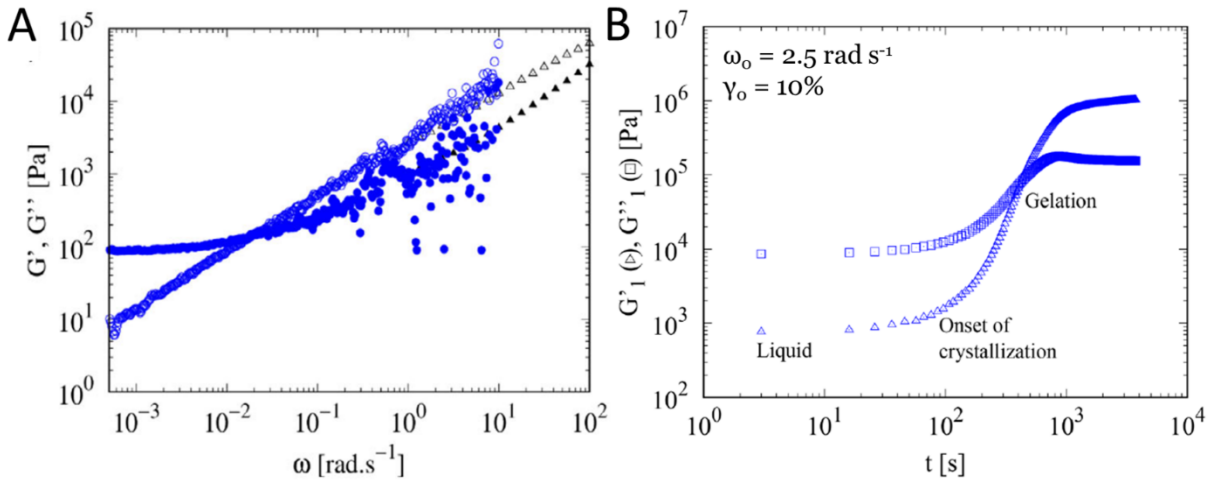

Figure 1.8: (A) Dynamic frequency sweep (black) and creep (blue) measurements performed on a PBT-PTHF segmented block copolymer at 185°C after melting it at 210°C. Open and filled symbols correspond to storage G' and loss G" moduli respectively. (B) SAOS measurement performed on the same PBT/PTHF copolymer at 140°C showing its phase transition through time. Figures are adapted from [54].

A complete characterization of the polymer is therefore necessary to fully comprehend its behavior. The different aspects related to the TPE structure (*i.e.*, type of HS and SS, chain length, ratio between HS and SS and process) will result in specific thermal and mechanical properties. Although in this thesis, we decided to focus mainly on one TPE matrix, it should be reminded that by changing the chemistry and the chain structure, we can tune the properties of the responsive material to match particular specifications.

1.3 Applications of TPE

In 2021, the TPE market represents 3.84 million tons market and is expected to grow to 5.55 million tons by 2026. [55] The processing advantages and the mechanical behavior of TPEs make them particularly interesting in a wide range of applications (see Table 1.1). The manufacturing of vehicles components is the primary sector for all TPE products. They are also highly relevant for sports goods, medical devices, household items, bitumen modifiers, [56, 57] adhesives, [58, 59] energy dissipators, [60] reinforcing fibers, [61] polyelectrolytes, [62, 63]

compatibilizers [64] and strain sensors. [65, 66] Figure 1.9 shows some examples of TPEs in common goods. From an industrial point of view, the two main characteristics of a TPE that are 1) good mechanical properties and 2) ease of processing make them a good choice for cost effective production and design flexibility.

Each type of TPE offers a distinctive set of properties (see Table 1.2). TPEs are generally good electrical insulators but fairly susceptible to high-energy UV radiation. The chemical performance of the TPE will depend greatly on their chemical structure. The main advantages for each type of TPE are summarized in the following table:

Markets	Applications
Automotive	Weather seals, shock dust boots, exterior and interior trims, instrument panels, air ducts, pipe grommets, glass encapsulation, drive belts, high/low pressure pipes, mats for motor scooters, O-rings
Construction	Extruded seals for doors and windows, simple or co-molded hydraulic seals, glazing seals, pipe seals
Industrial	Anti-vibration mounts, inlet pipes and exhaust manifolds, seals, drum suspension bushes, shock absorbers, roof membranes
Consumer goods	Magnetic seals for refrigerators, power tools handles, remote control covers, mobile phone covers, push-button panels, shock absorbing protections for vacuum cleaners
Medical	Breathing tubes, syringe seals 7 tips, ventilation masks and bags, seals, valves, catheters
Electronics	Sheaths for condensers, plugs and loose sockets, cables, mobile phone components
Footwear and sporting goods	Items for diving (flippers, snorkels, masks) and skiing (ski pole handles, ski boots), sports goods, shoe soles

Table 1.1: Most common TPE uses for different sectors. [67]

Figure 1.9: TPE products. PolyOne GLS supplies, adapted from [68]. TPEs in electronic components, adapted from [67]. Medical KRAIBURG TPE compounds, adapted from [69]. TPEs used for the soles of sport shoes, adapted from [67].

Material	Advantages
Thermoplastic polyurethanes (TPU)	Chemical tunability, abrasion resistance, tear strength, stiffness properties, and oxygen, ozone and weather resistance
Thermoplastic styrenic block copolymers (SBC)	High tensile strength and modulus, miscibility, good abrasion resistance, electrical properties
Thermoplastic elastomer polyolefins (TPO)	Flexible, inert, nontoxic
Thermoplastic vulcanizates (TPV)	Mechanical properties, fatigue durability, liquid and oil resistance
Thermoplastic copolyester elastomer (COPE)	Dynamic properties, good resistance to chemicals and oil, excellent strength, heat resistance, electrical insulator
Thermoplastic polyether block amides (COPA)	Processability, heat resistance, wear resistance

Table 1.2: TPE advantages in accordance with the different natures. [67]

Importantly, the thermoreversible nature of TPEs make them good candidates to be incorporated in reusable products in the aforementioned markets (see Table 1.1). The process of melting and reshaping the material into its original structure leads, in theory, to an almost complete recovery of the original shape of the material and its properties. Although it should be noted that the recovery capacity of a material is not only defined by the recovery of its properties (*i.e.*, mechanical, rheological, electrical properties) after one cycle, but also by the number of reuse cycles to which it can be submitted, which directly depends on its chemical stability.

The main condition for allowing the reshaping of a TPE is to reach its liquid state (*i.e.*, the melting point of HS), which can be done through different heating methods. In this thesis, we chose magnetic induction as the reliable and efficient method of reaching the TPU melting point. This method relies on loading the matrix with magnetic fillers. It presents clear advantages when compared to usual convective heating:

- Remote control heating mechanisms enabling an increase in temperature without direct contact between the composite material and the magnetic inductor generating the alternating magnetic field.
- Spatio-selective heating is possible through controlled localization / diffusion of magnetic fillers in an architectured material.
- High tunability for the targeted temperature, as the heat generation depends simultaneously on the external stimulus (*e.g.*, magnetic field amplitude, frequency, irradiation time) and on the material's properties (*e.g.*, filler fraction, particle nature and size, and viscosity of the matrix).
- Reduced thermal inertia, due to the absence of susceptors, enabling quick phase transitions and limits the thermal gradient across the sample thickness.

To fully understand how magnetic induction works, we will describe all the basic concepts in the following section, and then be able to describe the research performed on magnetic composites.

2 Magnetism and associated heating mechanisms

In this section, we will describe the fundamentals of magnetism and different magnetic behaviors, with a special focus on superparamagnetism. Then, we will detail the possible heating mechanisms using a magnetic stimulus.

2.1 Fundamentals

2.1.1 Atomic spin

A spin magnetic moment is associated to every elementary particle, such as protons, neutrons and electrons. Magnetic moments, at the atomic scale, are caused by the spin contribution of its corresponding elementary particles. In SI units, magnetic moments m is expressed in A.m^2. A group of spins aligned in the same direction can be considered as a macrospin (Figure 1.10A). A magnetic domain (Weiss domain) in a material is usually characterized by a single macrospin and is limited by domain walls (Bloch walls).

In multi-domain ferro/ferrimagnetic structures, regions with uniform magnetization are limited by these domain walls (Figure 1.10B). [56] These structures will react to an increase of an exterior magnetic field $\vec{H}$ by reorienting its magnetic domains progressively and through the movement of the domain walls, until every magnetic moment is aligned in the direction of the magnetic field $\vec{H}$ whose amplitude is measured in A.m^{-1} (or Oe in cgs units).

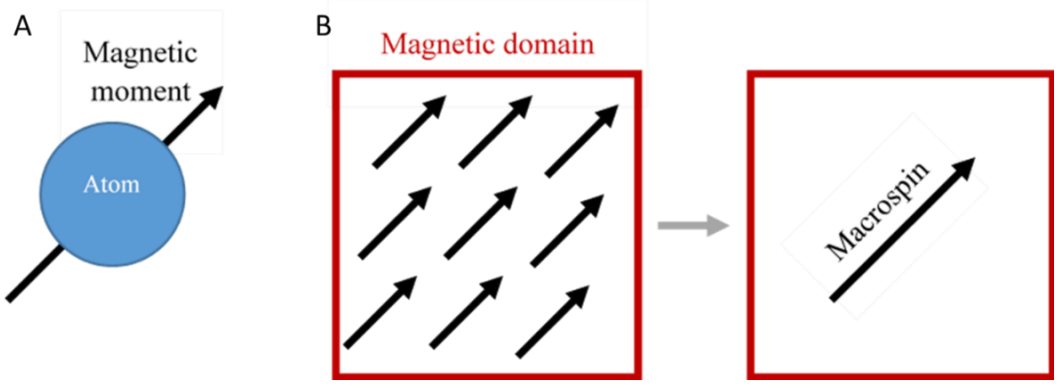

Figure 1.10: Illustration of magnetic moments. (A) Atomic magnetic moment. (B) Macrospin representation within a Weiss domain.

2.1.2 Magnetic susceptibility and relative permeability

Materials behave differently when subjected to a magnetic field $\vec{H}$, depending on their nature. This behavior is characterized by the magnetization $\vec{M}$, whose amplitude corresponds to the density of magnetic moments in a magnetic material, measured in $A.m^{-1}$ (or Oe in cgs units). [70]

In addition, parameters such as temperature, pressure, and frequency or amplitude of the applied magnetic field can induce a change on the material reaction with respect to the magnetic field $\vec{H}$. [70] In the linear regime, the amplitude of the magnetization $\vec{M}$ and the applied magnetic field $\vec{H}$ are associated through the magnetic susceptibility χ, with no unit.

$$\vec{M} = \chi\vec{H} \tag{I-1}$$

Another equation is also often used to characterize the induced magnetic field $\vec{B}$, measured in T, reacting to an applied magnetic field $\vec{H}$ through the permeability μ, measured in $H.m^{-1}$.

$$\vec{B} = \mu\vec{H} = \mu_0(\vec{H} + \vec{M}) \tag{I-2}$$

The induced magnetic field $\vec{B}$ gathers the magnetic field in vacuum $\mu_0\vec{H}$ and the magnetic response of the material $\mu_0\vec{M}$. [70] The response of a material subjected to a magnetic field $\vec{H}$ can be evaluated by either the magnetic susceptibility χ or the relative permeability μ_r, both of which are linearly linked and have no unit.

$$\mu_r = 1 + \chi \tag{I-3}$$

with the relative permeability μ_r being the ratio between the permeability μ and the vacuum permeability μ_0.

$$\mu_r = \frac{\mu}{\mu_0} \tag{I-4}$$

The main types of magnetism will be described in the following sections: diamagnetism, paramagnetism, ferromagnetism, ferrimagnetism and superparamagnetism.

2.2 Types of magnetism

2.2.1 Diamagnetism

The magnetic moment on a diamagnetic material is null. When a magnetic field $\vec{H}$ is applied on a material, an electric current is induced as a loop opposing the change in magnetic flux. [71] This interaction, weakly repulsive to the magnetic field $\vec{H}$, is due to a slight modification to electron rotation under a magnetic field. This means that there could be a slight tendency to align the dipoles opposite to the applied magnetic field $\vec{H}$ (Figure 1.11). All materials present a small diamagnetic behavior, that may or may not contribute to the whole material's magnetic behavior.

A diamagnetic material presents no magnetic moment, therefore there is nothing to compensate the intrinsically repulsive reaction to the magnetic field. Materials such as polymers are diamagnetic. Diamagnetic materials, such as copper, lead and silver, have a magnetic susceptibility χ slightly inferior to zero (χ ~ -10^{-5}).

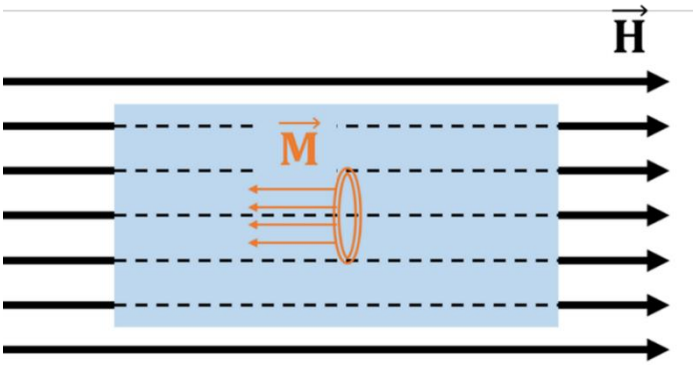

Figure 1.11: Diamagnetic material (blue) interacting with an external magnetic field $\vec{H}$. Slightly repulsive interaction $\vec{M}$ (orange).

2.2.2 Paramagnetism

Materials with a small magnetic moment due to the presence of unpaired electrons in their atomic orbitals, exhibit a paramagnetic behavior. In this case, the applied field $\vec{H}$ can slightly align the individual magnetic moments in the material. The repulsive diamagnetic response is still present in the material but it is overcome by the attractive influence of the magnetic moments. [71] The overall interaction is weakly attractive toward a magnetic pole.

When no magnetic field $\vec{H}$ is applied to the paramagnetic material, all moments are randomly oriented in every possible direction as represented in Figure 1.12. Paramagnetic materials retain no magnetization in the absence of the magnetic field. They have a magnetic susceptibility χ slightly superior to zero ($\chi \sim 10^{-5}$).

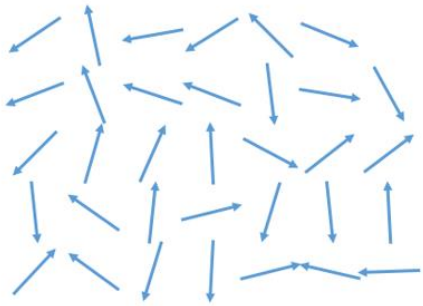

Figure 1.12: Randomly oriented magnetic moments within paramagnetic material. At the macroscopic scale, the sum of all moments is null.

2.2.3 Ferromagnetism

As explained in Chapter I section 2.1.1, a magnetic domain is a domain in which the spins are aligned in a given direction, limited by domain walls, both of which are pictured in Figure 1.13. [72] A magnetic domain is, thus, characterized by a single macrospin oriented in one direction. The size of these domains is usually in the order of the tens of nanometers.

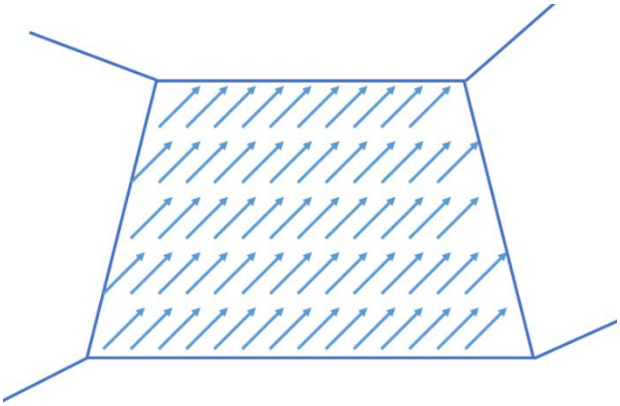

Figure 1.13: Magnetic moments in a ferromagnetic material. Block walls separating magnetic domains (Weiss domains) characterized by an internal alignment of the magnetic moments.

Ferromagnetism is limited by a temperature beyond which the magnetization is suppressed by the thermal motion. This temperature is called Curie temperature T_{Cu} measured in K, and represents the transition between ferromagnetism and paramagnetism. This means that above this value, the thermal agitation induces a disorder in the material, the magnetic domains cannot be maintained and the material becomes paramagnetic, losing its ferromagnetic properties. In the case of iron and magnetite, Curie temperature is 1044 K and 858 K respectively. [71, 73-75]

Ferromagnetic materials have a strongly attractive interaction toward a magnetic solicitation. Their magnetic susceptibility χ is higher than 10^{-2}, and therefore they are more sensitive to an external field through the alignment of their magnetic spins. An example of a ferromagnetic material is iron Fe (χ ~ 200 000). Once the magnetic field $\vec{H}$ is applied to a ferromagnetic material, its macrospins start to align in the direction of the applied field, causing a motion of their domain walls. Magnetic domains, which were already oriented in the direction of the applied field, will grow by realigning the spins at the border of the domain wall.

Initially, the magnetization M increases linearly with the magnetic field amplitude H with χ as the slope. At higher amplitudes of H, there is a non-linear increase of the magnetization M until the magnetic saturation M_s, corresponding to the point at which all the magnetic domains are aligned in the direction of $\vec{H}$ (see Figure 1.14). After reaching M_s, if the applied magnetic field H is stopped, the magnetic domain spins will not return to the original stable configuration. The material will present a magnetic remanence M_r. The magnetization M of a ferromagnetic material can return to zero by applying a magnetic solicitation in the opposite direction. This solicitation is called coercivity H_c, measured in A.m^{-1}, [71, 76] which decreases with the particle size d [77]:

$$H_c = H_{c,0} + \frac{cnst}{d} \qquad \text{(I-5)}$$

This is applicable for all multi-domain particles; nevertheless, it cannot be applied to single-domain particles. The coercivity H_c attains a maximum in the limit between the single-domain and the multi-domain.

Both M_r and H_c are measured in A.m^{-1}. Figure 1.14 shows the different magnetic responses to an applied magnetic field $\vec{H}$. The case of superparamagnetic behavior will be introduced in Chapter I section 2.3.

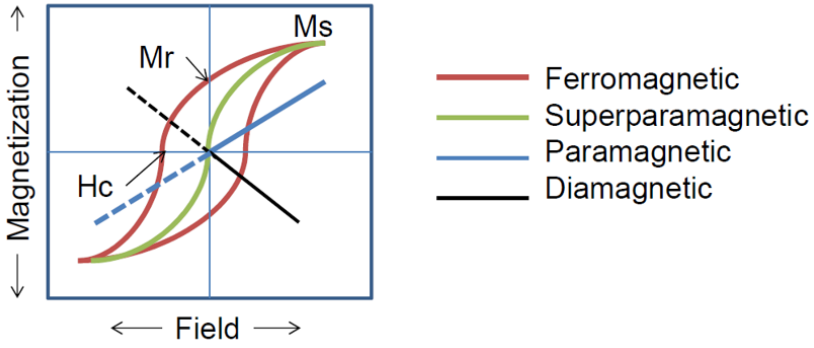

Figure 1.14: Magnetic behavior of different materials submitted to an applied magnetic field. [78]

2.2.4 Ferrimagnetism

Ferrimagnetic materials have two sublattices creating an antiparallel alignment. [71] Their moments are parallel to each other but in opposite directions, as shown in Figure 1.15. These moments do not cancel each other, meaning that they leave a permanent magnetization in the material. Thus, the sum of the moments is also susceptible in regards to the magnetic field. Similarly, to ferromagnetic materials, ferrimagnetic materials exhibit magnetic domains of size in the tens of nanometers.

Ferrimagnetic materials also have a magnetic susceptibility χ higher than 10^{-2}. An example of a ferrimagnetic material would be magnetite Fe_3O_4 (T_{Cu} = 860 K and χ = 2,59). [71, 73, 79]

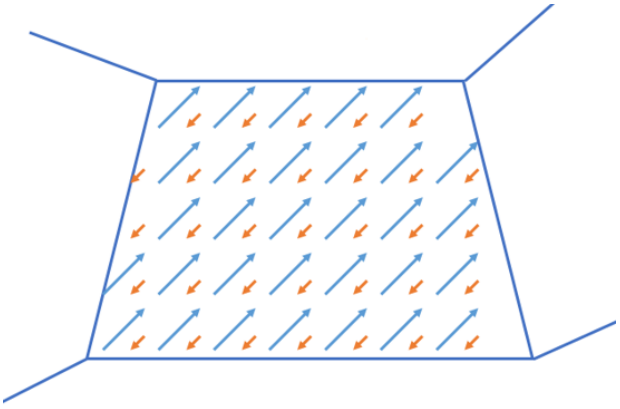

Figure 1.15: Magnetic moments in a ferrimagnetic material. Opposite moments (blue, orange) do not balance each other.

2.3 Superparamagnetism

2.3.1 Superparamagnetic domain

The behavior of a ferro/ferrimagnetic material changes once its size reaches the dimensions of a single magnetic domain. Identifying the different magnetic behaviors is of utmost importance when dealing with small particles of a magnetic material. Near this size, there is a critical value below which it costs more energy to create a domain wall than to support the magnetostatic energy. [56] This single-domain particle is uniformly magnetized with all of its spins aligning in the same direction. [56] The maximum single-domain size D_s represents the limit between single-domain and multi-domain and is defined by equation (I-6).

$$D_s = 72\sqrt{A_p|K_1|}/\mu_0 {M_s}^2 \quad \text{(I-6)}$$

where K_1 is the magnetocrystalline anisotropy in J.m^{-3} and A_p is the exchange stiffness constant which serves to characterize the electron exchange in a ferromagnetic material in J.m^{-3}. [80] The different types of magnetic anisotropies will be explained in Chapter I section 2.3.4.

An individual particle, smaller than the single-domain size, having one large magnetic moment (or macrospin), can behave like a giant paramagnetic atom with fast response to an applied magnetic field $\vec{H}$. Superparamagnetic particles are a variant of a ferro/ferrimagnetic material. Once the size of a ferro/ferrimagnetic material is sufficiently small, the size of the particle is similar to that of a magnetic domain (tens of nanometers). This limit particle size is referred as the superparamagnetic blocking diameter D_{sp}, and its value can be determined by equation (I-7). [80]

$$D_{sp} = (48k_B T/|K_1|)^{1/3} \quad \text{(I-7)}$$

where T is the temperature in K and k_B is the Boltzmann constant k_B = 1.38 x 10^{-23} J.K^{-1}.

Under the superparamagnetic limit, the particle will then be characterized by one macrospin with all of its local moments aligned in one single stable direction, determined by its magnetocrystalline anisotropy. Meaning that at small particle sizes, there can be frequent spontaneous magnetization reversal, from one stable orientation to the opposite one. After a

certain amount of time, the orientation of the macrospin can be spontaneously reversed (without the use of a magnetic solicitation).

Superparamagnetic nanoparticles keep a high value of magnetic susceptibility χ. In contrast to the two previous types of magnetism (ferro/ferrimagnetism), superparamagnetic particles do not display a hysteresis through a magnetization test at low frequency and therefore the coercivity H_c is null (see Figure 1.14).

The values of D_{sp} and D_s for iron Fe and magnetite Fe_3O_4 particles are referenced in Table 1.3, calculated for spherical particles. These values are susceptible to the particles' shape factor. Figure 1.16 shows the coercivity H_c as a function of the particle size. It also displays the multi-domain and single-domain particles separated D_s, as well as the ferro/ferrimagnetic FM and the superparamagnetic SPM domains separated by D_{sp}.

	Fe	Fe_3O_4
Superparamagnetic blocking diameter D_{sp}	16 nm	26 nm
Maximum single-domain size D_s	20 nm	76 nm

Table 1.3: Characteristic particle size, for spherical particles, limiting different behavioral magnetic ranges.

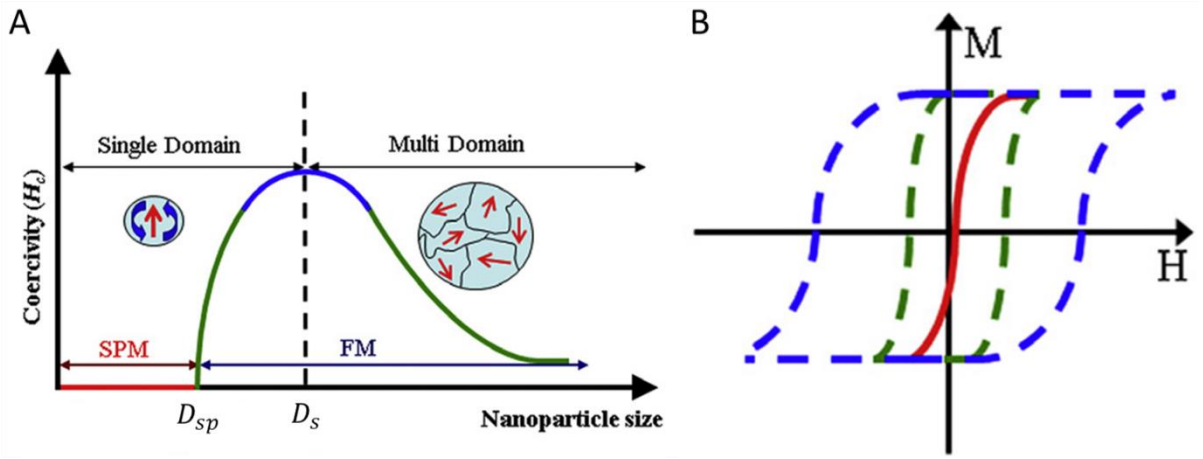

Figure 1.16: (A) Particle coercivity H_c versus particle size, with D_{sp} being the superparamagnetic blocking diameter and D_s being the maximum single-domain size. [81] (B) Magnetization curves displaying the presence or lack of hysteresis for different particle sizes, with colors matching the coercivity figure.

2.3.2 Blocking temperature

The superparamagnetic behavior is also characterized by the blocking temperature T_B. Thermal fluctuations need to be sufficient to enable the rotation of the magnetic moment of the particle. Above the blocking temperature T_B, ferro/ferrimagnetic nanoparticles exhibit superparamagnetic behavior, the rapid nanoparticle magnetization reversals can take place while it is not possible below (spins are considered as blocked and do not react to an exterior solicitation). [78, 82] This characteristic temperature depends on the size and the magnetic properties of the particle, according to the following equation [82]:

$$T_B = \frac{|K|V}{k_B \ln(\tau_m/\tau_0)} \quad \text{(I-8)}$$

Where K is the magnetic anisotropy constant in J.m^{-3}, V is the particle volume in m^3, τ_m is the measurement time (the inverse of the frequency f_m of the magnetic field used for the measurement) and τ_0 is the attempt time, both in s. The attempt time τ_0 is an average timescale between two successive random thermal excitations, usually between 10^{-9} and 10^{-12} s. [56, 76, 78, 83-89]

An increase in particle size will directly lead to an increase in the value of the blocking temperature T_B. [85] With the blocking temperature T_B being highly sensible to the particle volume, a wide distribution of the particle sizes results in a wide distribution of the blocking temperatures T_B. [56]

A dependence of T_B with the value of the applied magnetic field $\vec{H}$ has also been reported, showing that the increase of the amplitude H shifts the blocking temperature T_B towards lower temperatures. [90] For example, Tanwar *et al.* [91] performed Zero Field Cooling – Field Cooling (ZFC-FC) on 10 nm monodisperse magnetite Fe_3O_4 particles showed the dependency of T_B as a function of the applied field H. These measurements, performed at 50, 200, 500, 1000, 2000, 3000, 4000 and 5000 Oe, result in 96, 80, 60, 44, 30, 22, 19 and 15 K as blocking temperatures. T_B should not be considered as the limit of a phase transition but as a temperature for which a sudden change in relaxation time τ occurs. [83]

2.3.3 ZFC-FC curves

It is possible to differentiate a ferromagnetic material from a superparamagnetic material by characterizing its response to a magnetic field through a wide temperature range. A Superconducting Quantum Interference Device (SQUID) or a Vibrating-Sample Magnetometer (VSM) are typically used for this type of experiment, by following the material's magnetization of a material tested in a temperature-controlled cell under an applied magnetic field H delivered by an alternating current AC or a direct current DC.

A ZFC-FC experiment is used to determine a characteristic temperature for the transition between superparamagnetic and blocked states (see Figure 1.17). The protocol used for the ZFC-FC characterization of our samples is described in Chapter II section 3.7. As explained in the previous section, this temperature is called the blocking temperature T_B. It depends on the frequency used for its measurement, determining if the magnetic material is in a blocked state. [83] Below this temperature, the particle has its magnetic moment blocked and the magnetization decreases enormously. The fact that the ZFC and FC curves do not superimpose is a clear indication of superparamagnetism. It is possible to relate the blocking temperature to an average size of particles. In the ZFC curve, a clear peak indicates a narrow dispersion in particle size.

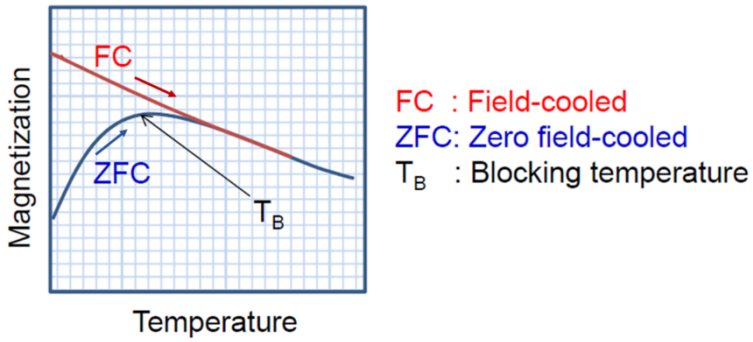

Figure 1.17: Schematic ZFC-FC measurements of magnetization performed on a superparamagnetic material. [78]

2.3.4 Magnetic anisotropy K

The blocking temperature T_B also depends on the value of the magnetic anisotropy constant K, which characterizes the magnetic properties of a material depending its nature (arrangement of its atomic spins) and its shape. [92] It has two main contribution: the magnetocrystalline

anisotropy K_1 and the shape anisotropy K_{sh}, in J.m^{-3}. A third contribution called stress anisotropy K_σ exists but will not be discussed because the materials considered here are not subjected to stress when exposed to an alternating magnetic field. [92]

$$K = K_1 + K_{sh} \quad \text{(I-9)}$$

The magnetocrystalline anisotropy K_1 is intrinsic to a material and characterizes the ease to obtain a magnetic effect on a preferential crystallographic direction. [71] Depending on the crystalline structure of the material, the spins are oriented in a particular direction more easily than the others. For iron particles, the magnetocrystalline anisotropy is 48 kJ m^{-3}, whereas for magnetite particles, it is -13 kJ m^{-3}. [71, 74, 85, 93-95]

The shape anisotropy K_{sh}, as its name suggests, depends on the different shapes of particles composing the material: spheres, cubes, cylinders. [71] The main equation used to calculate the shape anisotropy contribution is the following:

$$K_{sh} = \frac{1}{4}\mu_0 {M_s}^2 (1 - 3N) \quad \text{(I-10)}$$

where μ_0 is the vacuum magnetic permeability with $\mu_0 = 4\pi \cdot 10^{-7}$ J.A^{-2}.m^{-1}, M_s is the saturation magnetization in A.m^{-1}, also called spontaneous magnetization and N is the demagnetizing factor depending on the particle shape, with no unit. [92] Table 1.4 gathers the different possible values of the demagnetizing factor N depending on the particle shape.

Shape	Demagnetizing factor *N*
Long needle (parallel to magnetization)	0
Long needle (perpendicular to magnetization)	1/2
Sphere	1/3
Thin film (parallel to magnetization)	0
Thin film (perpendicular to magnetization)	1

Table 1.4: Demagnetization factor N for different particle shapes.

For a spherical particle, the demagnetization factor N is zero, which means that the shape anisotropy K_{sh} would be null and the magnetocristalline anisotropy K_1 would be the only one contributing to the value of the magnetic anisotropy K.

For needle-shaped particles, the value of N varies depending on the alignment of the particle in relation to the applied magnetic field H. The shape anisotropy K_{sh} shows a minimum and maximum value. For iron particles, the shape contribution to the magnetic anisotropy is comprised between - 450 and 900 kJ.m^{-3}, whereas for particles, it is comprised between - 35 and 70 kJ.m^{-3}.

Other expressions of the shape anisotropy K_{sh} in cgs units have been referenced [71, 93] such as:

$$K_{sh} = \frac{1}{2}(N_a - N_c){M_s}^2 \qquad \text{(I-11)}$$

in which, K_{sh} is measured in erg.cm^{-3}, M_s is measured in emu.cm^{-3} and $(N_a - N_c)$ are the shape factors depending on the ratio between the longest and the shortest width of the particle c/a, with some of its values referred on Table 1.5:

Shape ratio *c/a*	*(N_a - N_c)*
1.0	0.00
1.1	0.47
1.5	1.89
2.0	3.01
5.0	5.20
10	5.90

Table 1.5: $(N_a - N_c)$ factor corresponding to different shape ratios c/a between the biggest and smallest dimensions of the particle.

2.3.5 Néel/Brown relaxations

In the case of superparamagnetic particles, the magnetic moment of a nanoparticle has two stable orientations antiparallel to each other. For the nanoparticle magnetic moment to fluctuate between these two orientations, it needs to overcome an anisotropic energy barrier KV, [96]

with K the anisotropic constant due to crystalline and/or shape effects in J.m^{-3} and V the volume of the particle in m^3.

Magnetic relaxations can take place through the spontaneous realignment of a particle's magnetic moment towards its stable orientations. Néel relaxation occurs if the thermal energy k_BT sufficient move the moment from its preferred orientation. The relaxation of the moment towards its equilibrium state releases thermal energy through the rotation of the magnetic moment of the particle at high frequency. [84] This rotation occurs once a magnetic field $\vec{H}$ is applied upon the particle and it happens without macroscopic rotation of the particle.

This process is characterized by its relaxation time τ_N in s, given in by the Néel-Arrhenius equation [56, 76, 78, 83, 85-87, 89] using the attempt time τ_0 introduced in Chapter I section 2.3.2:

$$\tau_N = \tau_0 e^{KV/k_BT} \tag{I-12}$$

or by the equation modified by Brown [71-74]:

$$\tau_N = \frac{\tau_0}{2}\sqrt{\pi\frac{k_BT}{KV}}\,e^{KV/k_BT} \tag{I-13}$$

Brown relaxation is a viscous loss due to particle reorientation in a fluid; the heat is generated through shear stress with its surrounding. [84] In contrast to Néel relaxation, Brown relaxation occurs through the rotation of the particle to align its moment in the direction of the magnetic field. This process is characterised by a relaxation time τ_B in s. [76, 78, 82, 84, 86, 88, 89]

$$\tau_B = \frac{3\eta V_H}{k_BT} \tag{I-14}$$

where η is the viscosity of the material in Pa·s, V_H is the hydrodynamic volume in m^3.

In the case of a complex fluid, we can take the viscosity of the material η as being equal to the zero-shear viscosity η_0. However, one should keep in mind that other cases may emerge, in

particular when the particle's size becomes smaller than the typical distance between topological constraints (*e.g.* entanglements in a polymer melt).

An induced particle rotation is also possible for ferro/ferrimagnetic particles if it is enabled by the environment surrounding it. In this document, we shall make the distinction between Brown relaxation for single-domain superparamagnetic particles which is a spontaneous phenomenon and viscous loss friction for multi-domain ferro/ferrimagnetic particles which is provoked by the particle's reorientation in the magnetic field direction.

The apparent relaxation time τ is dominated by the shorter between the Néel and Brown relaxation times: [76, 82, 84, 86, 88]

$$\frac{1}{\tau} = \frac{1}{\tau_B} + \frac{1}{\tau_N} \tag{I-15}$$

One clear indication for the superparamagnetic behaviour is the lack of hysteresis in $M(H)$ curves (see Figure 1.14). [97] Instead, we can observe a clear sigmoidal curve with no hysteresis, which can be fitted to determine the average size of superparamagnetic particles, using Langevin's equation [71, 97]:

$$M = M_s \left(\coth(x) - \frac{1}{x} \right) \tag{I-16}$$

in which x is a dimensionless parameter given by:

$$x = \frac{m \mu_0 H}{k_B T} \tag{I-17}$$

and m is the magnetic moment of the nanoparticles.

$$m = M_{s(bulk)} V \tag{I-18}$$

2.4 Heating mechanisms

A magnetic field applied to a material can generate heat through different mechanisms. The reaction of the particle to an applied magnetic field $\vec{H}$ can vary significantly with its size and it

is crucial to know which mechanism leads directly to the heating of the particle. The different heating mechanism, such as eddy currents, domain wall motion and relaxation will be predominant in either the bulk material, multi-domain particles or single-domain particles respectively.

It should be noted that a wide dispersion of particle size could mean that several driving mechanisms may be activated, when a composite material (as it is the case in this work) is subjected to an alternating magnetic field.

2.4.1 Eddy currents

An alternating magnetic field applied to a conductive material with a size bigger than 1 cm can generate eddy currents within the material. [84] These currents formed in a closed loop in a susceptor material can cause heating through Joule heat losses. [98-100] If the material is a conductor, the inner currents generated will induce heating by Joule effect. Eddy current loss P_{eddy} in W is evaluated using the following expression [76]:

$$P_{eddy} = K_e {B_m}^2 f^2 d^2 / \rho_m \quad \text{(I-19)}$$

where K_e is a constant depending on the sample geometry in m^3, B_m is the maximum inducted magnetic field in T, f is its frequency in Hz, d is the smallest dimension transverse to flux in m and ρ_m is the material resistivity in Ω m. [76]

The effects of the magnetic field H in conductors are limited by penetration depth δ in m, depending on the resistivity ρ_m in Ω m, the permeability μ in $H.m^{-1}$ and the frequency f in Hz of the alternating field. Therefore, the size of the particles is an important parameter for a specific applied magnetic field to act upon the entirety of the particle.

$$\delta = \sqrt{\frac{\rho_m}{\mu \pi f}} \quad \text{(I-20)}$$

It is worth noting that conductive or insulator materials could be either diamagnetic, paramagnetic or ferromagnetic. Copper, aluminum and iron are conductive materials, but have different magnetic behaviors. Their magnetic susceptibility equals - $9.6 \cdot 10^{-6}$, $2.2 \cdot 10^{-5}$ and $2.0 \cdot 10^{5}$ respectively.

2.4.2 Magnetic hysteresis losses

Induction heating through magnetic hysteresis losses can happen on ferro/ferrimagnetic materials and on superparamagnetic magnetic nanoparticles possessing a high magnetic susceptibility. Here, we shall refer to all magnetic losses occurring in nanoparticles on the ferro/ferrimagnetic or on the superparamagnetic regimes (see hereafter). [82, 101]

Magnetic domain wall motion is the predominant heating mechanism for particles with a size larger than 100 nm. [84] This mechanism happens by domain wall motion and domain realignment. [84, 99] When a ferro/ferrimagnetic material is magnetized by an increasing magnetic field H, and then the field is decreased, the magnetization does not follow the initial magnetization curve. This irreversibility is called hysteresis and it can be seen by following the magnetization $M(H)$ curve (see Figure 1.14). [71, 76] The first magnetization shows a linear relation between M and H, and the slope corresponds to the value of the magnetic susceptibility χ. [75]

To explain the hysteresis, we shall detail every step in the magnetization/demagnetization. At high applied fields, the Weiss domains arrange in the direction of the magnetic field $\vec{H}$ and create a temporary magnetic dipole [98] and the magnetization approaches the saturation magnetization M_s. It is reached once all the magnetic dipoles are aligned in the direction of the magnetic field $\vec{H}$. [78] For iron particles, the saturation magnetization M_s is 1720 kA m^{-1}, whereas for magnetite particles, it is 480 kA m^{-1}. [71, 75, 94, 102]

It has been shown that the saturation magnetization M_s decreases with decreasing size of particles from the bulk value. [78] This happens because magnetic nanoparticles possess a disordered spin layer at their surface. Smaller particles have a higher ratio of surface over volume atoms. The following equation accounts for this deficiency:

$$M_s = M_s^{bulk}\left(\frac{r-d}{r}\right)^3 \qquad \text{(I-21)}$$

where r is the particle radius, d is the thickness of disordered spins and M_s^{bulk} is the bulk saturation magnetization in $A.m^{-1}$.

The saturation magnetization M_s also varies with temperature. It decreases when temperature increases until Curie temperature T_{Cu}. [78] This is logical because after the Curie temperature

T_{Cu} a ferro/ferrimagnetic material losses its magnetic properties and becomes paramagnetic. According to Bloch's law, the saturation magnetization M_s should follow the equation:

$$M_s = M_0 \left(1 - \left(\frac{T}{T_{Cu}}\right)^{1,5}\right) \quad \text{(I-22)}$$

where M_0 is the magnetization at 0 K in A.m^{-1}.

In Figure 1.18, the magnetization and the demagnetization processes are represented following the applied magnetic field. It clearly shows the hysteresis created through this process.

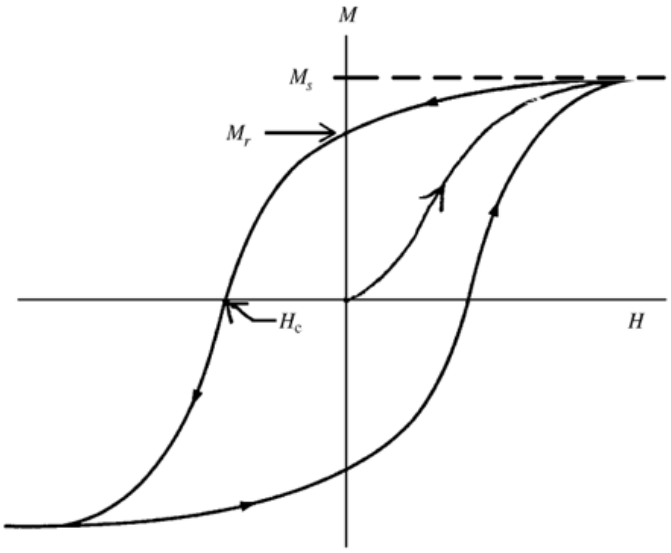

Figure 1.18: Typical ferro/ferrimagnetic material magnetization-demagnetization curve, displaying hysteresis. The first magnetization reaches the magnetic saturation M_s. The following steps for the cycle are detailed in Chapter I section 2.3.3.

The volumetric power P_{hyst}, measured in W.m^{-3}, dissipated through hysteresis loss can be calculated using the equation [76, 103]:

$$P_{hyst} = \mu_0 f \int_{-H_0}^{H_0} M(H) dH \quad \text{(I-23)}$$

where μ_0 is the vacuum magnetic permeability in H.m^{-1}, f is the frequency in Hz, H is the applied magnetic field in A.m^{-1}, H_0 is the amplitude of the oscillatory signal of the applied magnetic field in A.m^{-1} and M is the magnetization in A.m^{-1}.

SLP specific loss power (or SAR specific absorption rate) evaluates the heating performance of the magnetic particles, expressed as the heat dissipated per unit time per particle mass unit. [76, 104] The SLP is measured in W.g^{-1}.

$$SLP = \frac{P_{hyst}}{\rho\varphi} \quad \text{(I-24)}$$

where ρ is the density of the particles and φ is their volume fraction.

Through the latter equations, we can assume that heating at this scale is favored for materials possessing high saturation magnetization M_s and high susceptibility χ. [105] From a practical view, hysteresis can be maximized with increasing frequency f and applied magnetic field H.

Other articles reference an equation for the determination of SLP using cgs units [94]:

$$SLP = 10^{-7} M_s f A/\rho \quad \text{(I-25)}$$

where SLP is in W.g^{-1}, M_s is in emu.cm^{-3}, f is in Hz and A area of M/M_s as a function of H (in Oe).

Magnetic relaxation is the main heating mechanism for superparamagnetic nanoparticles. Superparamagnetic particles present no hysteresis at low frequency magnetic excitation. However, at high frequency magnetic excitation, hysteresis loss becomes possible and it can be quantified through the relaxation time τ. On the other hand, if the frequency is too high, the particles do not have the time to follow the magnetic solicitation and the hysteresis decreases. [88, 101] Therefore, the objective to maximize relaxation losses is to choose the optimal frequency for a given type of material (nature, size, agglomeration, environment).

It is possible to use the linear response theory (LRT) to estimate the theoretical value of the SLP. This method is used under certain conditions met by the geometrical and magnetic characteristics of an ensemble of magnetic particles. The SLP is calculated through the product of the hysteresis area A of the hysteresis loop and the frequency f of the applied magnetic field H, and normalized by the density of the magnetic particle to express the SLP in W.g^{-1} (see Equations I-23 and I-24). [102] For the SLP to be correctly evaluated with this theory, the size of the particle must be smaller than the single domain size D_s to allow a macrospin

approximation, but also smaller than the superparamagnetic blocking size D_{sp} for a two-level approximation through the equilibrium functions. [101]

The two-level approximation states that every superparamagnetic particle macrospin has two preferred orientations corresponding to two minima of energy. This approximation, which is only valid when the dimensionless parameter $\xi = \mu_0 H_{max} M_s V / k_B T$ is inferior to 1. In addition to LRT, this entails a linear dependence of the magnetization with the magnetic field applied and no dependence between the equilibrium functions (*i.e.*, determining the easy axis of magnetic orientation) and the magnetic particle's anisotropy. This results in two scenarios for the static susceptibility χ_0.

For magnetic particles with randomly oriented moments:

$$\chi_0 = \frac{\mu_0 {M_s}^2 V}{3 k_B T} \tag{I-26}$$

For magnetic nanoparticles, whose magnetic moment is aligned in the direction of the magnetic field:

$$\chi_0 = \frac{\mu_0 {M_s}^2 V}{3 k_B T} \left(3 - \frac{2}{1 + \left(\frac{\sigma}{3.4} \right)^{1.47}} \right) \tag{I-27}$$

with $\sigma = K_{eff} V / k_B T$ being another dimensionless parameter.

Both of these equations will lead to different expressions of the hysteresis loop area A.

For magnetic particles randomly oriented [76, 82, 84, 86, 88]:

$$A = \frac{\pi \mu_0{}^2 {H_{max}}^2 {M_s}^2 V}{3 k_B T} \frac{\omega \tau}{1 + \omega^2 \tau^2} \tag{I-28}$$

For magnetic nanoparticles aligned in the direction of the magnetic field:

$$A = \frac{\pi {\mu_0}^2 {H_{max}}^2 {M_s}^2 V}{3k_B T} \frac{\omega\tau}{1+\omega^2\tau^2}\left(3 - \frac{2}{1+\left(\frac{\sigma}{3.4}\right)^{1.47}}\right) \quad \text{(I-29)}$$

An example of calculated *SLP* curves resulting from the two scenarios are plotted in Figure 1.19 as a function of the superparamagnetic particle size d to show the distribution of specific energy generation.

The theoretical specific loss power *SLP* is then calculated from the heat generation

$$SLP = \frac{Af}{\rho\varphi} \quad \text{(I-30)}$$

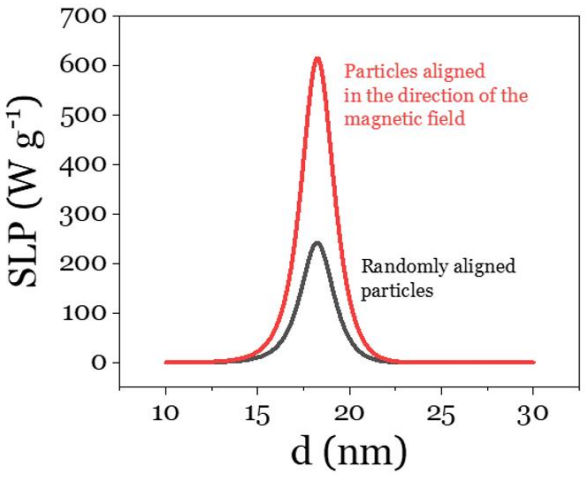

Figure 1.19: SLP distribution of Fe_3O_4 particles subjected to an alternating magnetic field of $\mu_0 H_{max}$ = 4 mT and 855 kHz at 300 K. The values of τ have been calculated with Equation I-15. In the two extreme cases of randomly oriented moments (black) and moments aligned in the direction of the magnetic field (red).

The specific loss power *SLP* is maximized at $\omega\tau \sim 1$. [76, 82, 84] Therefore, it would be wise to find the best range of frequencies for which $\omega\tau$ would be close to 1. For different particle nature, size and environment (*i.e.*, matrix or liquid), there is a preferable frequency range inducing the magnetic relaxation.

A distinction must be made between ferro/ferrimagnetic and superparamagnetic particles. For ferro/ferrimagnetic multi-domain particles, *SLP* is the product of the frequency and the hysteresis area of the magnetization curves, the latter being described through Rayleigh loops,

in accordance with equation I-23. As explained in Chapter I section 2.4.2, SLP (or SAR) has a maximum for $\omega\tau = 1$ (see Figure 1.20A) in superparamagnetic particles. The relaxation time τ depends on the nature, size and shape of the particle, and the viscosity of its environment, which means that for each combination of particle parameters, there is a matching frequency maximizing the value of SLP. As previously mentioned, dipolar interactions can decrease the apparent value of the relaxation time τ. Figure 1.20A indicates that a decrease in τ can be beneficial or detrimental to SLP if the relaxation losses are considered to be Néel-dominated [86, 106-108] or Brown-dominated. [88, 108] Figure 1.20B displays the hysteresis loops for many $\omega\tau$ values, illustrating the importance of having a frequency matching the relaxation time τ. We consider that most characterization of magnetic particle heating efficiency are performed at AC magnetic fields between 100 and 700 kHz.

As for the influence of the amplitude of the magnetic field on superparamagnetic particles, SLP will increase with the square of the amplitude H, [88, 109, 110] as expected from equations I-28 and I-29, and with the cube of H for ferro/ferrimagnetic particles. [110]

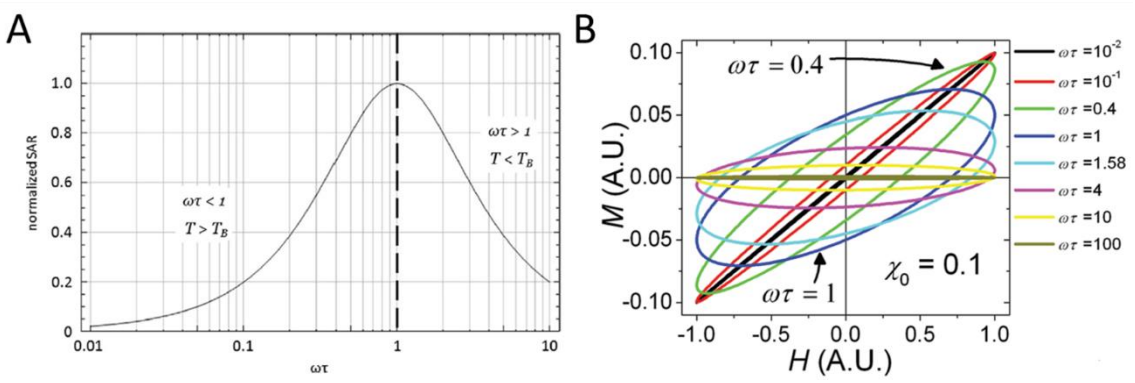

Figure 1.20: (A) Normalized SAR as a function of ωτ from equations I-28 and I-30 applicable to superparamagnetic particles. A maximum for SAR is seen for ωτ = 1, in accordance with the Rosensweig model, supposing a system of non-interacting particles. [84] (B) Hysteresis loops for different values of ωτ. [101]

The formation of nano-assemblies of particles in a medium (*i.e.*, as fillers in a composite material) poses a problem for predicting and interpreting the heat efficiency through magnetic induction. Some studies have aimed at preventing agglomeration or precipitation of particles in the liquid state. [111] In well-dispersed particles, the interaction is weak and non-relevant and the magnetic behavior can be associated to that of an individual nanoparticle. Whereas concentrated samples lead to a collective behavior, as the interactions become more relevant. [112] The Interacting SuperParamagnetic (ISP) model suggests that nanostructures can be

considered as a single entity a larger magnetic moment and volume, although the behavior of the whole structure seems more complex as the magnetic moments will mainly interfere between them.

Most these studies have been performed on well-dispersed suspensions of magnetic particles in an environment with low viscosity. Even though this is not the case for the materials presented in this manuscript, we should keep in mind that the progresses and the interpretations will help us better understand the magnetic behavior of the particles used in this work.

In conclusion, all the heating mechanisms previously mentioned lead to particles interacting differently with a magnetic field. Each of them can be the predominant method of heating depending on the particle size. Magnetic and electric properties, as well as the environment itself and the degree of agglomeration, are the main factors, which will determine the amplitude of this effect. An additional mechanism for induction heating exists (*i.e.*, "induced friction"), although we have chosen to detail it in an upcoming section, as it is wiser to introduce it once the thermal and rheological behavior of each composite has been presented.

In this work, we chose to use different iron Fe and magnetite Fe_3O_4 particles for their high susceptibility to the magnetic field and therefore high potential heating capacity. Different filler fractions are selected for our nanocomposites to be able to tune the heating rate and the maximum temperature accessible. This is particularly relevant in this study because we aim at targeting a fast healing of our materials in a specific range of temperature.

3 Induction heating on magnetic nanocomposites

As previously stated in the Introduction, we have decided to approach the concept of repairing a material using healing-on-demand based on induction heating, instead of self-healing. Therefore, this part will be restricted to detailing the most relevant works on induction heating performed on polymer-based nanocomposites. First, we will explain and justify the mechanical and rheological properties required for a material to be healed. Then, we will justify our choice for using TPEs in this works. Finally, we will present the need for a multi-physics approach taken for the full comprehension of the magnetic induced healing.

3.1 Specifications

In this part, we will determine the criteria for a TPU to be healed through magnetic induction. The primary aspect to take into consideration is the targeted temperature (see Figure 1.21). The magnetic composite needs to be able to heat over its melting point to flow, triggering polymer diffusion and thus repair the defect. Furthermore, this healing procedure is limited by the thermal degradation of the TPU matrix (*i.e.*, usually around 250°C for TPUs). [113] Therefore, there is a range of temperatures that could interest us for healing our material. For the TPU used in this work (*i.e.*, Desmopan 85085A), the corresponding range would be from 150 to 200 °C, although the optimal temperature will be set in Chapter III.

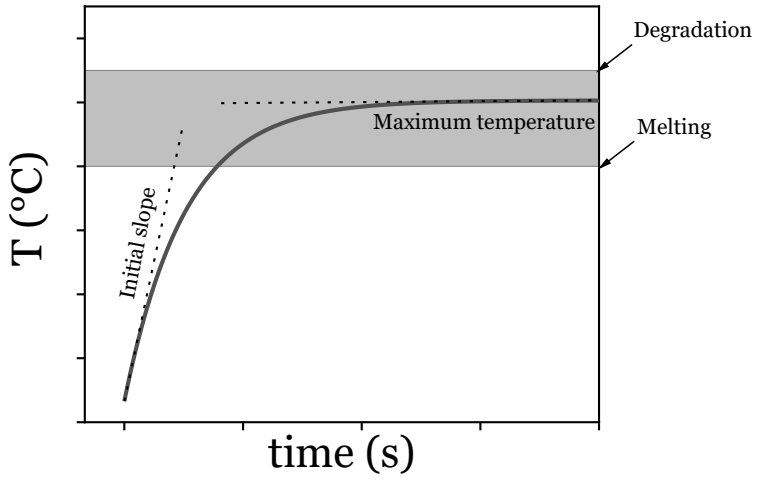

Figure 1.21: Temperature profile of a magnetic composite through induction heating.

For a given setup (*i.e.*, magnetic inductor geometry, alternating magnetic field amplitude and frequency, inductor-sample distance), the ability of a magnetic composite to generate heat is dictated by its magnetic fillers. Increasing the filler fraction will lead to an increase of the heating rate and the maximum temperature attained. At the same time, we must limit the concentration in magnetic particles, as these can affect the mechanical and rheological properties of our neat polymer (*e.g.*, fragility, gelation). [10, 114, 115] Gelation hinders the TPU's capacity to flow above its melting point as the material presents a gel-like structure. Additionally, at the solid state, the strain at fracture (and energy at failure) decreases with increasing filler fraction. Both of these effects should be avoided by limiting the magnetic fillers content. Particle/particle or particle/matrix interactions lead to these changes (see Figure 1.22), and are made more evident with increasing filler content. Indeed, we have limited our study to composites filled with 15 vol.% in magnetic particles, to limit the effects on mechanical and rheological properties. SAR can be improved differently depending on nanoparticle characteristics (*i.e.*, nature and size). Note that limiting filler content also works in the mindset of the thesis (*i.e.*, insisting in the low-cost aspect of the processes).

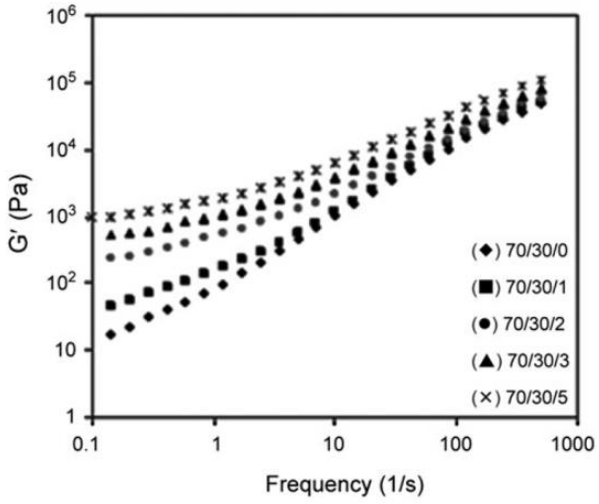

Figure 1.22: Storage shear modulus versus frequency of TPU/PCL composites filled with magnetite nanoparticles."70/30/X" denotes the TPU/PCL weight ratio and X the magnetic filler content in weight percentage, adapted from [115].

According to Equation I-28, the magnetic field amplitude has a clear positive effect on SAR, whereas frequency will have different effects depending on the predominant heating mechanism, which is linked to the nature and the size of the magnetic particles. Having a different setup subjecting the sample to a higher magnetic field amplitude and at an optimal

frequency may allow for the same temperature to be reached for a material with reduced magnetic filler content. [116, 117]

In this study, we have determined that the material also needs to flow under a reasonable timescale (i.e., for terminal relaxation time below 0.01 s). This aspect is linked to the temperature and to the average molecular weight of the TPU. The former should be sufficiently high over the glass transition and the latter should be comprised between 20 and 60 $kg.mol^{-1}$. [118]

The rheological behavior of our TPU is also of major importance. After reaching the TPUs melting point, it is typical for the storage G' and loss G'' moduli to highly decrease. The flow of the material occurs in a reasonably timescale for healing (≈ 1 min) if G'' is at least ten times higher than G' and we believe that the viscosity of the matrix should be around 100 Pa s at the molten state so that the TPU would be able to flow sufficiently. We must take into account the possibility of gelation in the composites with higher filler fraction. [115] The value of the viscosity does not decrease as much as it should to enable the healing of the material and thus, it would not be relevant for the application.

Table 1.6 assembles the different specifications needed for the healing process to occur effectively.

Variables	*Values*
Temperature range (°C)	150 – 200
Filler content (vol.%)	1 – 15
Viscosity at the molten state (Pa s)	~ 100
Energy at failure (MJ m^{-3})	50 – 200

Table 1.6: Summary of relevant parameters for magnetic induced healing.

3.2 State of the art on induction healing in polymer nanocomposites

Here, we will focus on the state of the art for different types of polymer-based magnetic nanocomposites. Several research teams have shown their interest for induction heating applied to polymer matrixes, not only for healing-on-demand, [9, 10, 87, 119] but also for magnetoactive composites, [120] shape recovery [9, 121] and 3D printing of magnetically

designed structures. [122] Different types of polymers are used in these studies depending on the targeted application: thermoplastic polymers, thermoplastic elastomers and ionic gels.

In most cases the concept of mechanical recovery has been defined as the ratio between the elongation at break of an original and a healed sample. [9, 10, 123, 124]

The pioneering work of Cordier *et al.* presented a **supramolecular network** capable of spontaneous recovery of its tensile properties after 180 minutes with stress-strain curves superposing perfectly. [125] The recovery of the elongation at break increases gradually with time (over a few hours), therefore this approach is highly dependent of the time required for the full healing to occur and the materials' sensitivity to moisture. As the time necessary for healing to occur efficiently is too high, some studies [126] incorporated the concept of stimulus healing into unentangled materials to assist and to accelerate this process. Magnetic particles are added as fillers in supramolecular networks (see Figure 1.23A) to assist through the generation of heat through magnetic induction. Two ionic aggregates were used for supramolecular studies: terpyridine (TPy) and ureidopyrimidinone (UPy), filled with magnetite Fe_3O_4 particles. [126, 127] Figure 1.23B shows that, even after 2h of magnetic-assisted healing at 110.1 kHz and 20 $kA.m^{-1}$, resulting in a temperature of 55 °C, the mechanical recovery of the UPy-based composite, filled with 20 wt.% in magnetic particles, is not optimized. It should be noted that the tensile stress and tensile stress of these materials are not sufficient to match the mechanical properties required for our study.

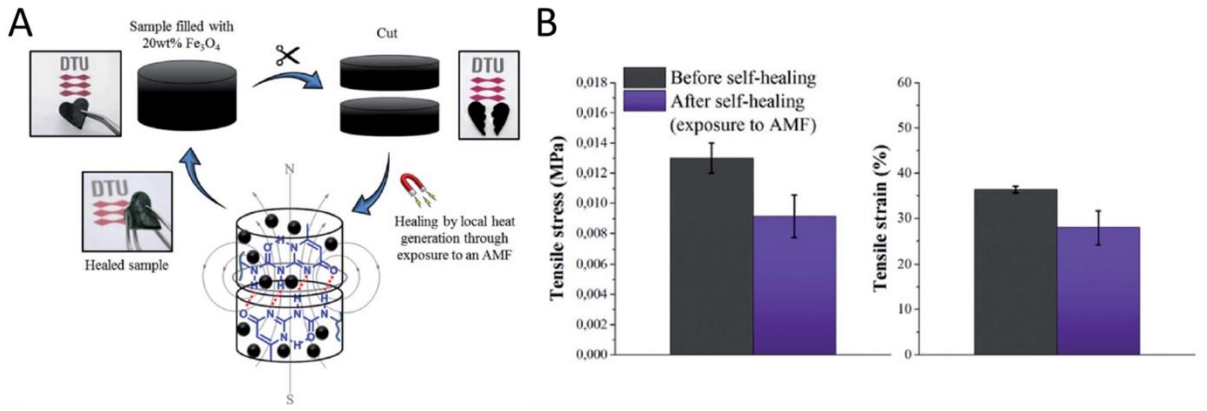

Figure 1.23: (A) Schematic illustration of induction heating used to assist in UPy-based healing. (B) Tensile stress and tensile strain of the corresponding materials filled with 20 wt.% in Fe_3O_4 particles before and after healing assisted by induction heating at 55°C for 2h. Both are adapted from [126].

Magneto responsive ionomeric composites, capable of healing with the assistance of an AC magnetic field, have also been studied by Hohlbein *et al*. [123] The magnetic fillers considered

where Fe_3O_4 and $CoFe_2O_4$ with different shapes and sizes, such as spheres (15 to 200 nm in radius), cubes (200 nm in side length) and rods (500 nm in length and 55 nm in width). Composites of 0.03 to 0.4 vol.% in magnetic fillers were prepared and a characterization of their magnetic and rheological properties was performed. To determine the healing efficiency of these materials, samples were cut in half and then either healed inside an oven at 70°C or through magnetic induction at 31.5 $kA.m^{-1}$ with a frequency of 250 kHz (see Figure 1.24A). The best results in mechanical recovery were obtained through magnetic induction with composites filled with 0.05 vol.% in 200 nm cubic Fe_3O_4 with a *SAR* value of 69.4 W/g reaching a temperature of 100°C in 15 minutes (see Figure 1.24B-C). The composite healed through magnetic induction has a recovery of the elongation at break evaluated at over 95% for 15 minutes, breaking at 1.15 MPa in stress for 345% strain.

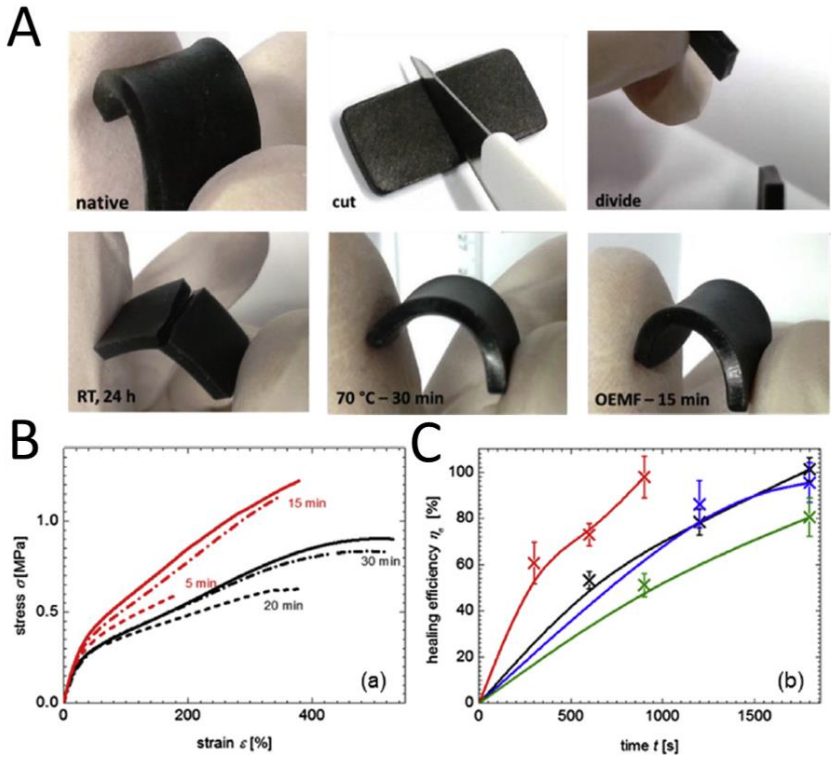

Figure 1.24: (A) Illustration of the repairing process applied to a cut sample. (B) Strain-stress curves of native (straight lines) and healed (dashed lines) samples of ionomer (black) and ionomer filled with cubic 0.05 vol.% in Fe_3O_4 (red), indicating the time used for healing. (C) Evolution of healing efficiency over time of the ionomer (black) and the ionomer filled with 0.05 vol.% in Fe_3O_4 (blue) healed in the oven at 70°C, the ionomer filled with 0.03 and 0.05 vol.% in Fe_3O_4 (green and red respectively) healed through magnetic induction. This figure is adapted from [123].

Induced healing of supramolecular polymers shows promising results on recovery of mechanical properties, although this process required a relatively long time. On top of this,

supramolecular materials are lacking in strong mechanical properties, presenting an elastic and shear modulus below 1 MPa due to the unentangled nature of its polymer chains. This discards them as possible materials for the intended applications in this work. [123]

Thermoplastic polymers can be either amorphous or semi-crystalline and can be melt-processed under heating. They present higher values of Young's modulus up to 4.5 GPa below their glass transition temperature, and high elongations at break up to 300% in its vicinity , a wide range of glass transition T_g and melting point T_m from -135 to 290°C and from 105 to 345°C respectively. [128, 129] The temperature to consider to evaluate the possibility of healing for these materials is the melting temperature T_m for semi-crystalline and T_g for amorphous ones. Above these temperatures, the material flows and the sample can be repaired (see Figure 1.25A) because of the reversible aspect of this transition. These materials can be easily reshaped and recycled.

Several research groups have focused their attention on applying magnetic induction on these materials to repair them. [10, 87, 98, 119, 130] Figure 1.25B shows the strain cycles undergone by Mn-Zn ferrite composites with a thermoplastic matrix and its respective recovery step, confirming that these materials can be repaired if needed. Ramanujan *et al.* have also proposed a series of magnetic composites filled with Mn-Zn ferrites (*i.e.*, $Mn_xZn_{1-x}Fe_2O_4$), [10, 119] based on polymer poly(ethylene-co-vinyl acetate) EVA matrixes as healable rubbers with promising shape recovery through many cycles and repairable after fracture. Composites with 10-20 wt.% in Mn-Zn ferrites were prepared, with particle sized ranging from 12 to 15 nm leading up to 50 MPa for the storage modulus at room temperature for the composite with the highest filler fraction (*i.e.*, 20 wt.%), determined through DMA. The healing process shows a near perfect recovery of the strain at failure and the elastic modulus, however the tensile stress at failure is lower for the healed samples. All of them presented high shape recovery over three cycles of uniaxial stretching from 96.7 to 100%. In these particular cases, the recovery is given as the ratio between the tear strength of an original and a healed sample. The healing process was deemed effective and the restoration of the sample was reached after 10 minutes of exposure to the magnetic field at 475 kHz with an amplitude of 4 $kA.m^{-1}$.

While in most cases, the choice for magnetic filler is made depending on heating efficiency, here the Curie temperature of the Mn-Zn ferrite (*i.e.*, 230°C) works as a temperature limit for induction heating, preventing polymer degradation. As explained in Chapter I section 2.2,

atomic magnetic moments are no longer correlated above the Curie temperature, resulting in the disappearing of Bloch walls and a sudden drop of SAR. The Mn-Zn ferrite Curie temperature can also be tuned between 190 and 280°C by adjusting the Mn to Zn ratio. [119] This can be advantageous for heating the composite while avoiding polymer degradation.

Other thermoplastic matrixes can potentially be used for healing thermoplastic materials. For each of these materials, their respective melting points must be considered as the targeted temperatures required for effective healing. [98]

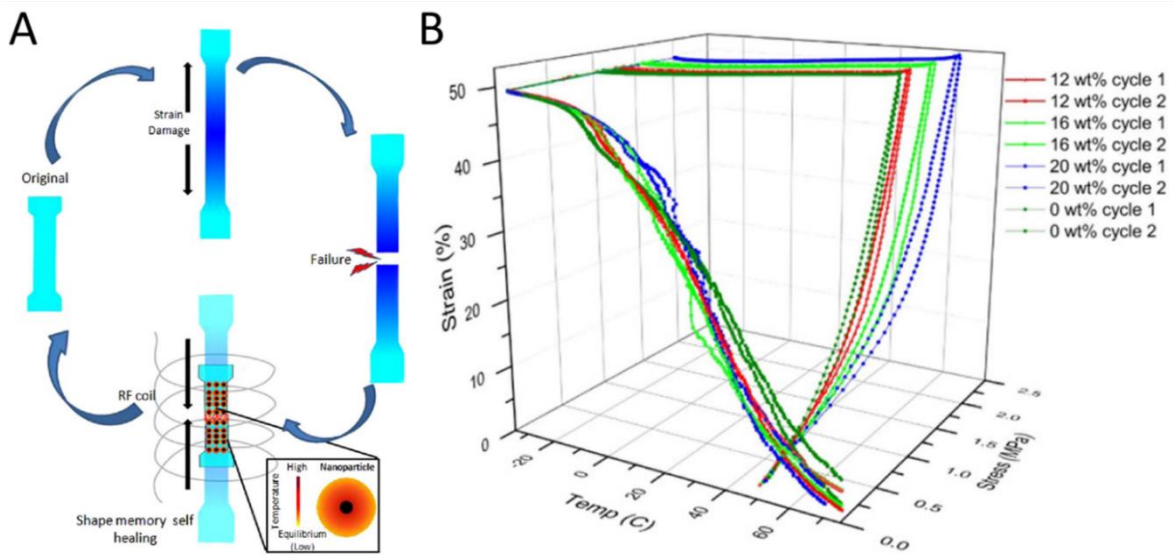

Figure 1.25: (A) Schematic representation of the damage-healing cycle of a thermoplastic tensile sample. The sample is stretched up to the failure. Then, the sample is healed and the original shape is recovered through magnetic induction heating. (B) DMA measurements of the same thermoplastic samples filled with up to 20 wt.% in $Mn_{0.8}Zn_{0.2}Fe_2O_4$, following two cycles of strain and recovery without reaching its rupture. This figure is adapted from [10].

Composites with extremely low magnetic filler content have also proven to be candidates for induction healing with the condition of using an induction machine the proper characteristics for improving SAR. Thermoplastic polymers such as polypropylene and polymethyl methacrylate have been used for the production of composites with low content in maghemite γ-Fe_2O_3 (*i.e.*, under 0.25 vol.%). [116, 117] In particular, composites filled with maghemite treated with polyethylene glycol γ-Fe_2O_3@PEG have shown largely better results than those filled solely with maghemite. The PMMA composites with 0.23 vol.% in filler content have indicated that it is possible to obtain above 95% recovery for materials following 100 cycles of cracking and healing. This process occurs for 40-60 minutes under a magnetic field amplitude

of 10 kA.m^{-1} and a frequency of 968 kHz. The remarkable results and repeatability of the healing process is due to the long period of time attributed to it, the high magnetic field amplitude, and the ability for particles to diffuse through the heated matrix during the procedure (see Figure 1.26). Diffusion of magnetic fillers, towards the crack or surface defect, is aided by the high frequency alternating magnetic field and the heat induced by it. The density of particles increases around the crack, thus increasing the SAR locally and accessing higher temperatures.

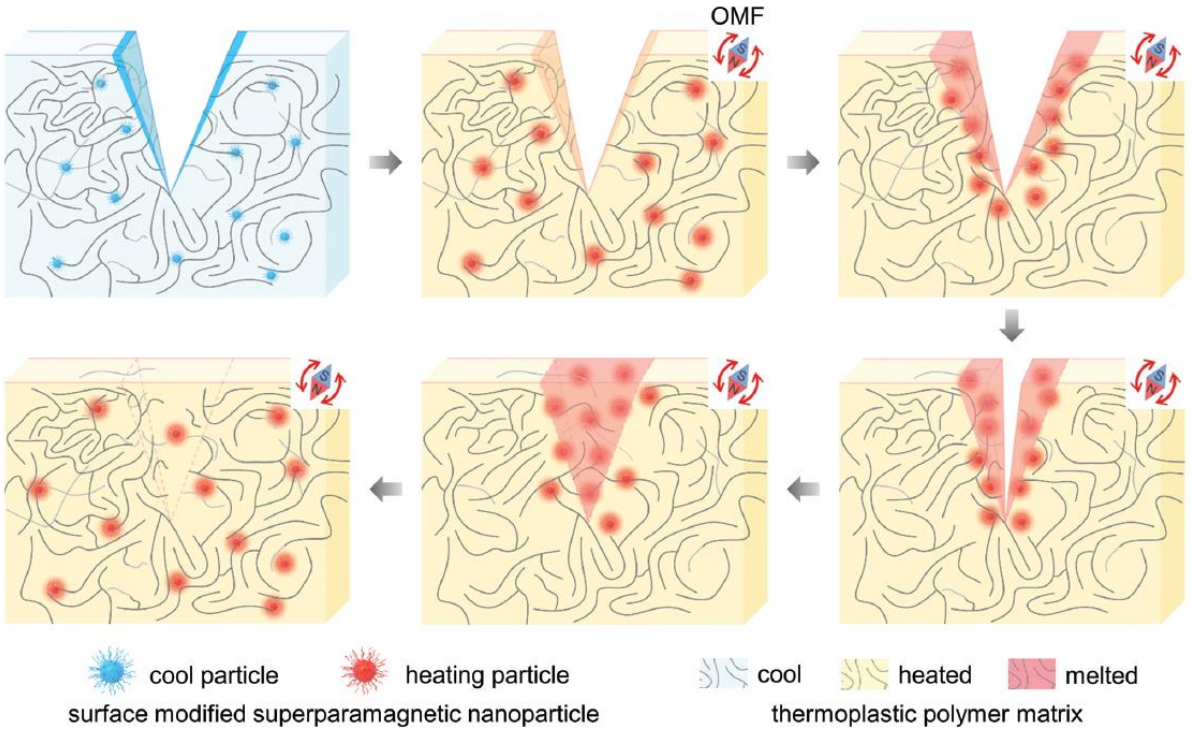

Figure 1.26: Illustration depicting the healing steps occurring during the induction healing process, adapted from [117].

Elastomers are interesting in this sense as they have a viscoelastic mechanical behavior, capable to deform under extreme solicitations. Several teams have studied the possibility of healing elastomer-based material. [9] The use of a magnetic field has been proven useful for shape recovery of a composite (see Figure 1.27A) produced with an elastomer such as acrylonitrile butadiene rubber NBR. [9] Such samples underwent up to four cycles of strain and magnetic induced shape recovery with an AC field of 4 kA.m^{-1} at 375 kHz. Composites filled with 20 wt.% in Mn-Zn ferrite showed promising results for repairing damages samples damage (see Figure 1.27B). This sample was stretched up to its fracture. The shape of both parts was recovered with the use of the AC magnetic field. Then, both ends were put together within the

coil and the magnetic field was applied for 10 minutes. The samples followed this procedure four times and the strain-stress performances are reported in Figure 1.27C, with the measurements being made up to 300% in strain. The sample filled with 20 wt.% in magnetic particles showed the best results for mechanical recovery with the composite reaching a temperature plateau at 148°C after 5-6 minutes. In this case, the repairing is not as optimized as it is the case for thermoplastic materials. The clear solution would be to look for materials benefitting from the advantages brought from thermoplastic and elastomer polymers.

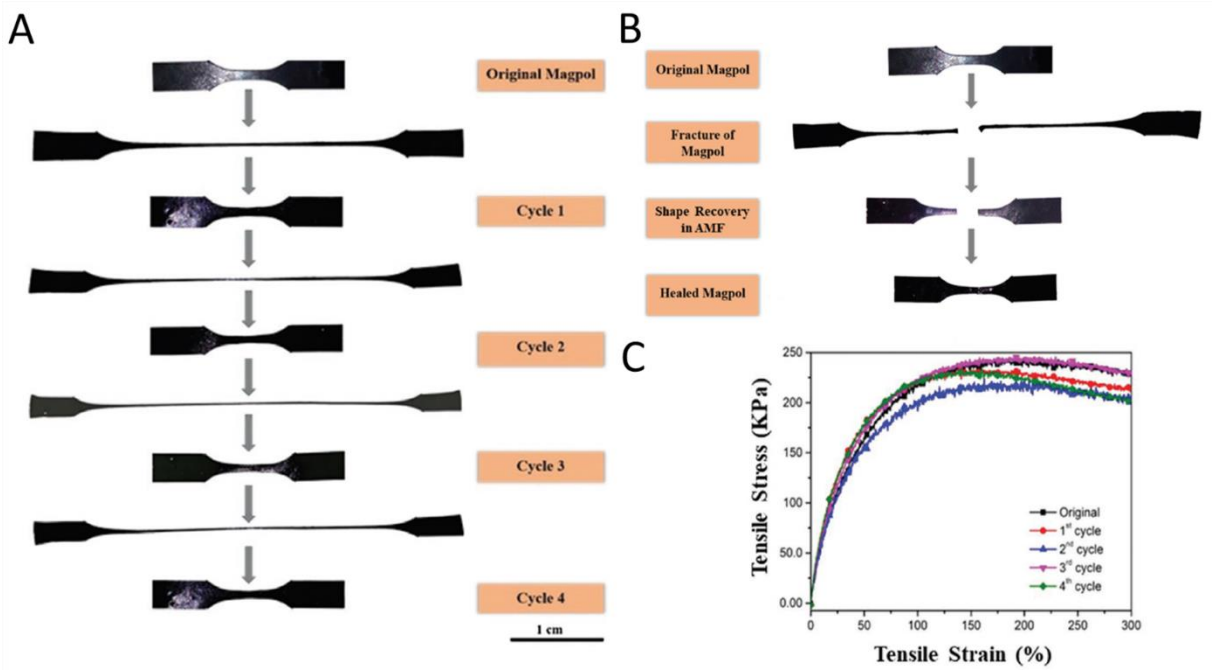

Figure 1.27: (A) Shape recovery and (B) induced healing of a tensile dumbbell magnetic polymer Magpol. (C) Stress-strain curves for native and healed Magpol samples after 1-4 cycles. Figures adapted from [9].

The ensemble of references in this section show that a full multi-disciplinary study (*i.e.*, structural, rheological, magnetic, mechanical characterizations) on polymer-based magnetic composites has not been made systematically and we shall focus on justifying the advantages of doing so. Considering all the sample properties and the machine settings presented in this section, we justify our choice, directed towards thermoplastic polyurethanes TPUs, a group of thermoplastic elastomers TPEs combining all the advantages from the thermoplastic polymer previously mentioned and the rubber-like behavior. TPUs are expected to have their properties improved (*i.e.*, thermal, mechanical, rheological) or new ones bestowed (*i.e.*, electric, magnetic) by increasing the magnetic filler content. The reinforcement determined with the TPU and the

composite's Young's modulus is expected to increase with filler fraction, while strain at break should decrease as filler fraction increases. [131]

3.3 Multi-physics approach for heat production rationalization

We have previously stated the properties necessary to ensure the flow of the material and we have justified our choice for the matrix while comparing the recent induction healing studies performed on polymer-based composites. Here, we focus our interest in optimizing the induction healing performance. The previous section has shown outstanding healing results for different polymer-based magnetic composites, although none of the studies have presented a full multi-physics characterization of the sample and the healing process. A more complete and in-depth characterization is necessary to rationalize the overall behavior with the hope of improving our understanding of the physics of induction-driven healing.

Electric and magnetic properties determine the SAR of the material subjected to an alternating magnetic field through many possible heating mechanisms, as presented in Chapter I section 2.4. The impact of the chemistry, the size, the morphology and the aggregation of particles on the materials' ability to produce heat has been investigated. [82] In fact, magnetic susceptibility, coercivity and magnetic saturation, which are directly linked to hysteresis losses (and SAR), will vary depending on the nature of the particles. [97, 132-137] On the other hand, Joule losses will only be relevant if the material's electric conductivity is sufficient.

Beyond magnetic characteristics, mechanical ones also play an important role in affecting SAR. In fact, if the viscosity is sufficiently low, the magnetic particles can form two types of nano-assemblies under an applied AC magnetic field: nanochains or nanoclusters (see Figure 1.28). The formation of perfectly aligned nanochains has shown to be beneficial for heat generation, [138, 139] whereas the formation of nanoclusters have been mostly detrimental. [82, 86, 94, 96, 106, 127, 139] A nanochain can be considered an assembly of nanoparticles with their magnetic moments locked together. Magnetic moments will react together to the magnetic field applied. Increasing filler fraction can lead to the formation of undesired nanoclusters. Dipole-dipole interactions may modify the energy barrier KV, which must be overcome by the thermal energy for the nanoparticle's magnetic moment to switch to the other stable orientation. This tends to decrease the characteristic relaxation time of the nanoparticle, which might increase or decrease the heating efficiency of the particles. Thus, the induction heating efficiency is dependent on the dispersion state of the particle inside the matrix.

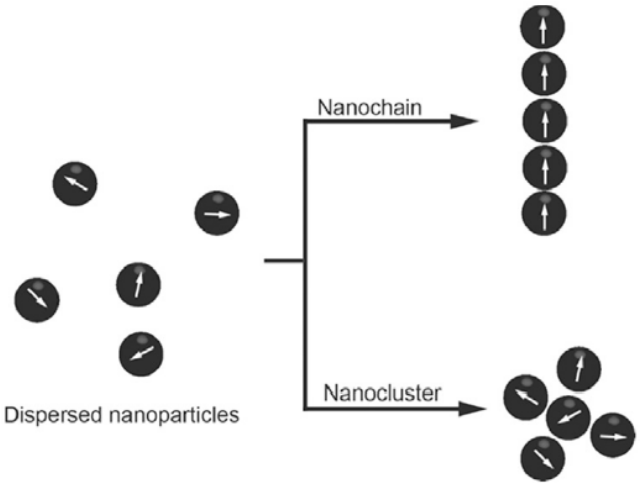

Figure 1.28: Two possible arrangements for nanoparticles under an AC magnetic field, adapted from [82].

Finally, the fall in viscosity at the molten state might lead to additional responses to the alternating magnetic field, thus increases the SAR, indicating a direct impact of the TPU's mechanical properties on the magnetic induced heat generation. Some studies have reported the presence of another heating mode appearing at the melting point with two different thermoplastic matrixes, (*i.e.*, high density polyethylene HD-PE and polyamide 6 PA-6). [98] Once the temperature reaches the polymers' respective melting point, an additional heating mechanism seems to appear systematically. This is due to the decrease in viscosity in the material once it reaches its melting point, leading to an increase in SAR. At this point, the magnetic fillers have a higher degree of mobility and this could lead to heat generation through friction with the matrix. This represents an important aspect to take into account once we heal our composites, as it is essential to reliably control the temperature profiles.

Figure 1.29 illustrates two different possible heating behaviors resulting from ferromagnetic particles embedded in a matrix having a phase transition. The crossing of solid to liquid transition temperature T_m of the gel leads to a sharp increase of the temperature. This phenomenon is attributed to the viscosity drop, allowing particle movement (rotation at high frequency, following $\vec{H}$), and therefore enabling an additional heating mechanism based on friction between the filler and the matrix. Such a heating mechanism has also been reported by Yassine *et al.* on hydrogels. [140]

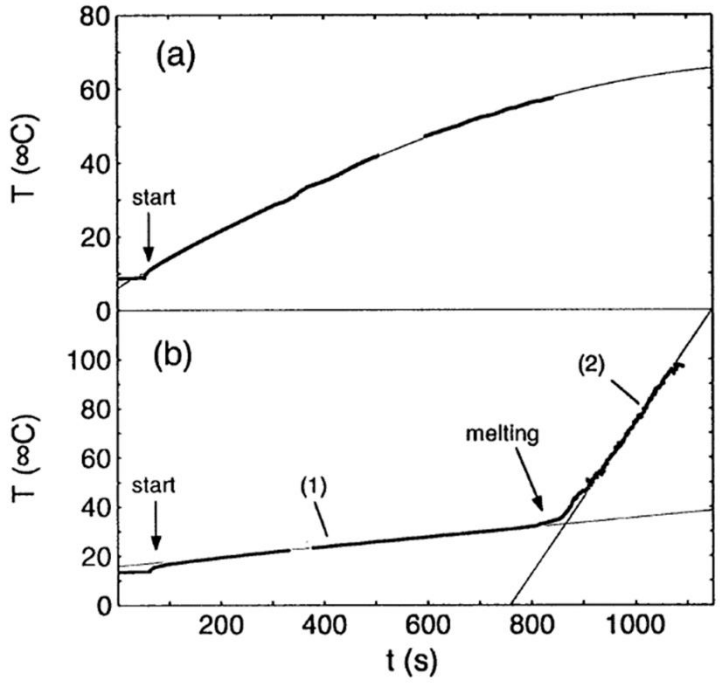

Figure 1.29: Temperature profile for the heating of a magnetic particles in (a) a ferrofluid and (b) suspended in a gel capable of melting, adapted from [110].

The dependence of SAR on the multiple properties of the material (*i.e.*, magnetic, electrical, structural, rheological) proves the crucial need for a multi-physics study. The characterization of the structure of TPUs and their thermal behavior are crucial if we intend to have a reliable understanding of the response to magnetic induction.

To conclude this section, the fundamental concepts required for understanding this work have been described. The characteristics of thermoplastic elastomers have been listed, with an emphasis on the link between their structure and their properties. Basics concepts of magnetism and magnetic induction under an oscillatory magnetic field have been detailed. Finally, the state of the art for induction heating on polymer-based nanocomposites has helped in situating our work in this growing literature, emphasizing the importance of a multi-physics study.

References

[1] G. Holden, E. T. Bishop and N. R. Legge, "Thermoplastic elastomers," in Journal of Polymer Science Part C: Polymer Symposia, 1969.

[2] E. T. Bishop and S. Davison, "Network characteristics of the thermoplastic elastomers," in Journal of Polymer Science Part C: Polymer Symposia, 1969.

[3] L. Leibler, "Theory of microphase separation in block copolymers," Macromolecules, vol. 13, p. 1602–1617, 1980.

[4] M. W. Matsen and M. Schick, "Stable and unstable phases of a linear multiblock copolymer melt," Macromolecules, vol. 27, p. 7157–7163, 1994.

[5] G. H. Fredrickson and E. Helfand, "Fluctuation effects in the theory of microphase separation in block copolymers," The Journal of chemical physics, vol. 87, p. 697–705, 1987.

[6] G. H. Fredrickson, A. J. Liu and F. S. Bates, "Entropic corrections to the Flory-Huggins theory of polymer blends: Architectural and conformational effects," Macromolecules, vol. 27, p. 2503–2511, 1994.

[7] F. S. Bates and G. H. Fredrickson, "Block copolymer thermodynamics: theory and experiment," Annual review of physical chemistry, vol. 41, p. 525–557, 1990.

[8] F. S. Bates and G. H. Fredrickson, "Block copolymers-designer soft materials," Physics today, vol. 52, 2000.

[9] R. Panigrahi, M. Zarek, V. Sharma, D. Cohn and R. V. Ramanujan, "Bio-Inspired Multiple Cycle Healing and Damage Sensing in Elastomer–Magnet Nanocomposites," Macromolecular Chemistry and Physics, vol. 220, p. 1900168, 2019.

[10] A. S. Ahmed and R. V. Ramanujan, "Magnetic field triggered multicycle damage sensing and self healing," Scientific reports, vol. 5, p. 1–10, 2015.

[11] G. P. Baeza, "The reinforcement effect in well-defined segmented copolymers: Counting the topological constraints at the mesoscopic scale," Macromolecules, vol. 51, p. 1957–1966, 2018.

[12] G. P. Baeza, "Recent advances on the structure–properties relationship of multiblock copolymers," Journal of Polymer Science, vol. 59, p. 2405–2433, 2021.

[13] M. Nébouy, A. Louhichi and G. P. Baeza, "Volume fraction and width of ribbon-like crystallites control the rubbery modulus of segmented block copolymers," Journal of Polymer Engineering, vol. 40, p. 715–726, 2020.

[14] M. Nébouy, J. Morthomas, C. Fusco, G. P. Baeza and L. Chazeau, "Coarse-grained molecular dynamics modeling of segmented block copolymers: impact of the chain architecture on crystallization and morphology," Macromolecules, vol. 53, p. 3847–3860, 2020.

[15] N. Candau, E. Vives, A. I. Fernández and M. L. Maspoch, "Elastocaloric effect in vulcanized natural rubber and natural/wastes rubber blends," Polymer, p. 124309, 2021.

[16] T. A. Huy, R. Adhikari, R. Weidisch, G. H. Michler, K. Knoll and others, "Influence of interfacial structure on morphology and deformation behavior of SBS block copolymers," Polymer, vol. 44, p. 1237–1245, 2003.

[17] M. A. Van Dijk and R. Van den Berg, "Ordering phenomena in thin block copolymer films studied using atomic force microscopy," Macromolecules, vol. 28, p. 6773–6778, 1995.

[18] R. Van den Berg, H. De Groot, M. A. Van Dijk and D. R. Denley, "Atomic force microscopy of thin triblock copolymer films," Polymer, vol. 35, p. 5778–5781, 1994.

[19] S. Jangareddy, T. Sun, A. B. Burns and R. A. Register, "Blends of Polyisoprene with Model Styrene–Olefin Copolymers: Mixing Energetics in Blends versus Block Copolymers," Macromolecules, vol. 54, p. 3999–4009, 2021.

[20] J. L. Adams, W. W. Graessley and R. A. Register, "Rheology and the microphase separation transition in styrene-isoprene block copolymers," Macromolecules, vol. 27, p. 6026–6032, 1994.

[21] N. Candau, G. Stoclet, J.-F. Tahon, A. Demongeot, E. Yilgor, I. Yilgor, Y. Z. Menceloglu and O. Oguz, "Mechanical reinforcement and memory effect of strain-induced soft segment crystals in thermoplastic polyurethane-urea elastomers," Polymer, vol. 223, p. 123708, 2021.

[22] X. Kong, S. Tan, X. Yang, G. Li, E. Zhou and D. Ma, "Isothermal crystallization kinetics of PEO in poly (ethylene terephthalate)–poly (ethylene oxide) segmented copolymers. I. Effect of the soft-block length," Journal of Polymer Science Part B: Polymer Physics, vol. 38, p. 3230–3238, 2000.

[23] T. J. Hermel, L. Wu, S. F. Hahn, T. P. Lodge and F. S. Bates, "Shear-induced lamellae alignment in matched triblock and pentablock copolymers," Macromolecules, vol. 35, p. 4685–4689, 2002.

[24] T. J. Hermel, S. F. Hahn, K. A. Chaffin, W. W. Gerberich and F. S. Bates, "Role of molecular architecture in mechanical failure of glassy/semicrystalline block copolymers: CEC vs CECEC lamellae," Macromolecules, vol. 36, p. 2190–2193, 2003.

[25] A. Hotta, E. Cochran, J. Ruokolainen, V. Khanna, G. H. Fredrickson, E. J. Kramer, Y.-W. Shin, F. Shimizu, A. E. Cherian, P. D. Hustad and others, "Semicrystalline thermoplastic elastomeric polyolefins: Advances through catalyst development and macromolecular design," Proceedings of the National Academy of Sciences, vol. 103, p. 15327–15332, 2006.

[26] M. Vatankhah-Varnosfaderani, A. N. Keith, Y. Cong, H. Liang, M. Rosenthal, M. Sztucki, C. Clair, S. Magonov, D. A. Ivanov, A. V. Dobrynin and others, "Chameleon-like elastomers with molecularly encoded strain-adaptive stiffening and coloration," Science, vol. 359, p. 1509–1513, 2018.

[27] F. Auriemma, R. Di Girolamo, G. Urciuoli, M. R. Caputo, C. De Rosa, M. Scoti, A. Malafronte, R. Cipullo, V. Busico, N. Grizzuti and others, "Transmission electron microscopy analysis of multiblock ethylene/1-octene copolymers," Polymer, vol. 193, p. 122347, 2020.

[28] P. Zhu, C. Zhou, X. Dong, B. B. Sauer, Y. Lai and D. Wang, "The segmental responses to orientation and relaxation of thermoplastic poly (ether-ester) elastomer during cyclic deformation: An in-situ WAXD/SAXS study," Polymer, vol. 188, p. 122120, 2020.

[29] B. B. Sauer and W. G. Kampert, "Tensile deformation and morphology changes in segmented elastomer films and fibers including mechanical property modeling," Journal of Applied Polymer Science, vol. 137, p. 49315, 2020.

[30] G. J. E. Biemond, J. Feijen and R. J. Gaymans, "Influence of polydispersity of crystallizable segments on the properties of segmented block copolymers," Polymer Engineering & Science, vol. 48, p. 1389–1400, 2008.

[31] L. Bai, Z. Hong, D. Wang, J. Li, X. Wang, G. Pan, L. Li and X. Li, "Deformation-induced phase transitions of polyamide 12 in its elastomer segmented copolymers," Polymer, vol. 51, p. 5604–5611, 2010.

[32] G. P. Baeza, A. Sharma, A. Louhichi, L. Imperiali, W. P. J. Appel, C. F. C. Fitié, M. P. Lettinga, E. Van Ruymbeke and D. Vlassopoulos, "Multiscale organization of thermoplastic elastomers with varying content of hard segments," Polymer, vol. 107, p. 89–101, 2016.

[33] N. J. Sijbrandi, A. J. Kimenai, E. P. C. Mes, R. Broos, G. Bar, M. Rosenthal, Y. Odarchenko, D. A. Ivanov, P. J. Dijkstra and J. Feijen, "Synthesis, morphology, and properties of segmented poly (ether amide) s with uniform oxalamide-based hard segments," Macromolecules, vol. 45, p. 3948–3961, 2012.

[34] U. Bandara and M. Dröscher, "The two-phase structure of segmented block copoly (ether ester)," Colloid and Polymer Science, vol. 261, p. 26–39, 1983.

[35] G. Wegner, T. Fujii, W. Meyer and G. Lieser, "Structure and properties of segmented polyether-esters. II. Crystallization behavior of polyether-esters with random distribution of hard segment length," Die Angewandte Makromolekulare Chemie: Applied Macromolecular Chemistry and Physics, vol. 74, p. 295–316, 1978.

[36] R. J. Gaymans and J. L. De Haan, "Segmented copolymers with poly (ester amide) units of uniform length: synthesis," Polymer, vol. 34, p. 4360–4364, 1993.

[37] G. J. E. Biemond, J. Feijen and R. J. Gaymans, "Tensile properties of segmented block copolymers with monodisperse hard segments," Journal of materials science, vol. 43, p. 3689–3696, 2008.

[38] J. Krijgsman, D. Husken and R. J. Gaymans, "Synthesis and properties of thermoplastic elastomers based on PTMO and tetra-amide," Polymer, vol. 44, p. 7573–7588, 2003.

[39] M. C. E. J. Niesten, J. Feijen and R. J. Gaymans, "Synthesis and properties of segmented copolymers having aramid units of uniform length," Polymer, vol. 41, p. 8487–8500, 2000.

[40] A. Arun and R. J. Gaymans, "Segmented Block Copolymers with Monodisperse Aramide End-Segments," Macromolecular chemistry and physics, vol. 209, p. 854–863, 2008.

[41] Y. Wang, P. Zhu, Y. Lai, L. Wang, D. Wang and X. Dong, "Effect of crosslinking networks on strain-induced crystallization in polyamide 1012 multiblock Poly (tetramethylene oxide) copolymers," Polymer, vol. 225, p. 123802, 2021.

[42] M. Nébouy, A. de Almeida, S. Brottet and G. P. Baeza, "Process-oriented structure tuning of PBT/PTHF thermoplastic elastomers," Macromolecules, vol. 51, p. 6291–6302, 2018.

[43] P. J. Flory, "Thermodynamics of high polymer solutions," The Journal of chemical physics, vol. 10, p. 51–61, 1942.

[44] M. L. Huggins, "Some properties of solutions of long-chain compounds.," The Journal of Physical Chemistry, vol. 46, p. 151–158, 1942.

[45] A. Arora, J. Qin, D. C. Morse, K. T. Delaney, G. H. Fredrickson, F. S. Bates and K. D. Dorfman, "Broadly accessible self-consistent field theory for block polymer materials discovery," Macromolecules, vol. 49, p. 4675–4690, 2016.

[46] R. K. W. Spencer and M. W. Matsen, "Domain bridging in thermoplastic elastomers of star block copolymer," Macromolecules, vol. 50, p. 1681–1687, 2017.

[47] C. Fernández-de-Alba, A. M. Jimenez, M. Abbasi, S. K. Kumar, K. Saalwächter and G. P. Baeza, "On the Immobilized Polymer Fraction in Attractive Nanocomposites: T g Gradient versus Interfacial Layer," Macromolecules, vol. 54, p. 10289–10299, 2021.

[48] O. Oguz, N. Candau, G. Stoclet, E. Simsek, C. Kosak Soz, E. Yilgor, I. Yilgor and Y. Z. Menceloglu, "Geometric Confinement Controls Stiffness, Strength, Extensibility, and Toughness in Poly (urethane–urea) Copolymers," Macromolecules, 2021.

[49] J. Zhang, R. Deubler, M. Hartlieb, L. Martin, J. Tanaka, E. Patyukova, P. D. Topham, F. H. Schacher and S. Perrier, "Evolution of microphase separation with variations of segments of sequence-controlled multiblock copolymers," Macromolecules, vol. 50, p. 7380–7387, 2017.

[50] S. Sbrescia, J. Ju, T. Engels, E. Van Ruymbeke and M. Seitz, "Morphological origins of temperature and rate dependent mechanical properties of model soft thermoplastic elastomers," Journal of Polymer Science, vol. 59, p. 477–493, 2021.

[51] S. Aime, N. D. Eisenmenger and T. A. P. Engels, "A model for failure in thermoplastic elastomers based on Eyring kinetics and network connectivity," Journal of Rheology, vol. 61, p. 1329–1342, 2017.

[52] H. Xie, H. Lu, Z. Zhang, X. Li, X. Yang and Y. Tu, "Effect of Block Number and Weight Fraction on the Structure and Properties of Poly (butylene terephthalate)-block-Poly (tetramethylene oxide) Multiblock Copolymers," Macromolecules, vol. 54, p. 2703–2710, 2021.

[53] M. Nébouy, L. Chazeau, J. Morthomas, C. Fusco, P. Dieudonné-George and G. P. Baeza, "Flow-induced crystallization of a multiblock copolymer under large amplitude oscillatory shear: Experiments and modeling," Journal of Rheology, vol. 65, p. 405–418, 2021.

[54] M. Nébouy, A. de Almeida, L. Chazeau and G. P. Baeza, "Modeling shear-induced crystallization in startup flow: The case of segmented copolymers," Journal of Rheology, vol. 63, p. 837–850, 2019.

[55] P. Ellis, The Future of Thermoplastic Elastomers to 2026, Smithers, 2021.

[56] A.-H. Lu, E. e. Salabas and F. Schüth, "Magnetic nanoparticles: synthesis, protection, functionalization, and application," Angewandte Chemie International Edition, vol. 46, p. 1222–1244, 2007.

[57] R. Gallu, F. Méchin, F. Dalmas, J.-F. Gérard, R. Perrin and F. Loup, "On the use of solubility parameters to investigate phase separation-morphology-mechanical behavior relationships of TPU," Polymer, vol. 207, p. 122882, 2020.

[58] D. Bae, M. J. Moon, M. Y. Shon, S. T. Oh, G. N. Kim and D. W. Yun, "Study on the heating behavior of Ni-embedded thermoplastic polyurethane adhesive film via induction heating," The Journal of Adhesion, vol. 93, p. 964–979, 2017.

[59] S. Salimi, T. S. Babra, G. S. Dines, S. W. Baskerville, W. Hayes and B. W. Greenland, "Composite polyurethane adhesives that debond-on-demand by hysteresis heating in an oscillating magnetic field," European Polymer Journal, vol. 121, p. 109264, 2019.

[60] H. Kishi, M. Kuwata, S. Matsuda, T. Asami and A. Murakami, "Damping properties of thermoplastic-elastomer interleaved carbon fiber-reinforced epoxy composites," Composites Science and technology, vol. 64, p. 2517–2523, 2004.

[61] H. Li and J. L. White, "Structure development in melt spinning filaments from polybutylene terephthalate based thermoplastic elastomers," Polymer Engineering & Science, vol. 40, p. 917–928, 2000.

[62] M. Viviani, S. P. Fluitman, K. Loos and G. Portale, "Proton conducting ABA triblock copolymers with sulfonated poly (phenylene sulfide sulfone) midblock obtained via copper-free thiol-click chemistry," Polymer Chemistry, vol. 12, p. 2563–2571, 2021.

[63] W. Huang, Q. Pan, H. Qi, X. Li, Y. Tu and C. Y. Li, "Poly (butylene terephthalate)-b-poly (ethylene oxide) alternating multiblock copolymers: synthesis and application in solid polymer electrolytes," Polymer, vol. 128, p. 188–199, 2017.

[64] E. A. Eastwood and M. D. Dadmun, "Multiblock copolymers in the compatibilization of polystyrene and poly (methyl methacrylate) blends: Role of polymer architecture," Macromolecules, vol. 35, p. 5069–5077, 2002.

[65] J. Zhou, X. Xu, Y. Xin and G. Lubineau, "Coaxial thermoplastic elastomer-wrapped carbon nanotube fibers for deformable and wearable strain sensors," Advanced Functional Materials, vol. 28, p. 1705591, 2018.

[66] H. Probst, K. Katzer, A. Nocke, R. Hickmann, M. Zimmermann and C. Cherif, "Melt Spinning of Highly Stretchable, Electrically Conductive Filament Yarns," Polymers, vol. 13, p. 590, 2021.

[67] "Thermoplastic Elastomers 101: An Ultimate Guide," [Online]. Available: https://omnexus.specialchem.com/selection-guide/thermoplastic-elastomer.

[68] J. Markarian, "Thermoplastic elastomer compounds continue upward trend," Plastics, Additives and Compounding, vol. 10, p. 38–43, 2008.

[69] Thermoplastic elastomers of KRAIBURG TPE comply with new VDI guideline 2017.

[70] J. M. D. Coey, Magnetostatics, Cambridge university press, 2010, p. 24–61.

[71] C. M. Sorensen, "Magnetism," in Nanoscale Materials in Chemistry, John Wiley & Sons, Ltd, 2002, pp. 169-221.

[72] A. P. Roberts, T. P. Almeida, N. S. Church, R. J. Harrison, D. Heslop, Y. Li, J. Li, A. R. Muxworthy, W. Williams and X. Zhao, "Resolving the Origin of Pseudo-Single Domain Magnetic Behavior," Journal of Geophysical Research: Solid Earth, vol. 122, pp. 9534-9558, 2017.

[73] T. Bayerl, M. Duhovic, P. Mitschang and D. Bhattacharyya, "The heating of polymer composites by electromagnetic induction–A review," Composites Part A: Applied Science and Manufacturing, vol. 57, p. 27–40, 2014.

[74] J. Degauque, "Magnétisme et matériaux magnétiques: introduction," Le Journal de Physique IV, vol. 2, p. C3–1, 1992.

[75] J. M. D. Coey, Introduction, Cambridge university press, 2010, p. 1–23.

[76] Z. Shaterabadi, G. Nabiyouni and M. Soleymani, "Physics responsible for heating efficiency and self-controlled temperature rise of magnetic nanoparticles in magnetic hyperthermia therapy," Progress in biophysics and molecular biology, vol. 133, p. 9–19, 2018.

[77] M. Anhalt and B. Weidenfeller, "Magnetic properties of polymer bonded soft magnetic particles for various filler fractions," Journal of applied physics, vol. 101, p. 023907, 2007.

[78] A. G. Kolhatkar, A. C. Jamison, D. Litvinov, R. C. Willson and T. R. Lee, "Tuning the magnetic properties of nanoparticles," International journal of molecular sciences, vol. 14, p. 15977–16009, 2013.

[79] J. M. D. Coey, Antiferromagnetism and other magnetic order, Cambridge university press, 2010, p. 195–230.

[80] J. M. D. Coey, Micromagnetism, domains and hysteresis, Cambridge university press, 2010, p. 231–263.

[81] M. Mehrmohammadi, K. Y. Yoon, M. Qu, K. P. Johnston and S. Y. Emelianov, "Enhanced pulsed magneto-motive ultrasound imaging using superparamagnetic nanoclusters," Nanotechnology, vol. 22, p. 045502, 2010.

[82] E. C. Abenojar, S. Wickramasinghe, J. Bas-Concepcion and A. C. S. Samia, "Structural effects on the magnetic hyperthermia properties of iron oxide nanoparticles," Progress in Natural Science: Materials International, vol. 26, p. 440–448, 2016.

[83] J. M. D. Coey, Nanoscale magnetism, Cambridge university press, 2010, p. 264–304.

[84] A. E. Deatsch and B. A. Evans, "Heating efficiency in magnetic nanoparticle hyperthermia," Journal of Magnetism and Magnetic Materials, vol. 354, p. 163–172, 2014.

[85] T. C. Monson, E. L. Venturini, V. Petkov, Y. Ren, J. M. Lavin and D. L. Huber, "Large enhancements of magnetic anisotropy in oxide-free iron nanoparticles," Journal of magnetism and magnetic materials, vol. 331, p. 156–161, 2013.

[86] X. Wang, H. Gu and Z. Yang, "The heating effect of magnetic fluids in an alternating magnetic field," Journal of magnetism and magnetic materials, vol. 293, p. 334–340, 2005.

[87] C. C. Corten and M. W. Urban, "Repairing polymers using oscillating magnetic field," Advanced materials, vol. 21, p. 5011–5015, 2009.

[88] C. L. Dennis and R. Ivkov, "Physics of heat generation using magnetic nanoparticles for hyperthermia," International Journal of Hyperthermia, vol. 29, p. 715–729, 2013.

[89] S. A. Rovers, R. Hoogenboom, M. F. Kemmere and J. T. F. Keurentjes, "Relaxation processes of superparamagnetic iron oxide nanoparticles in liquid and incorporated in poly (methyl methacrylate)," The Journal of Physical Chemistry C, vol. 112, p. 15643–15646, 2008.

[90] W. Wu, Z. Wu, T. Yu, C. Jiang and W.-S. Kim, "Recent progress on magnetic iron oxide nanoparticles: synthesis, surface functional strategies and biomedical applications," Science and technology of advanced materials, 2015.

[91] S. Tanwar, V. P. S. Awana, S. P. Singh and R. Pasricha, "Magnetic field dependence of blocking temperature in oleic acid functionalized iron oxide nanoparticles," Journal of superconductivity and novel magnetism, vol. 25, p. 2041–2045, 2012.

[92] J. M. D. Coey, Ferromagnetism and exchange, Cambridge university press, 2010, p. 128–194.

[93] D.-L. Hou, X.-F. Nie and H.-L. Luo, "Magnetic anisotropy and coercivity of ultrafine iron particles," Journal of magnetism and magnetic materials, vol. 188, p. 169–172, 1998.

[94] N. A. Usov, M. S. Nesmeyanov and V. P. Tarasov, "Magnetic vortices as efficient nano heaters in magnetic nanoparticle hyperthermia," Scientific reports, vol. 8, p. 1–9, 2018.

[95] J. M. D. Coey, Magnetic materials, Cambridge university press, 2010, p. 374–438.

[96] D. Serantes, D. Baldomir, C. Martinez-Boubeta, K. Simeonidis, M. Angelakeris, E. Natividad, M. Castro, A. Mediano, D.-X. Chen, A. Sanchez and others, "Influence of dipolar interactions on hyperthermia properties of ferromagnetic particles," Journal of Applied Physics, vol. 108, p. 073918, 2010.

[97] D. Caruntu, G. Caruntu and C. J. O'Connor, "Magnetic properties of variable-sized Fe3O4 nanoparticles synthesized from non-aqueous homogeneous solutions of polyols," Journal of physics D: Applied physics, vol. 40, p. 5801, 2007.

[98] T. Bayerl, R. Schledjewski and P. Mitschang, "Induction heating of thermoplastic materials by particulate heating promoters," Polymers and Polymer Composites, vol. 20, p. 333–342, 2012.

[99] D. Bae, P. Shin, S. Kwak, M. Moon, M. Shon, S. Oh and G. Kim, "Heating behavior of ferromagnetic Fe particle-embedded thermoplastic polyurethane adhesive film by induction heating," Journal of Industrial and Engineering Chemistry, vol. 30, p. 92–97, 2015.

[100] D. H. Bae, M. Y. Shon, S. T. Oh and G. N. Kim, "Study on the Heating Behavior of Fe3O4-Embedded Thermoplastic Polyurethane Adhesive Film via Induction heating," Bulletin of the Korean Chemical Society, vol. 37, p. 1211–1218, 2016.

[101] J. Carrey, B. Mehdaoui and M. Respaud, "Simple models for dynamic hysteresis loop calculations of magnetic single-domain nanoparticles: Application to magnetic hyperthermia optimization," Journal of Applied Physics, vol. 109, p. 083921, 2011.

[102] H. Nemala, J. S. Thakur, V. M. Naik, P. P. Vaishnava, G. Lawes and R. Naik, "Investigation of magnetic properties of Fe3O4 nanoparticles using temperature dependent magnetic hyperthermia in ferrofluids," Journal of Applied Physics, vol. 116, p. 034309, 2014.

[103] U. M. Engelmann, C. Shasha, E. Teeman, I. Slabu and K. M. Krishnan, "Predicting size-dependent heating efficiency of magnetic nanoparticles from experiment and stochastic Néel-Brown Langevin simulation," Journal of Magnetism and Magnetic Materials, vol. 471, p. 450–456, 2019.

[104] R. Hergt, S. Dutz, R. Müller and M. Zeisberger, "Magnetic particle hyperthermia: nanoparticle magnetism and materials development for cancer therapy," Journal of Physics: Condensed Matter, vol. 18, p. S2919, 2006.

[105] R. Ferrero, A. Manzin, G. Barrera, F. Celegato, M. Coïsson and P. Tiberto, "Influence of shape, size and magnetostatic interactions on the hyperthermia properties of permalloy nanostructures," Scientific reports, vol. 9, p. 1–12, 2019.

[106] P. H. Linh, P. V. Thach, N. A. Tuan, N. C. Thuan, D. H. Manh, N. X. Phuc and L. V. Hong, "Magnetic fluid based on Fe3O4 nanoparticles: Preparation and hyperthermia application," in J. Phys. Conf. Ser, 2009.

[107] A. Urtizberea, E. Natividad, A. Arizaga, M. Castro and A. Mediano, "Specific absorption rates and magnetic properties of ferrofluids with interaction effects at low concentrations," The Journal of Physical Chemistry C, vol. 114, p. 4916–4922, 2010.

[108] Y. Piñeiro-Redondo, M. Bañobre-López, I. Pardiñas-Blanco, G. Goya, M. A. López-Quintela and J. Rivas, "The influence of colloidal parameters on the specific power absorption of PAA-coated magnetite nanoparticles," Nanoscale research letters, vol. 6, p. 1–7, 2011.

[109] B. Mehdaoui, A. Meffre, L.-M. Lacroix, J. Carrey, S. Lachaize, M. Gougeon, M. Respaud and B. Chaudret, "Large specific absorption rates in the magnetic hyperthermia properties of metallic iron nanocubes," Journal of Magnetism and Magnetic Materials, vol. 322, p. L49–L52, 2010.

[110] R. Hiergeist, W. Andrä, N. Buske, R. Hergt, I. Hilger, U. Richter and W. Kaiser, "Application of magnetite ferrofluids for hyperthermia," Journal of Magnetism and Magnetic Materials, vol. 201, p. 420–422, 1999.

[111] C. W. Lai, F. W. Low, M. F. Tai and S. B. Abdul Hamid, "Iron oxide nanoparticles decorated oleic acid for high colloidal stability," Advances in Polymer Technology, vol. 37, p. 1712–1721, 2018.

[112] O. Moscoso-Londoño, P. Tancredi, D. Muraca, P. M. Zélis, D. Coral, M. F. van Raap, U. Wolff, V. Neu, C. Damm, C. L. P. De Oliveira and others, "Different approaches to analyze the dipolar interaction effects on diluted and concentrated granular superparamagnetic systems," Journal of Magnetism and Magnetic Materials, vol. 428, p. 105–118, 2017.

[113] W. D. Woolley, "Nitrogen-containing products from the thermal decomposition of flexible polyurethane foams," British Polymer Journal, vol. 4, p. 27–43, 1972.

[114] G. P. Baeza, A.-C. Genix, C. Degrandcourt, L. Petitjean, J. Gummel, M. Couty and J. Oberdisse, "Multiscale filler structure in simplified industrial nanocomposite silica/SBR systems studied by SAXS and TEM," Macromolecules, vol. 46, p. 317–329, 2013.

[115] Y. Mosleh, N. G. Ebrahimi, A. Mahdavian and M. Ashjari, "TPU/PCL/nanomagnetite ternary shape memory composites: studies on their thermal, dynamic-mechanical, rheological and electrical properties," Iranian Polymer Journal, vol. 23, p. 137–145, 2014.

[116] Y. Yang, J. He, Q. Li, L. Gao, J. Hu, R. Zeng, J. Qin, S. X. Wang and Q. Wang, "Self-healing of electrical damage in polymers using superparamagnetic nanoparticles," Nature nanotechnology, vol. 14, p. 151–155, 2019.

[117] Y. Yang, L. Gao, J. Xie, Y. Zhou, J. Hu, Q. Li and J. He, "Defect-targeted self-healing of multiscale damage in polymers," Nanoscale, vol. 12, p. 3605–3613, 2020.

[118] D. Nichetti, S. Cossar and N. Grizzuti, "Effects of molecular weight and chemical structure on phase transition of thermoplastic polyurethanes," Journal of Rheology, vol. 49, p. 1361–1376, 2005.

[119] A. S. Ahmed and R. V. Ramanujan, "Curie temperature controlled self-healing magnet–polymer composites," Journal of Materials Research, vol. 30, p. 946–958, 2015.

[120] M. Schrödner and G. Pflug, "Magnetomechanical properties of composites and fibers made from thermoplastic elastomers (TPE) and carbonyl iron powder (CIP)," Journal of Magnetism and Magnetic Materials, vol. 454, p. 258–263, 2018.

[121] G. D. Soto, C. Meiorin, D. G. Actis, P. M. Zélis, O. M. Londoño, D. Muraca, M. A. Mosiewicki and N. E. Marcovich, "Magnetic nanocomposites based on shape memory polyurethanes," European Polymer Journal, vol. 109, p. 8–15, 2018.

[122] Y. Kim, H. Yuk, R. Zhao, S. A. Chester and X. Zhao, "Printing ferromagnetic domains for untethered fast-transforming soft materials," Nature, vol. 558, p. 274–279, 2018.

[123] N. Hohlbein, A. Shaaban and A. M. Schmidt, "Remote-controlled activation of self-healing behavior in magneto-responsive ionomeric composites," Polymer, vol. 69, p. 301–309, 2015.

[124] Y. Chen, X. Zhao, Y. Li, Z.-Y. Jin, Y. Yang, M.-B. Yang and B. Yin, "Light-and magnetic-responsive synergy controlled reconfiguration of polymer nanocomposites with shape memory assisted self-healing performance for soft robotics," Journal of Materials Chemistry C, 2021.

[125] P. Cordier, F. Tournilhac, C. Soulié-Ziakovic and L. Leibler, "Self-healing and thermoreversible rubber from supramolecular assembly," Nature, vol. 451, p. 977–980, 2008.

[126] E. Ogliani, L. Yu, I. Javakhishvili and A. L. Skov, "A thermo-reversible silicone elastomer with remotely controlled self-healing," RSC advances, vol. 8, p. 8285–8291, 2018.

[127] G. Falco, P. Griffiths, C. Coutouly, C.-A. Fustin and G. P. Baeza, "Supramolecular Superparamagnetic Nanocomposites Based on a Magnetite-Filled Unentangled Terpyridine-Functionalized Polymer," Macromolecules, vol. 53, p. 5361–5370, 2020.

[128] K. Van de Velde and P. Kiekens, "Thermoplastic polymers: overview of several properties and their consequences in flax fibre reinforced composites," Polymer testing, vol. 20, p. 885–893, 2001.

[129] G. Jogur, A. Nawaz Khan, A. Das, P. Mahajan and R. Alagirusamy, "Impact properties of thermoplastic composites," Textile Progress, vol. 50, p. 109–183, 2018.

[130] Z. Xiang, B. Ducharne, N. Della Schiava, J.-F. Capsal, P.-J. Cottinet, G. Coativy, P. Lermusiaux and M. Q. Le, "Induction heating-based low-frequency alternating magnetic field: High potential of ferromagnetic composites for medical applications," Materials & Design, vol. 174, p. 107804, 2019.

[131] H.-Y. Mi, Z. Li, L.-S. Turng, Y. Sun and S. Gong, "Silver nanowire/thermoplastic polyurethane elastomer nanocomposites: Thermal, mechanical, and dielectric properties," Materials & Design (1980-2015), vol. 56, p. 398–404, 2014.

[132] A. P. Khandhar, R. M. Ferguson, J. A. Simon and K. M. Krishnan, "Tailored magnetic nanoparticles for optimizing magnetic fluid hyperthermia," Journal of Biomedical Materials Research Part A, vol. 100, p. 728–737, 2012.

[133] T. C. Han, M. R. Tsai and C. Y. Wei, "Size effect on magnetic properties of hexagonal HoMnO3 nanoparticles," Journal of Applied Physics, vol. 109, p. 07B517, 2011.

[134] R. Müller, S. Dutz, A. Neeb, A. C. B. Cato and M. Zeisberger, "Magnetic heating effect of nanoparticles with different sizes and size distributions," Journal of Magnetism and Magnetic Materials, vol. 328, p. 80–85, 2013.

[135] P. Guardia, A. Labarta and X. Batlle, "Tuning the size, the shape, and the magnetic properties of iron oxide nanoparticles," The Journal of Physical Chemistry C, vol. 115, p. 390–396, 2011.

[136] C. de Montferrand, L. Hu, I. Milosevic, V. Russier, D. Bonnin, L. Motte, A. Brioude and Y. Lalatonne, "Iron oxide nanoparticles with sizes, shapes and compositions resulting in different magnetization signatures as potential labels for multiparametric detection," Acta biomaterialia, vol. 9, p. 6150–6157, 2013.

[137] G. Zhen, B. W. Muir, B. A. Moffat, P. Harbour, K. S. Murray, B. Moubaraki, K. Suzuki, I. Madsen, N. Agron-Olshina, L. Waddington and others, "Comparative study of the magnetic behavior of spherical and cubic superparamagnetic iron oxide nanoparticles," The Journal of Physical Chemistry C, vol. 115, p. 327–334, 2011.

[138] S. L. Saville, B. Qi, J. Baker, R. Stone, R. E. Camley, K. L. Livesey, L. Ye, T. M. Crawford and O. T. Mefford, "The formation of linear aggregates in magnetic hyperthermia: Implications on specific absorption rate and magnetic anisotropy," Journal of colloid and interface science, vol. 424, p. 141–151, 2014.

[139] D. Serantes, K. Simeonidis, M. Angelakeris, O. Chubykalo-Fesenko, M. Marciello, M. D. P. Morales, D. Baldomir and C. Martinez-Boubeta, "Multiplying magnetic hyperthermia response by nanoparticle assembling," The Journal of Physical Chemistry C, vol. 118, p. 5927–5934, 2014.

[140] O. Yassine, A. Zaher, E. Q. Li, A. Alfadhel, J. E. Perez, M. Kavaldzhiev, M. F. Contreras, S. T. Thoroddsen, N. M. Khashab and J. Kosel, "Highly efficient thermoresponsive nanocomposite for controlled release applications," Scientific reports, vol. 6, p. 1–7, 2016.

Chapter II: Materials & Methods

Contents

1 Raw materials

1.1 TPU matrix

The polymer matrix used in this work consists of a commercial TPU, Desmopan 85085A supplied by Covestro (Germany). The TPU comes in the shape of plastic pellets, intended for processing through extrusion or injection moulding (see Figure 2.1A). As explained in Chapter I section 1.1, a TPU is made of a succession of hard-segment (HS) that can phase separate and possibly crystallize at room temperature encompassed into a soft-segments (SS) amorphous rubbery background. As seen in Figure 2.1B, HS are formed by the association of hexane-1,6-diol (HDO) and hexamethylene diisocyanate (HDI) as chain extender. SS are made of a mixture of butanediol polyadipate PABD (M_n ~ 1350 g/mol) and polypropylene oxide PPO (M_n ~ 1000 g/mol). Flory statistics theoretically indicates a polymolecularity index equal to 2, meaning that at higher lengthscales, the whole TPU chains are polydisperse because of their synthesis through polycondensation.

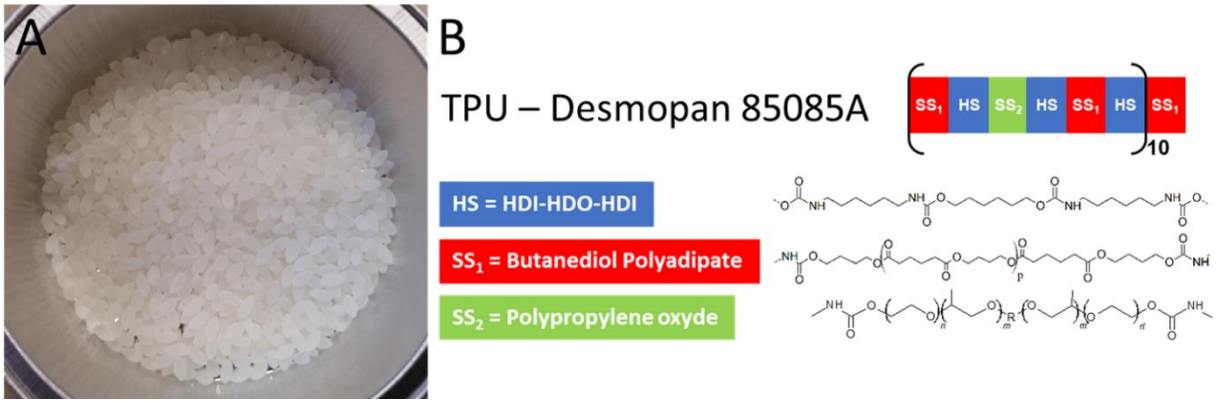

Figure 2.1: Desmopan 85085A. (A) Pellets for the production of TPU-based magnetic composites. Pellets are white because of the HS/SS phase separation and crystallization of HS. (B) Schematic representation of the TPU architecture and corresponding chemical formulae for each segment.

1.2 Magnetic particles

The three different magnetic powders, purchased from Nanografi (Turkey), are chosen as fillers to reinforce and prepare responsive rubber composites (see Figure 2.2). For simplicity, the three sets of particles will be referred to as Fe_3O_4, Fe-n and Fe-µ. The heating mechanisms expected for each set of particles will be detailed in Chapter II section 2.4. The densities used for Fe_3O_4 and Fe composites are 5.17 and 7.87 g cm^{-3} respectively. Their characteristics are as follows:

- Fe_3O_4 nanoparticles (99.55%) consist on building block particles of 14 - 29 nm in diameter forming "fractal aggregates" of *ca.* 100 nm in radius (see Figure 2.2B). Since the superparamagnetic blocking diameter is $D_{sp}^{Fe_3O_4}$ is 26 nm at room temperature, these particles are mainly superparamagnetic (see Chapter I sections 2.3 and 2.4).
- Fe-n nanoparticles (99.55%) consist on spherical particles with a diameter of 90 – 100 nm (see Figure 2.2C). In spite of their nanometric size, these particles are bigger than the iron maximum single domain size (*i.e.*, 20 nm), and therefore, they are expected to be multi-domain making their spin structure more complex than in the case of Fe_3O_4 powder. These particles are expected to mainly heat through magnetic walls motion (see Chapter I section 2.4).
- Fe-µ particles (99.99%) have been sieved with a 325 mesh (≈ 44 µm), and contain a wide distribution of particle sizes and shapes (see Figure 2.2D). While most of the particles have a *ca.* 50 µm diameter, some of them are larger, mainly below 200 µm. Furthermore, it appears that there is a non-negligible number of needle-shaped nanoparticles of typically 300 nm long and 50 nm wide. These particles are not visible in the SEM images of the as-received powder, it is possible that they come from the breaking of agglomerates (see Figure 2.2E) during composite processing (see Chapter II section 2). The polydispersity in this powder is thus important to keep in mind for further interpretations.

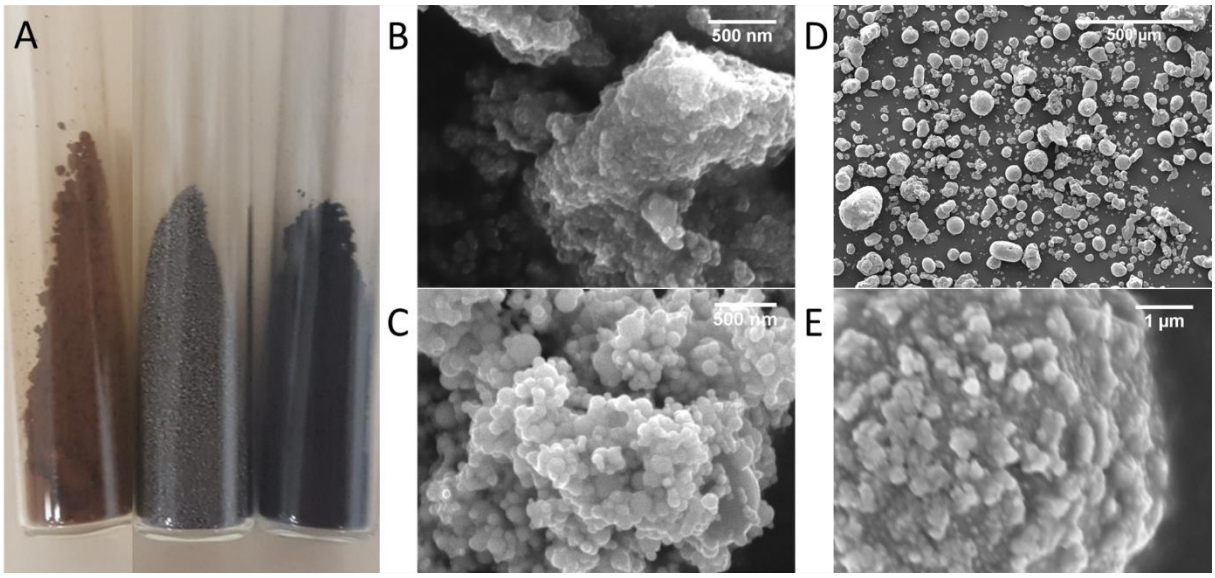

Figure 2.2: (A) Nanografi Fe_3O_4, Fe-n and Fe-µ magnetic particles (from left to right respectively). SEM micrographs of (B) Fe_3O_4, (C) Fe-n and (D-E) Fe-µ powders.

X-Ray Diffraction measurements were performed on the as-received magnetic powders to confirm their nature (see Figure 2.3). Diffractograms show that all the peaks correspond crystallographic plane families as described by the Miller indices (hkl) of magnetite Fe_3O_4 and iron Fe respectively, confirming the purity of the magnetic particles.

Fourier-transform infrared spectroscopy (FTIR) experiments performed in attenuated total reflectance mode on Fe_3O_4, Fe-n and Fe-µ powders are presented in Figure 2.4. Typical Fe-O and O-H bands are visible in Fe_3O_4 corresponding to the surface state made of Fe-O-Fe bridges and Fe-OH groups (see Figure 2.4A). In contrast, O-H bands are not noted in Fe particles (see Figure 2.4B). Interestingly, while Fe-µ does not exhibit any strong band, synonymous of a high purity, whereas Fe-n does reveal the presence of Fe-O groups likely to interact with the HS of the TPE.

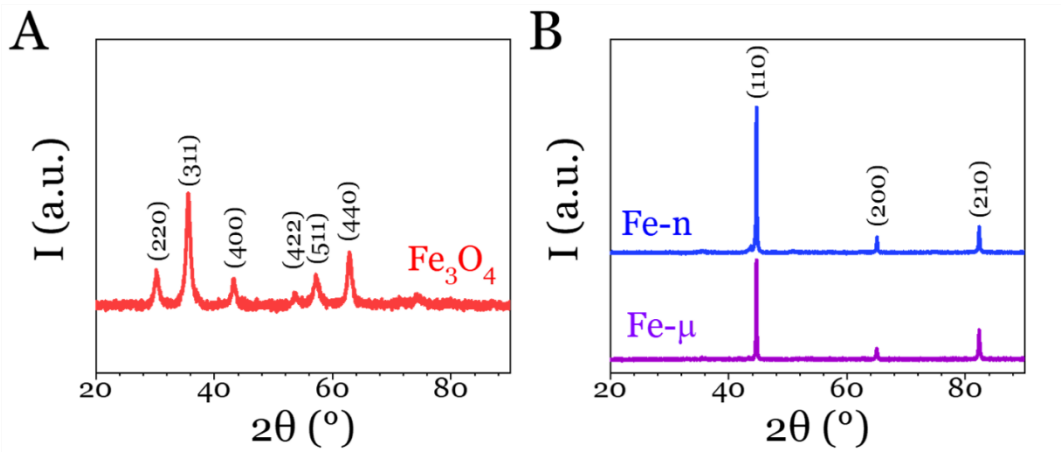

Figure 2.3: XRD patterns for (A) Fe_3O_4, (B) Fe-n and Fe-µ as-received powders.

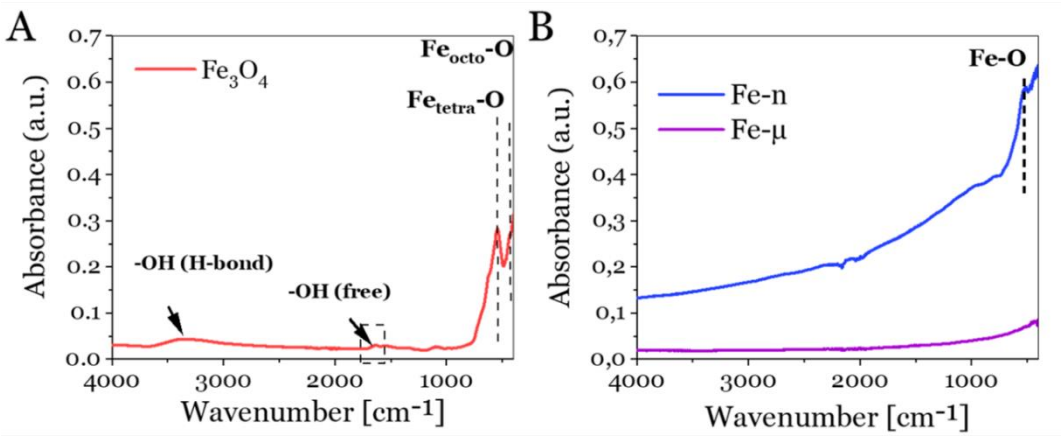

Figure 2.4: FTIR spectra of (A) Fe_3O_4, (B) Fe-n and Fe-µ as-received magnetic powders.

2 Formulation and processing of the composites

The composites are processed through twin-screw extrusion followed by hot-pressing. An appropriate amount of Desmopan (12 g) and magnetic particles (from *ca.* 1 to 15 g) are first hand-mixed at room temperature. The corresponding composites with increase filler fraction are referred to as 1, 5, 10 and 15 vol.%. The exact filler content for each composite sample has been determined by thermogravimetric analysis and can be found in Chapter III section 2.1.

This mixture is then poured into a DSM Xplore (Netherlands) mini-extruder (see Figure 2.5A) having a chamber of 15 cm^3, equipped with two vertical co-rotative screws in a stepwise manner and a canal creating a recirculation loop for the extruded material. The extruder chamber is pre-heated at 175°C ensuring the quick melting of the TPU. The extruder's rotor speed is set to 80 rpm and the mixing time to 5 min once the whole sample is poured into the extruder. After this time, the couple exhibits a minimum and remains constant. The extruded composite is collected on a Teflon composite sheet.

The raw composites are then hot-pressed at 180°C for 3 min under 10 MPa and subsequently cooled down in air down to room temperature in *ca.* 10 min with no external pressure. The composites are shaped into films of either 65 x 65 x 1 mm^3 or 40 x 40 x 0.5 mm^3 depending on the type of characterization for which they are intended. Aluminum plates and 0.1 mm-thick Teflon sheets are used for molding the composite films (see Figure 2.5B). For tensile and healing experiments, thicker composite films (*i.e.*, 1 mm) are required, while the thinner films (*i.e.*, 0.5 mm) are used for other characterizations, such as dielectric spectroscopy, atomic force microscopy, electron microscopy, rheology, magnetic characterizations and induction heating. Hot-pressed films are then kept in sealed plastic bags at room temperature.

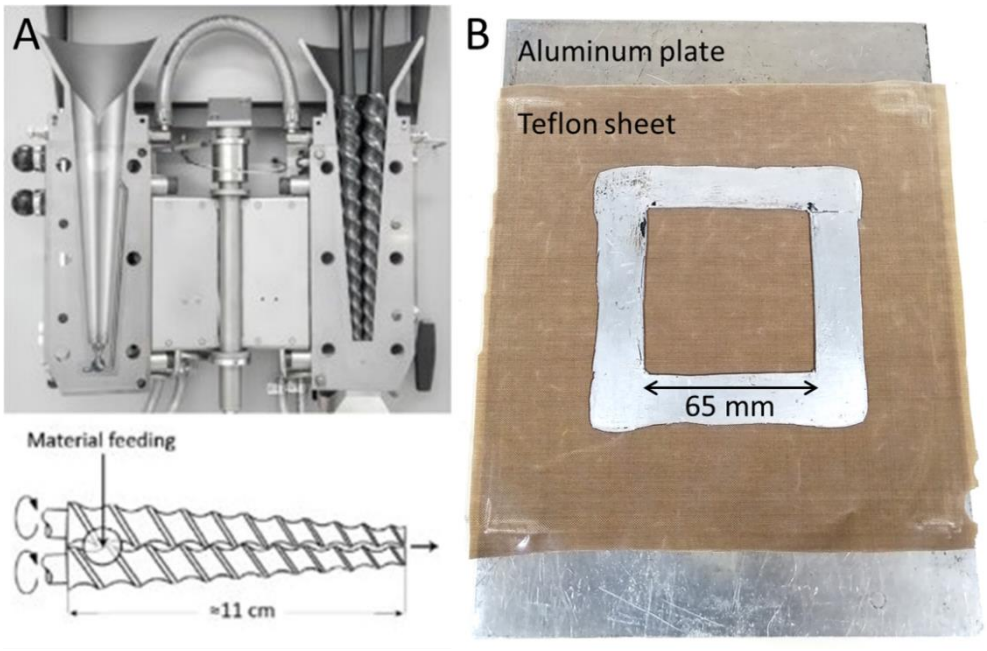

Figure 2.5: (A) DSM Xplore mini-extruder and its schematic representation. [1] (B) Arrangement for hot-pressing.

3 Physical characterization of materials

3.1 Atomic force microscopy

Atomic force microscopy (AFM) is a microscopy technique using the interaction between the atoms at the tip (connected to a cantilever) and the surface. The interaction leads to a contrast in rigidity or topography with the tip scanning the selected surface one line at a time. The probing device (cantilever and tip) relies on piezoelectric components allowing for a precise control of the device (see Figure 2.6), with a signal feedback loop controlling its reaction movement. Small changes in the topography or rigidity of the surface are detected with a laser being reflected on the top surface of the cantilever. This is particularly interesting for polymer materials, for which electron microscopy would not display any contrast. A high-quality tip, carefully tuned to its resonating frequency, can lead to a resolution down to the atomic level. This technique is limited by the quality of the sample's surface and its scanning rate is relatively slow compared to other microscopy techniques.

AFM phase micrographs are performed on a Dimension 3100 equipped with a Nanoscope V scanning probe controller (Bruker, USA) using tapping mode. All experiments are performed

in air and at room temperature using noncontact PointProbe® Plus Non-Contact / tapping mode – High resonance frequency (PPP-NCH) tips with resonating frequencies around 330 kHz, a radius of curvature smaller than 7 nm, and a nominal spring constant of 42 N m^{-1} (Nanosensor, Switzerland). Raw samples, processed through hot-pressing, are used for AFM analysis.

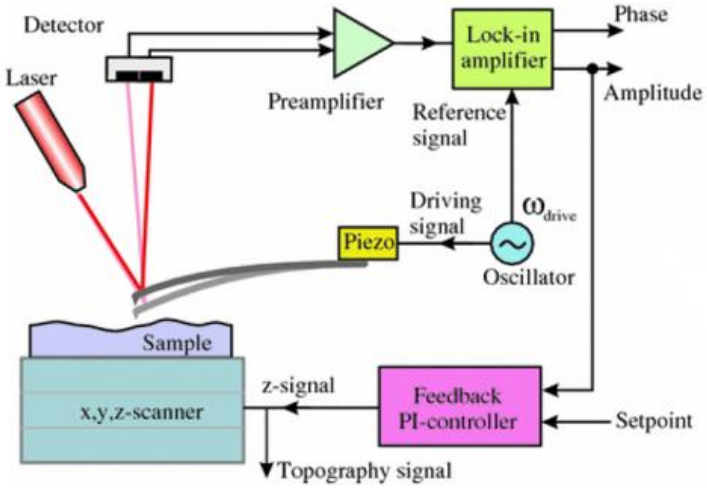

Figure 2.6: Schematic representation of an AFM feedback loop, controlling the movement and detecting the oscillation amplitude of the cantilever over the surface of the sample. [2]

3.2 Electron microscopy

Electron microscopy is based on the interaction between an electron beam and the sample, although in most cases, it requires an induced vacuum to work. Depending on the accelerating voltage used, it can access resolutions down to 0.2 nm for the best instruments (high resolution transmission electron microscopes). The reliance of these techniques on the interaction between electrons and the material (see Figure 2.7) can lead to material damage depending on the intensity of the beam and the exposure time. Polymers are particularly sensitive to the electron beam. Analyzed samples need to be conductive or have a metal coating to avoid overcharging the surface.

Scanning electron microscopy (SEM) produces images through the scanning of the surface with an electron beam. Among all the electrons generated by the interactions between the incident beam and the sample, secondary electrons SE are useful for the topography and backscattered electrons BSE are used for the chemical contrast. The interaction with the material leads to the emission of secondary electrons, which are detected and generate the SEM

image. The large field depth can generate images representing the surface. Coating with a thin layer of metal might be needed for some samples (non-conductive specimens), to prevent problems generated by the accumulation of electron charges. Samples intended for SEM have been metallized with platinum. SEM images of magnetic powders and composite micrographs are obtained using a VEGA3 (TESCAN, USA). The acceleration tension of the electrons is set to 10 - 20 kV, and the beam intensity varied from 3 to 13.

Transmission electron microscopy (TEM) is a different technique in which a thin specimen is irradiated and the electrons are collected after passing through the sample. Depending on the composition of the sample, these electrons are scattered, absorbed or transmitted. The TEM image is the print of all the interactions and displays a contrast in atomic number, making it a technique adapted to materials composed by inorganic particle and an organic matrix. The field depth is small, and a single image might not be representative of the whole sample. A sample in the shape of thin film is crucial to ensure a good signal to noise ratio. The specimens analyzed are prepared by cryo-ultramicrotomy using a Ultracut UCT microtome (Leica, Germany) with a diamond knife (DiAtome, United Kingdom). The temperature of the sample and the cutting speed are set to -80°C (below the glass transition of the soft phase) and 0.3 mm s^{-1} respectively. Sections of about 90 nm thick are dry-collected and placed on a 400-mesh copper grid. TEM images are acquired using a CM120 Philips transmission electron microscope operating at an accelerating voltage of 120 kV. Precise scans of various regions of the sample are systematically collected, starting from a small magnification and then gradually increased.

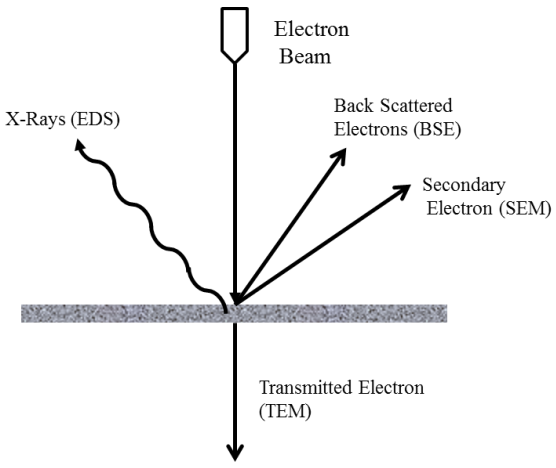

Figure 2.7: Illustration of the different interactions of an electron beam with the sample.

3.3 X-ray diffraction

X-ray diffraction (XRD) relies on the interaction between X-rays and a specimen. The resulting diffractogram displays the intensity of diffracted X-ray over 2θ (*i.e.*, the angle between the incident beam and the diffracted X-rays). As the wavelength of the X-ray beam is known, diffracted X-rays are detected displaying peaks at characteristic angles, following Bragg's equation. Every crystal structure generates a distinctive X-ray diffractogram with peaks at specific angles, and thus this analysis leads to the identification of the nature and crystal structure of the specimen. If the sample consists of different components (*e.g.*, particles having an oxidized layer), both characteristic patterns appear in the diffractogram.

XRD measurements are performed at room temperature on a D8 advance apparatus (Bruker, USA) using Cu-Kα1 radiation wavelength of 1.54 Å. The diffraction pattern of our Fe_3O_4 powder was recorded in the 2θ range of 15 – 90°, whereas that of Fe-n and Fe-μ was recorded in the range of 20 – 120°.

3.4 Small-angle X-ray scattering

Small-angle X-ray scattering (SAXS) is a technique relying on the detection of scattered electrons from the sample at small angles θ (*i.e.*, 0.1 to 10°), which are linked to the scattering vector q through the following equation:

$$|q| = \frac{4\pi}{\lambda} \sin\frac{\theta}{2} \qquad \text{(II-1)}$$

This measurement at the nanoscale is used to determine the size and shape of particles in a composite or of various phases in the case of bi-phasic specimens. It generates an average of the electron interactions over a relatively large section of the sample, in the order of 10^4 – 10^5 μm^2 (see Figure 2.8). Intensity $I(q)$ is determined using the following equation:

$$I(q) = I_0 P(q) S(q) \qquad \text{(II-2)}$$

where I_0, $P(q)$ and $S(q)$ are the intensity at origin, the form factor and the structure factor respectively. The form factor characterizes the distribution of the object's mass in the space, while the structure factor is given by the spatial correlation between such objects.

SAXS experiments are carried out on a Xeuss 2.0 apparatus (Xenocs, FR) at the Laboratoire Léon Brillouin (LLB, CEA Saclay, France). The instrument uses a microfocused Cu-Kα1 source with a wavelength of 1.54 Å and a Pilatus3 detector (Dectris, Switzerland). Samples are shaped into 1 mm thick films and the sample-detector distance was set to 2.5 m to achieve a q-range from 0.03 - 2 nm^{-1}. Data is corrected from the background, transmission and thickness sample to obtain the scattering intensity in absolute units (cm^{-1}).

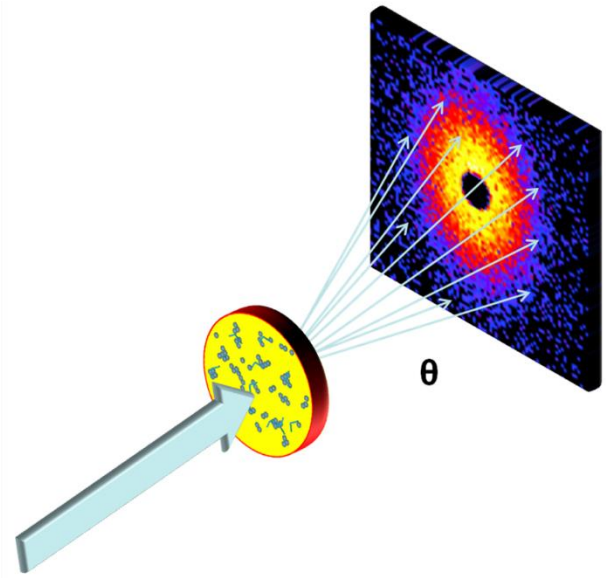

Figure 2.8: Schematic representation of the pattern resulting from a SAXS experiment.

3.5 Differential scanning calorimetry

Differential scanning calorimetry (DSC) is a thermal analysis technique in which the heat flow difference between a specimen and a reference is measured as a function of the temperature. Both the sample and the reference follow the same temperature cycle, which can consist of several heating and/or cooling steps. This is the predominant technique for determining phase-transition temperatures such as the glass transition T_g, the melting point T_m and the crystallization point T_c. Chemical properties, such as oxidation, stability, degradation and kinetics of crystallization can also be studied. It can also indicate the specific heat capacity C_p

of the specimen, with the heat flow baseline divided by the heating rate used for the measurement.

Controlling the atmosphere and the temperature during testing is crucial. Usually, an inert gas, such as nitrogen, helium or argon is used to prevent an undesired interaction with the sample and to regulate the temperature.

Samples of 10 to 20 mg are tested using a Perkin Elmer DSC 8000 (see Figure 2.9) by cooling down to -90°C and then heating up to 220°C with a rate of 10°C min^{-1}. This cycle is then repeated, resulting in a total of two cycles for each formulation. The cooling is ensured with a nitrogen flow of 20 mL min^{-1} at -120°C.

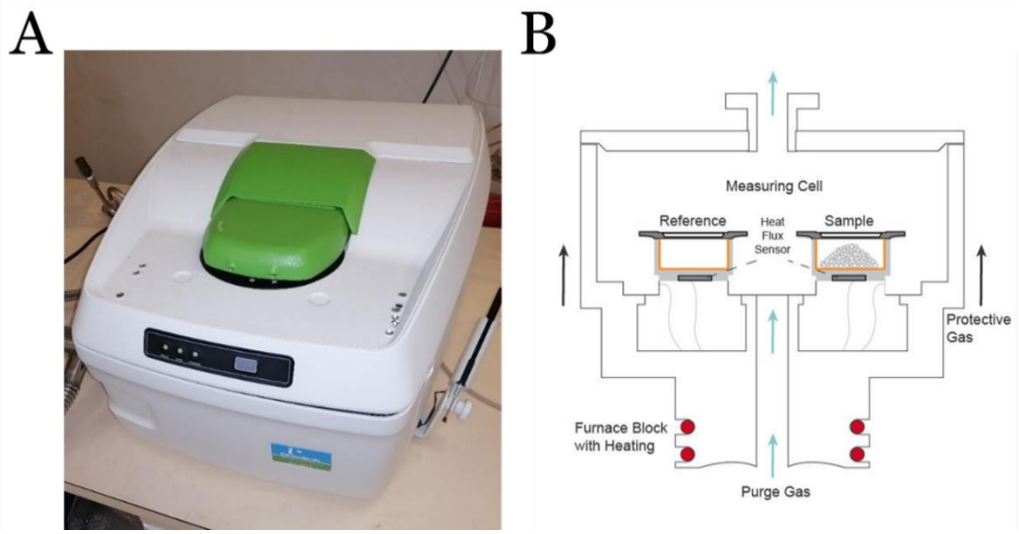

Figure 2.9: (A) Perkin Elmer DSC 8000 and (B) schematic representation of the workings of a DSC. [3]

3.6 Rheology

Rheology is the study of the flow and deformation of matter under an applied stress. It is mostly used to measure characteristic mechanical properties of soft materials. In the case of a rotational rheometer, the deformation of the material comes from the rotation of plates over and/or under the sample through steady shear of oscillatory shear. The most common types of rheology experiments are stress relaxation, creep recovery and dynamical frequency sweeps.

We performed dynamic frequency sweep measurements ($100 > \omega > 0.1$ rad s^{-1} and $\gamma = 10 –$ 50 % according to the materials) in a strain-controlled rheometer (ARES 2KFRTN1 from Rheometric Scientific, currently TA, USA) using stainless steel parallel plates of 8 mm

diameter (*ca.* 0.8 mm in sample thickness). A nitrogen convection oven allowed maintaining an inert atmosphere with a temperature control in the order of ±1°C. Measuring the storage and loss shear moduli (components of the complex shear modulus) over time or temperature will give indications for the state of the matter and the characteristic phase-transition times or temperatures. The storage modulus G' and the loss modulus G'' represent the elastic and viscous contributions of the viscoelastic behavior respectively.

It is worth noting that many different measuring geometries can be used such as, plate-plate, cone-plate, concentric cylinders (see Figure 2.10) according to the properties of the measured sample. For example, larger plates will be used to measure samples of lower viscosity to ensure a good signal/noise ratio and to limit the deformation of the tool. Parallel plate is the most common geometry for linear (low deformation) measurements.

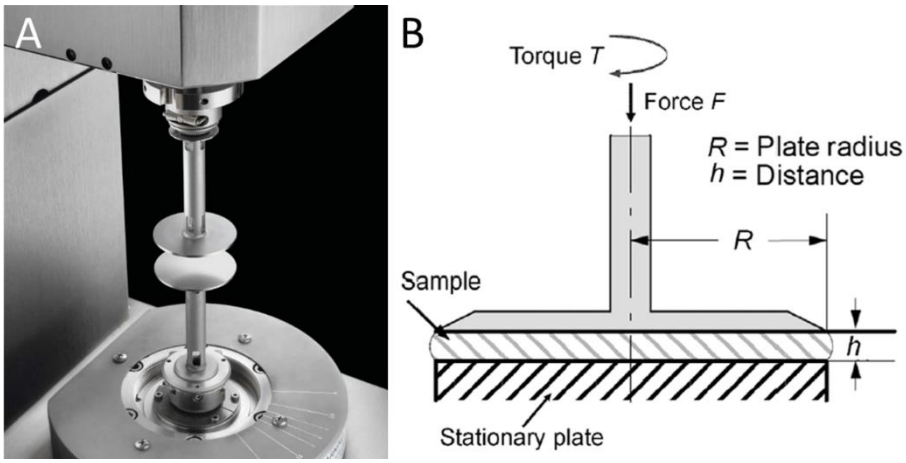

Figure 2.10: (A) Plate-plate measuring geometry. (B) Schematic representation of the plate-plate geometry. [4]

3.7 Superconducting quantum interference device

The superconducting quantum interference device (SQUID) has the purpose of characterizing the magnetic behavior of a material by following its magnetization in a temperature-controlled cell under an applied magnetic field H delivered by either an alternating current AC or by a direct current DC. Small samples (*i.e.*, 2 x 2 x 0.5 mm^2) intended for magnetic characterization are placed inside a transparent plastic straw and attached with a thread on both ends to suspend the sample at the center of the straw (see Figure 2.11A-B). We performed two types of tests using the SQUID magnetometer: magnetization-demagnetization and zero field cooling - field cooling.

Magnetization-demagnetization curves are obtained by following the induced magnetization on the material subjected to a set of magnetic solicitations. Different types of magnetic behavior have been described in Chapter I section 2.2. This test is performed with a quasi-static frequency (*i.e.*, f = 0.5 Hz) varying magnetic solicitations, at 300 K. First, a magnetic field with an amplitude of +4000 kA m^{-1} is applied to the specimen. Then, the measurements of the magnetic moment are performed while the amplitude of the solicitation decreases down to -4000 kA m^{-1} and increases back to +4000 kA m^{-1} to complete the cycle.

The zero-field cooling - field cooling (ZFC-FC) allows for a clear distinction between superparamagnetic and ferro/ferrimagnetic behavior of a material. The tested material is cooled down to a near-zero Kelvin temperature (*i.e.*, 6 K) in the absence of an external magnetic field. Then the material is subjected to a magnetic field amplitude H (*i.e.*, 4 kA m^{-1}) with a quasi-static frequency (*i.e.*, 0.5 Hz) and heated up to 300 K. The measurement of the magnetic moment while increasing the temperature is called the ZFC curve. While maintaining the same magnetic field amplitude, the temperature is decreased again to a near-zero Kelvin temperature. The measurement of the magnetic moment while decreasing the temperature is called the FC curve.

The fact that the ZFC and FC curves do not overlap is a clear indication of superparamagnetism (see Figure 2.11C). For the ZFC measurement of a superparamagnetic material, once the material has been taken to a near-zero temperature, it can be considered as blocked. Raising the temperature near T_B will take the particle out of its blocked state, and increase the magnetization. The thermal energy activates the superparamagnetic behavior above T_B.

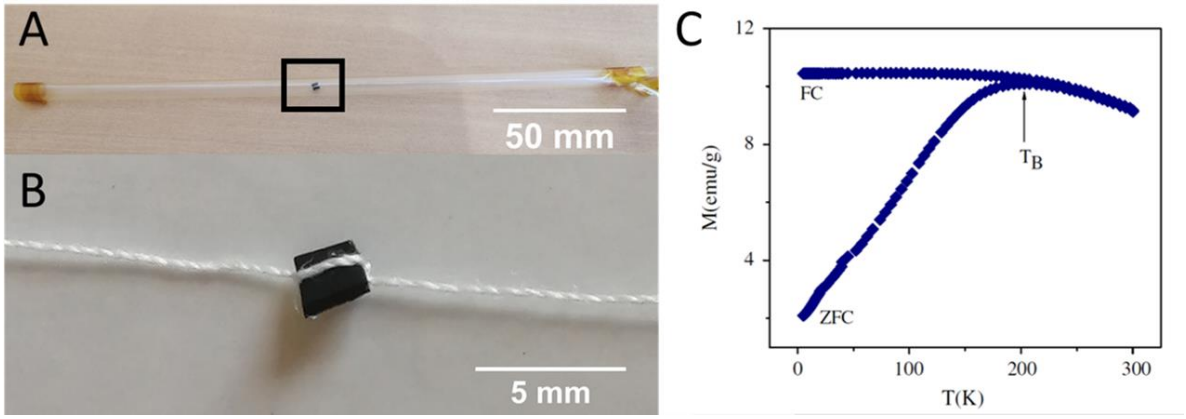

Figure 2.11: (A) Set-up for holding the sample inside the SQUID. (B) Zoom in on the sample attached with a thread. (C) Typical ZFC-FC curve for a superparamagnetic specimen. Curve extracted from Caruntu et al., [5] for oleate-capped magnetite nanocrystals with 6 mm in diameter.

3.8 Tensile test

Uniaxial tensile tests allow for the determination of the constitutive law in a uniaxial traction. These tests have been performed on the magnetic composite samples at room temperature on a 1/ME device (MTS, USA) equipped with a 1 kN load cell (see Figure 2.12). Samples are punched using the appropriate H3 dice with 20 mm gage length and 4 mm wide and are shaped into dumbbell pieces of working dimensions 10.0 × 4.0 × 1.0 mm^3. They are held and tightened using jaws, with the sample placed vertically. We used small pieces of rubber to enhance the grip of the jaws for the neat matrix and the composites with the least amount of magnetic filler (*i.e.*, 1 and 5 vol.% of Fe_3O_4, Fe-n and Fe-µ composites).

The vertical displacement rate is set to 10 $mm.min^{-1}$, and force and displacement are recorded during the test. The corresponding true strain ε_t and true stress σ_t are then calculated using the dimensions of the sample and assuming the absence of volume variation during the whole deformation. The Young's modulus is calculated using the initial linear slope of the true stress over true strain curve. A minimum of three samples are measured for each formulation.

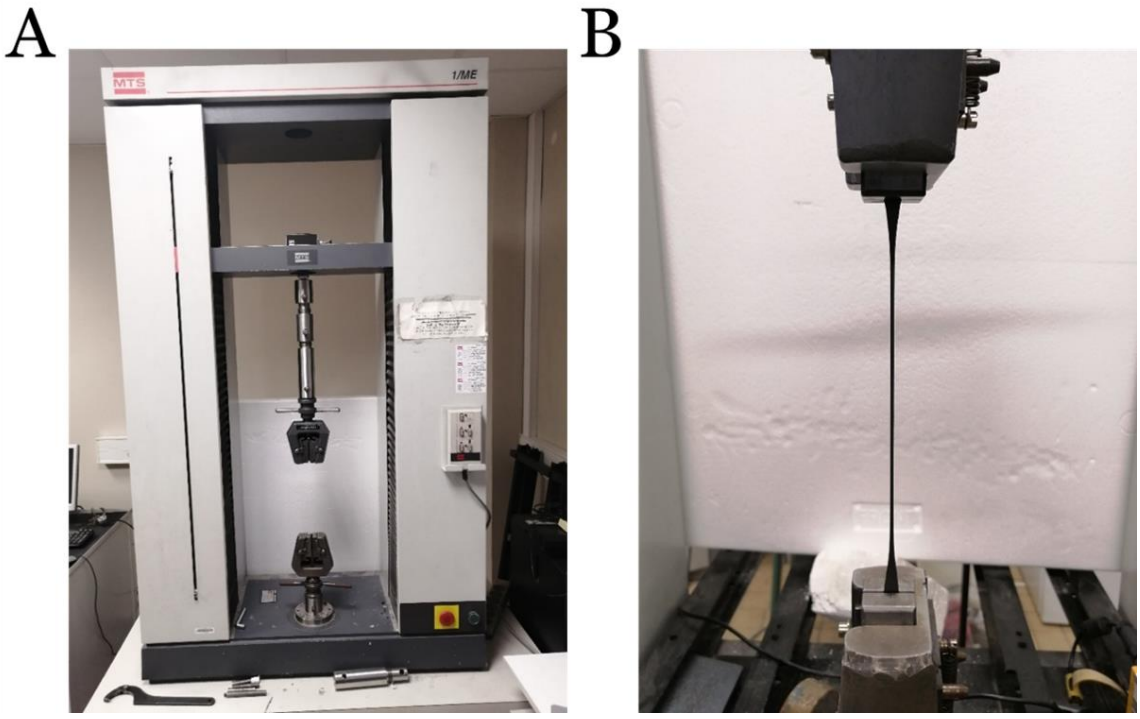

Figure 2.12: (A) MTS 1/ME and (B) a sample being tested for uniaxial deformation tensile test.

3.9 X-ray tomography

X-ray tomography enables the acquirement of a 3D volume of the sample though the interaction with an X-ray beam. These measurements are performed on a GE Sensing & Inspection Technologies Phoenix v|tome|x (USA) with a PaxScan digital X-ray image detector (Varian, USA) at room temperature (*ca.* 25°C).

The 3D reconstruction of the whole sample is possible by rotating and/or moving it vertically (see Figure 2.13), while continuously recording radiographs. The collected 2D images are gathered and stacked to recreate the 3D sample using Phoenix datos|x software. Display and adjustments of the reconstructed volume were performed with the open-source Fiji software, with additional plugins such "3D viewer". The samples are tensile dumbbells hot-pressed and cut using the corresponding H3 dice, which are either analyzed directly after being prepared or have recently undergone the cut-healing process in the middle section of the dumbbell (see Chapter II section 4).

We used 80 kV and 180 µA as X-ray parameters, placing the sample vertically with a voxel size of 3 µm. In fact, the distance between the sample and the X-ray beam source (*i.e.*, 14 to 18 mm in our case) is chosen for a better compromise between the volume analyzed and the voxel size. Therefore, this technique does not allow for nanometric object to be analyzed, although aggregates or agglomerates in the sample can be detected. Spatial resolution is often considered to be two or three times the voxel size.

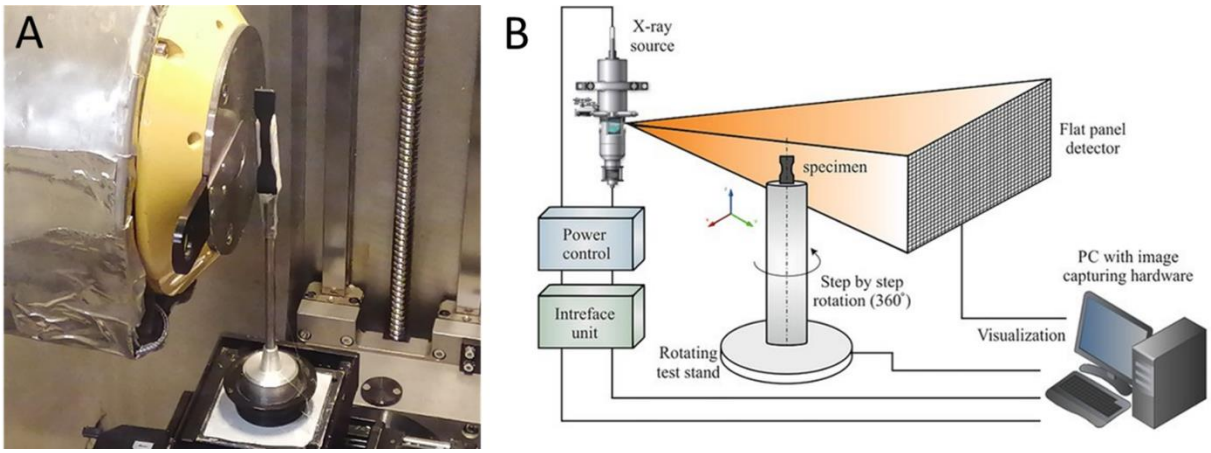

Figure 2.13: (A) Dumbbell sample placed in front of the X-ray beam source for optimal voxel size. (B) Schematic representation of the X-ray tomography setup. [6]

4 Induction heating

Induction heating is a process of heat generation through the application of an alternating magnetic field upon a material. The induction heating device comes in three main parts: the Power cube, the Master controller, and an induction head apparatus (see Figure 2.14A) from CEIA (France). The Power cube 45/900 generates the alternative current of 19 A at 855 kHz, which will feed the coil inducing the magnetic field. The Power cube delivers the alternative current in the form of pulses, which means that, over a certain period, the AC signal is generated as pulses (see Figure 2.14B-C). The ratio of AC pulse over period is referred to as t_{pulse}/t_{period} and ranges from 17% to 100% (see Appendix A). The Master controller v3 manages the induction parameters such as t_{pulse}/t_{period} and the duration of the solicitation. An optical pyrometer SH15/SLE from CEIA can also be added to the setup to measure the temperature in the range of 80 - 700°C and follow precise steps in temperature profiles.

Two types of induction heads are used: a flat spiral coil (see Figure 2.14D) and a two-turn coil (see Figure 2.14E) with 12 and 15 mm in diameter respectively. The spiral coil geometry enables for a reliable thermal measurement of the top surface of the sample and therefore it is the one used for the induction heating characterization and the healing procedures of tensile samples. When the induction heating needed to be coupled with other techniques (*i.e.*, SAXS and XPCS), the two-turn coil geometry was more suitable.

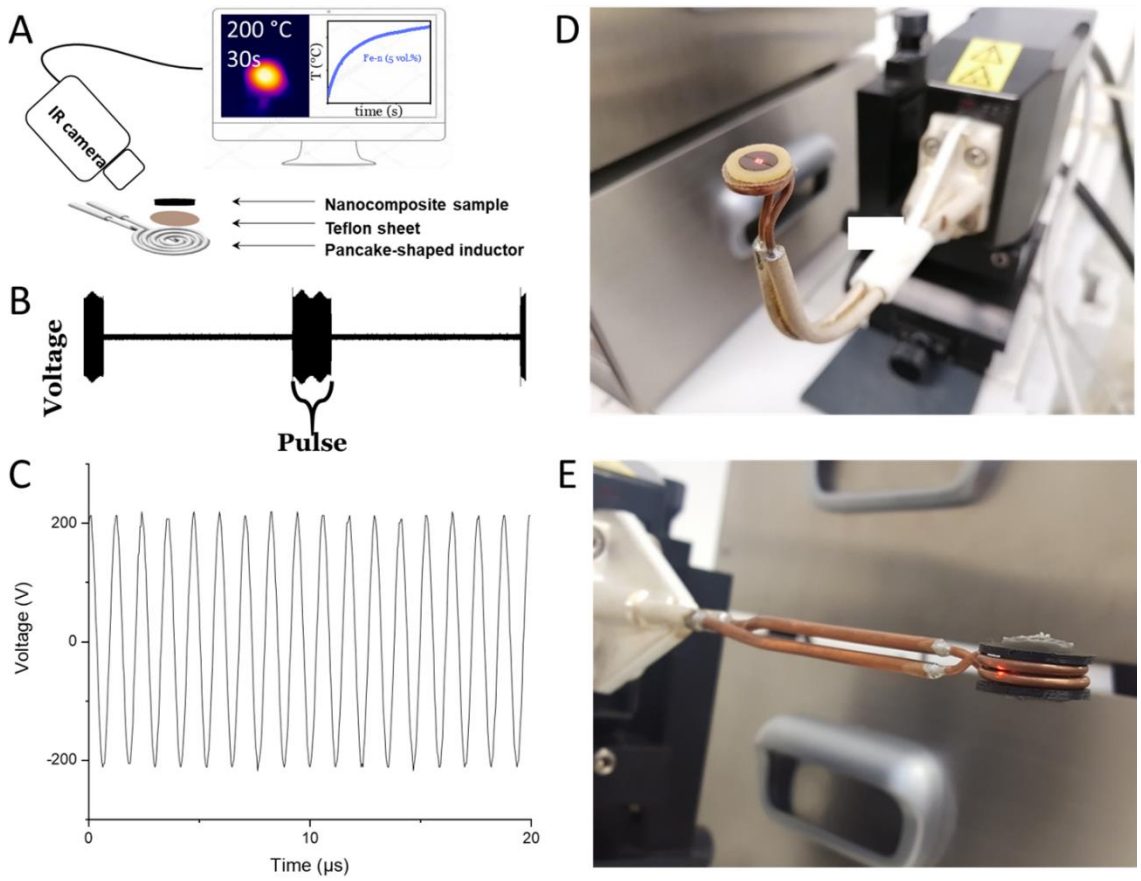

Figure 2.14: (A) Schematic representation of the induction heating setup. (B) Oscillogram of the voltage signal over time, displaying the pulses over periods. (C) Zoom in from the oscillogram indicating 855 kHz as the frequency of the signal. (D) CEIA induction heating head with the flat spiral coil configuration, and a composite sample on top. (E) CEIA induction heating head with the two-turn coil configuration, and a composite sample inside the coil.

Disk-shaped samples (6 mm in diameter and 0.48 to 0.52 mm in thickness) are placed over the spiral coil geometry of the inductor head (see Figure 2.15A) and heated to determine the calorimetric SLP of the sample. All temperatures reported correspond to the maximal temperature of a small area at the center of the sample recorded by the IR camera. A 0.1 mm-thick Teflon composite sheet covers the inductor to protect it from material flowing. The t_{pulse}/t_{period} ratio is set at 17% for the comparison between all composites. The ratio is increased up to 100% for certain measurements with lower filler fraction composites.

All induction heating thermal measurements are set for 60 s. The SLP for each sample is calculated using the following equation:

$$SLP = \frac{C_p (dT/dt)_i}{x_p} \quad \text{(II-3)}$$

with C_p the specific heat capacity, $(dT/dt)_i$ the initial slope from the thermal imaging curve and x_p the weight filler fraction in particles.

Since the amplitude of the magnetic field decreases with the square of the distance to the inductor, the coil-to-sample distance cannot exceed 1 cm. To prevent the coil from overheating, a flow of water is used to cool it down. The setup is completed by an IR camera PI-450 (Optris, Germany) equipped with a 13° lens characterized with an optical resolution of 382 × 288 pixels enabling an accurate spatio-temporal data acquisition of the temperature in the range of 0 - 250°C at 27 Hz. The reliability of the thermal measurements has also been evaluated by comparing them those of a thermocouple for the matrix and the magnetic composites used (see Appendix B). The camera is placed at 20 - 25 cm from the coil/sample to limit interaction with the induction system.

The healing procedure consists of cutting a dumbbell sample, intended for tensile testing, in half (at mid-length) and then, placing the sample on the spiral coil with the center of the coil positioned directly under the cut. The sample is simply placed in a crosslinked rubber mold, with a 0.1 mm-thick Teflon composite sheet being placed between the sample/rubber mold and the coil, and the whole set-up being fixed on a Teflon plate to keep the shape of the dumbbell sample during the healing process (see Figure 2.15B). The optimal t_{pulse}/t_{period} ratio was determined for each of the selected samples to reach a temperature of 180 - 200°C in typically 60 s. Samples are selected for the healing procedure only if they validate certain conditions in thermal, rheological and mechanical behavior. These conditions will be explained through the different chapters of the manuscript.

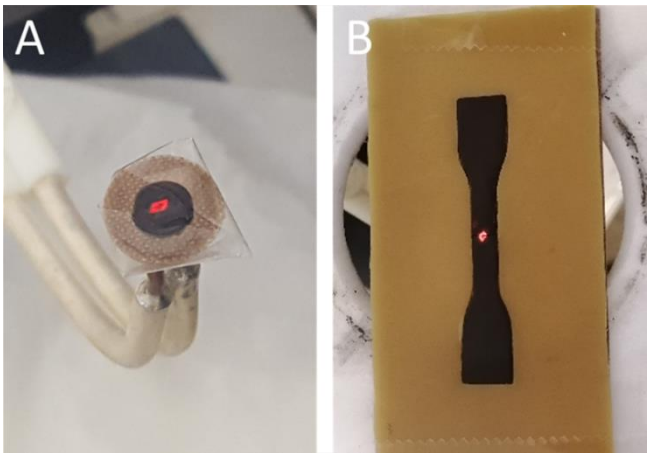

Figure 2.15: (A) Composite disk placed over the spiral coil for an induction characterization. (B) Dumbbell sample cut in half and placed over the spiral coil for the healing procedure. In both cases, the red dot results from the optical pyrometer, which has sometimes been used coupled to the IR camera.

A 3D simulation of the spiral and the two-turn coil is performed with the software COMSOL© to visualize the distribution of magnetic field lines around the coil (see Figure 2.16A). The resulting magnetic field profile indicates a maximum amplitude of 10 - 12 mT within the coil but closer to 4 - 6 mT directly on top of it (see Figure 2.16B), where disk-shaped samples (6 mm in diameter and 0.5 mm in thickness) sit during the measurements placed on top of a Teflon sheet. Figure 2.16C shows the distribution of the magnetic field lines around the two-turn coil. A sample suspended at the center of the coil, as it will be for SAXS and XPCS in-situ measurements, is subjected to a 3 - 4 mT magnetic field amplitude (see Figure 2.16D).

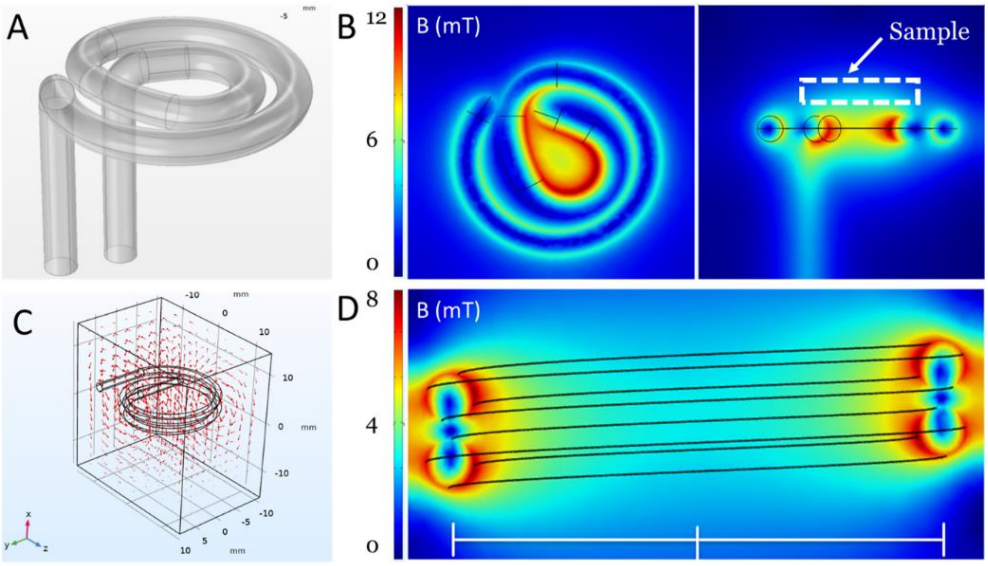

Figure 2.16: (A) 3D model of the flat spiral coil (two concentric turns). (B) COMSOL simulation of the magnetic field around the spiral coil. (C) Spatial distribution of magnetic lines around the two-turn coil. (D) COMSOL simulation of the magnetic field around the two-turn coil (side view).

References

[1] K. Oksman, Y. Aitomäki, A. P. Mathew, G. Siqueira, Q. Zhou, S. Butylina, S. Tanpichai, X. Zhou and S. Hooshmand, "Review of the recent developments in cellulose nanocomposite processing," Composites Part A: Applied Science and Manufacturing, vol. 83, p. 2–18, 2016.

[2] B. Voigtländer, Atomic Force Microscopy, Springer, 2019.

[3] Differential Scanning Calorimetry (DSC).

[4] A. Ghanbari, Z. Mousavi, M.-C. Heuzey, G. S. Patience and P. J. Carreau, "Experimental methods in chemical engineering: Rheometry," The Canadian Journal of Chemical Engineering, vol. 98, p. 1456–1470, 2020.

[5] D. Caruntu, G. Caruntu and C. J. O'Connor, "Magnetic properties of variable-sized Fe3O4 nanoparticles synthesized from non-aqueous homogeneous solutions of polyols," Journal of physics D: Applied physics, vol. 40, p. 5801, 2007.

[6] M. R. Khosravani and T. Reinicke, "On the use of X-ray computed tomography in assessment of 3D-printed components," Journal of Nondestructive Evaluation, vol. 39, p. 1–17, 2020.

Chapter III: Structure & Thermomechanics of Composites

Contents

As previously mentioned in Chapter I, our goal is to develop composites with high strain at failure, high strength and capable to heal under magnetic stimulus. The addition of fillers with different nature, size and shape factor to a TPU matrix, is very likely to modify its mechanical properties and to suppress its ability to flow, yet being a necessary prerequisite to enable its healing. In this chapter, we focus on the structure and thermomechanics characterization of the composites varying systematically the filler content with the aim to make emerge optimal formulations. The acquired knowledge is intended to help in interpreting the healing behavior presented in the upcoming chapter.

First, we characterize the structure of the TPU matrix and of the magnetic composites through complementary microscopy and scattering techniques. Then, thermal characterization on the composites is presented, with a particular focus on characteristic temperatures of interest for our desired application. Finally, we present the mechanical behavior of the composites though uniaxial tensile tests at room temperature and rheological measurements beyond the melting point.

1 Structure of the composites

1.1 Neat TPU matrix structure

AFM experiments were performed on the TPU matrix (Desmopan 85085A) with the objective of revealing the morphology of the hard domains (see Figure 3.1A). This technique, when used in tapping mode and phase contrast, enables to distinguish domains based on their apparent rigidity; see the color gradient from light (hard) to dark gold (soft). The surface of the TPU matrix, prepared through extrusion and subsequent hot-pressing, reveals the presence of long (*ca.* 100-200 nm) HS-based ribbon-like crystallites evenly spaced every 11-14 nm. This type of structure matches the one observed by Nébouy *et al.* [1] as discussed in Chapter I section 1.2. In addition to AFM characterization, we also performed SAXS experiments on the same neat TPU matrix (see Figure 3.1B), providing statistical information representative of the whole sample. A clear peak in intensity can be seen at $q^* = 0.45$ nm^{-1}, which is directly related to the distance between the HS ribbon-like structures such as $d^* = 2\pi/q^* \approx 13$ nm, in excellent agreement with the AFM measurement.

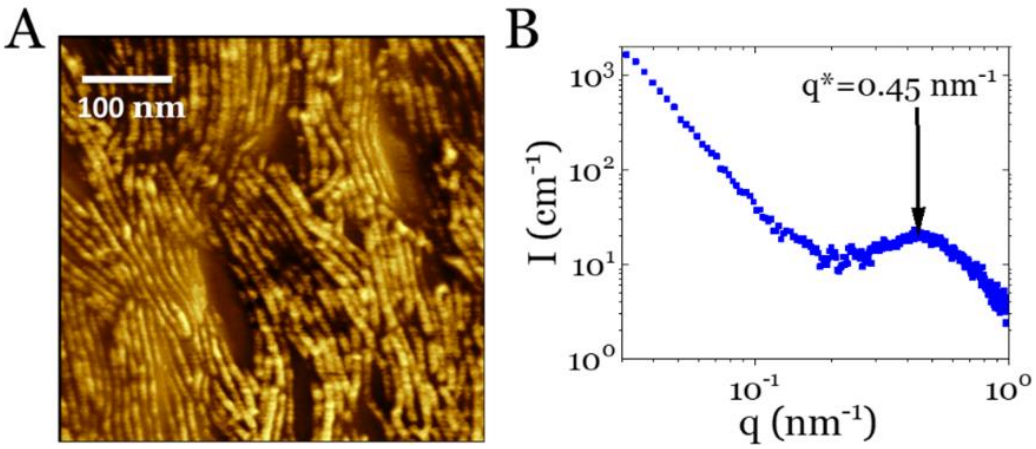

Figure 3.1: (A) AFM micrograph of a hot-pressed TPU sample (Desmopan 85085A). (B) SAXS pattern of the neat TPU emphasizing the inter-ribbon distance.

1.2 Electron microscopy on the composites

We focus on the structure of the processed magnetic composites, with a particular interest on the distribution of fillers within the nanocomposites. TEM and SEM micrographs on Figure 3.2A-C show that at large lengthscales (*i.e.*, over 10 µm), Fe_3O_4, Fe-n and Fe-µ composites display a rather homogenous distribution of particles (systematically for $\Phi = 5$ vol.%). However, it also appears at first sight that aggregates of particles are formed in the case of Fe_3O_4 and Fe-n composites. Moreover, micrographs of the Fe-µ sample indicate a wide distribution of particle sizes, as expected from the supplier information (see Chapter II section 1.2). We remind the reader that we chose economic commercial powders, with no particular surface treatment, in order to be able to upscale the production easily.

To complete the TEM and SEM observations (see Figure 3.3A-B), we provide histograms of particle size distribution determined from all the micrographs taken with the highest resolutions. For each series of composites, we show the size distributions in number and volume. Number distribution was performed using the watershed algorithm for object segmentation and then the volume distribution is determined through the area measurement of each object, assuming spherical particle shapes. The number and volume distributions mostly overlap in the case for Fe_3O_4 composites (see Figure 3.3C), giving *ca.* 15 nm in both average particle number and volume sizes.

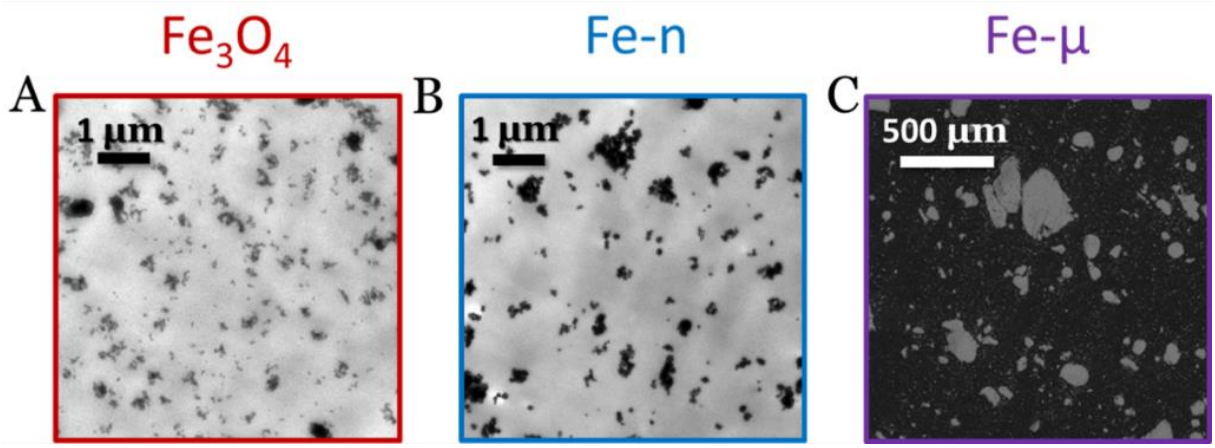

Figure 3.2: TEM and SEM micrographs of composites containing ca. 5 vol.% in (A) Fe_3O_4, (B) Fe-n and (C) Fe-μ magnetic particles.

Fe_3O_4: Elementary particles of Fe_3O_4 form fractal aggregates of *ca.* 100 nm (see Figure 3.3A-B), possibly gathering into larger structures. The range of particle sizes measured from several micrographs indicate a relatively narrow distribution (*ca.* $d_{Fe_3O_4}$ = 10-25 nm), which matches quite well the supplier data reported in Chapter II section 1.2.

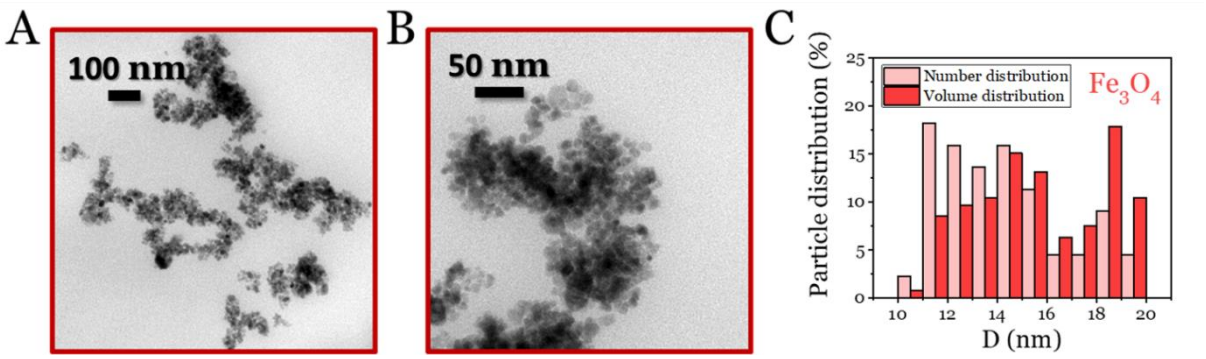

Figure 3.3: (A-B) TEM micrographs of composites containing ca. 5 vol.% in Fe_3O_4 magnetic particles. (C) Number and volume distributions for the corresponding images of Fe_3O_4 filled composites.

Fe-n: Micrographs of Fe-n composites show a wider distribution of particle sizes (*ca.* d_{Fe-n} = 40-140 nm), far wider than the range indicated in Chapter II section 1.2 (see Figure 3.4A-B). Particles aggregate into objects containing several tens of nanoparticles, although these aggregates do not seem as compact as those in Fe_3O_4 composites. As expected, due to the wide distribution in particle sizes, histograms of particle size distribution do not show a perfect

overlap between normal and volume distributions (see Figure 3.4C). Average particle number and volume sizes are *ca.* 75 and 100 nm respectively.

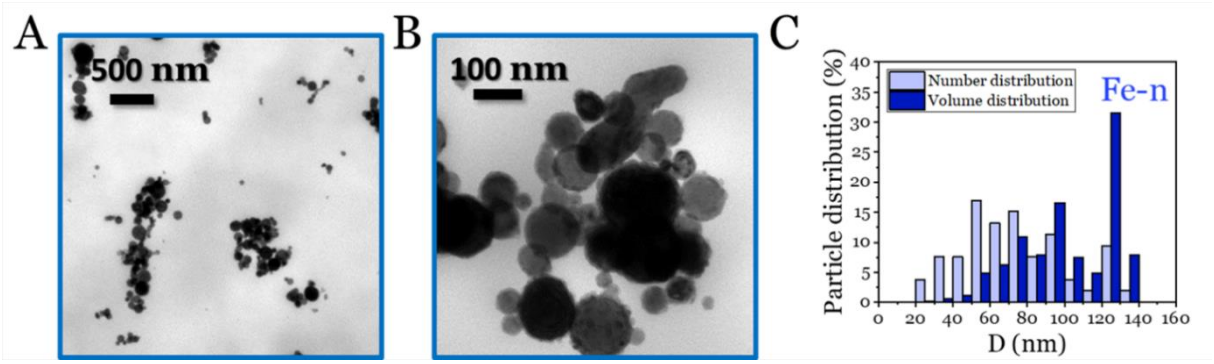

Figure 3.4: (A-B) TEM micrographs of composites containing ca. 5 vol.% in Fe-n magnetic particles. (C) Number and volume distributions for the corresponding images of Fe-n filled composites.

Fe-µ: As stated previously, Fe-µ composites show a wider distribution in size and shape of particles. They contain a large number of micro-particles up to the 40-50 µm range, as well as a non-negligible population of particles under the micrometer size (see Figure 3.5A-B). The latter particles present a needle-like shape, with 300 nm of length and 50 nm of diameter. They appear to be well-dispersed in the matrix and no aggregation is observed for micro-particles nor needle-like particles. The Fe-µ particle size distribution histogram displays accordingly two different populations in Fe-µ particles (see Figure 3.2C), centered around *ca.* 3 and 40 µm in average respectively.

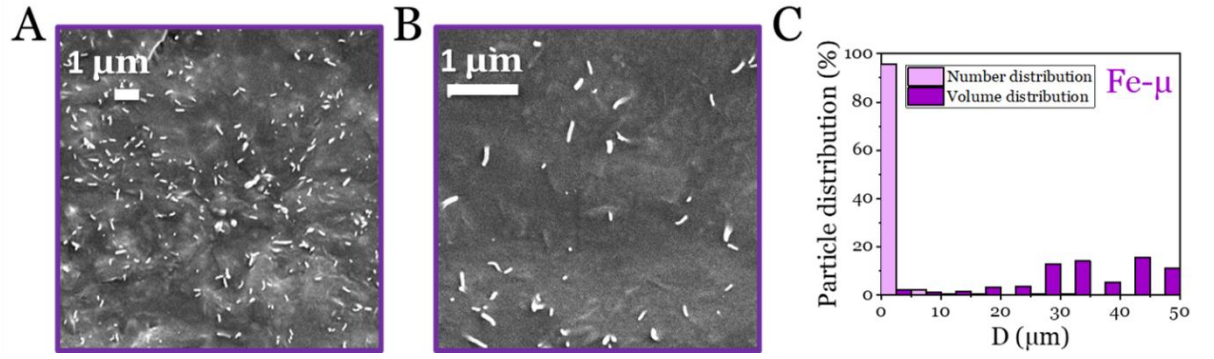

Figure 3.5: (A-B) SEM micrographs of composites containing ca. 5 vol.% in Fe-µ magnetic particles representing an isotropic arrangement of Fe-µ needles. (C) Number and volume distributions for the corresponding images of Fe-µ composites.

1.3 Small-angle X-ray scattering on the nanocomposites

In Figure 3.6, we provide normalized SAXS diffractograms measured on the Fe-n and Fe_3O_4 series of nanocomposites. No relevant signals could be measured on the Fe-µ series because of the presence of very large (several hundreds of µm) objects (see Figure 3.2C).

In the high-q range, both kinds of nanoparticles exhibit a typical q^{-4} power law characteristic of a smooth interface between the soft background (*i.e.*, TPU matrix) and the hard fillers (*i.e.*, magnetic nanoparticles). In this range, oscillations from the form factor would be an indication of monodisperse particle sizes. Here, the lack of oscillations originates from the high polydispersity in size (>20%) in agreement to the micrographs and histograms of both nanocomposites in Figures 3.3 and 3.4. Note that this so-called Porod's regime does not appear in the same (absolute) q-range for both series due to the quite different diameters of nanoparticles (electronic microscopy gives *ca.* 75 nm and *ca.* 15 nm in average for Fe-n and Fe_3O_4 respectively). As expected, normalizing the scattering intensity by the volume fraction in particles (*i.e.*, 1, 5, 10 vol.%) overlaps all the signals at high-q in each series.

At intermediate-q values, an inflexion point is observed, that one can relate to the diameter of the particles (Guinier approximation) such as $D_{SAXS} = 2\pi/q^*$, making the assumption of spherical particles. This leads to $D_{SAXS}^{Fe-n} \approx 80$ nm and $D_{SAXS}^{Fe_3O_4} \approx 15$ nm, in good agreement with the microscopy observations provided in the previous section. Note that no clear structure factor peak is observed due to the high polydispersity of both kind of particles. [2] However, a "correlation hole" caused by the interactions between elementary beads is seen in Fe_3O_4 nanocomposites explaining the slope q^{-2} at intermediate-q followed by a steeper signal at lower-q, from which the slope is often used to quantify the fractal structure of networks at large lengthscale.

At low-q values, while Fe-n particles signal tends to a plateau whose intensity is related to the average mass of the particles, Fe_3O_4-based composites exhibit a slope of $q^{-2.3}$ typical of a branched fractal network whose density seems to increase with the filler content. [3] This is in agreement with the electron microscopy observations in Figure 3.3.

The volume filler fraction increase does not appear to impact the $I(q)$ signal in any significant way, other than the increase in compacity of fractal structures in the case of Fe_3O_4 composites.

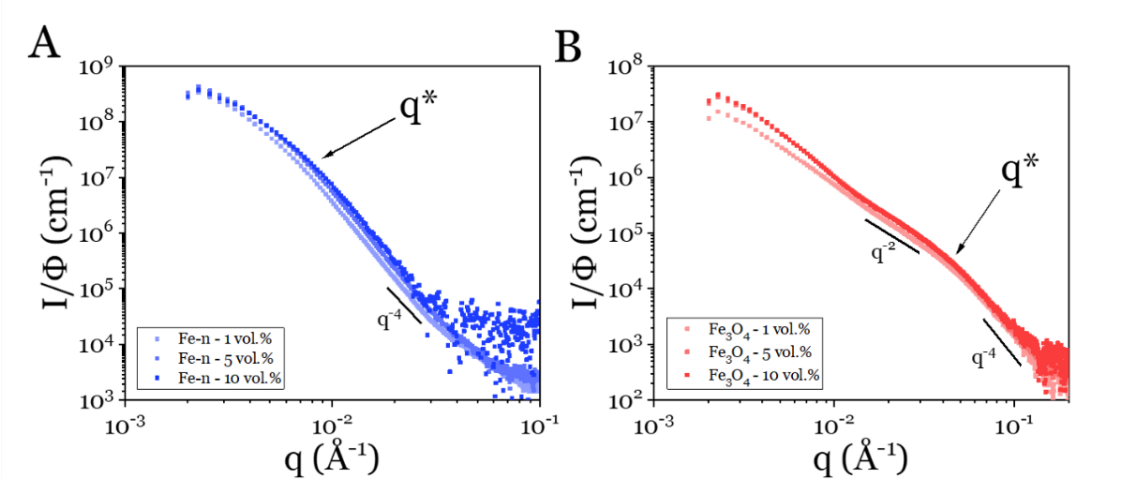

Figure 3.6: SAXS patterns for (A) Fe-n and (B) Fe_3O_4 series of composites.

2 Thermal characterization

This section focuses on the different thermal experiments performed on the three series of composites. The volume fraction in particles in the composites is verified through TGA measurements and the characteristic temperatures of interest through DSC tests.

2.1 Thermogravimetric analysis

In Figure 3.7A-C, we present TGA measurements performed on the three series of composites. We have chosen to show the results between 25°C and 550°C. The weight loss seen in the 275-425°C range is exclusively assigned to the TPU. Then, the inorganic nanoparticles (*i.e.*, Fe_3O_4, Fe-n, Fe-µ) appear to be mostly stable beyond 425°C, leading to the determination of filler content in mass. The results are evaluated at ±1 % relative to the filler mass because of the decomposition of hydroxyl groups on the surface of Fe_3O_4 nanoparticles, [4] leading to mass loss in the same temperature range (see Figure 3.7D). Additionally, Fe-n and Fe-µ particles do not show any relevant loss of mass in the temperature range of the experiment. We limit the temperature of the induction heating process to 200°C with the hope of limiting the polymer degradation, as TGA measurements seem to show the beginning of the degradation at ~275°C.

The corresponding volume filler fractions Φ_f are calculated using the following equation:

$$\Phi_f = \frac{x_f}{x_f + \frac{\rho_f}{\rho_m}(100 - x_f)} \quad \text{(III-1)}$$

where x_f, ρ_f and ρ_m are the filler weight ratio, the filler density (5.17 g cm^{-3} for Fe_3O_4 and 7.87 g cm^{-3} for Fe particles, assuming pure powders) and the TPU density (1.13 g cm^{-3}) respectively.

For the sake of clarity, we refer to the composites according to their nominal filler fractions while actual values measured through TGA are provided in Table 3.1 below and used to determine SAR values in the next chapter.

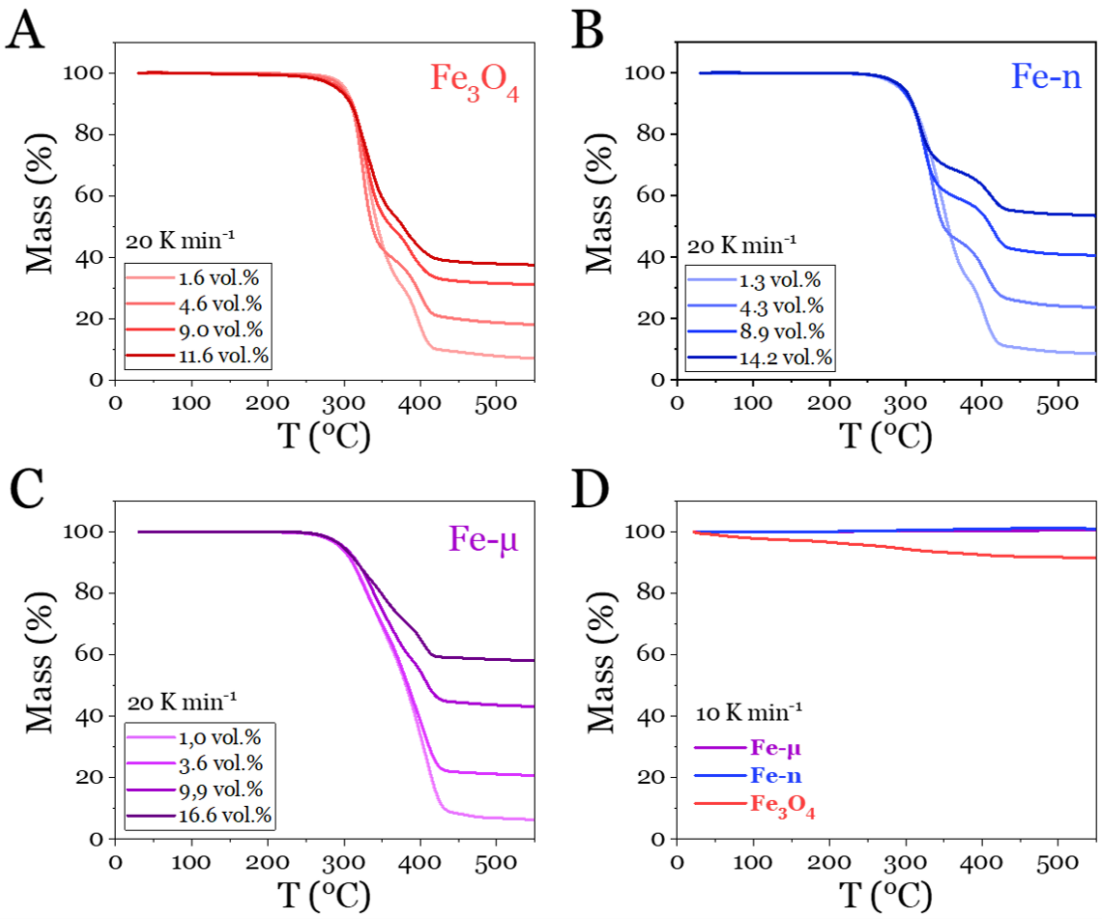

Figure 3.7: Thermogravimetric analysis performed on composites filled with (A) Fe_3O_4, (B) Fe-n and (C) Fe-µ particles. (D) TGA performed on Fe_3O_4, Fe-n and Fe-µ powders.

Nominal fraction	TGA Fe_3O_4	TGA Fe-n	TGA Fe-µ
1 vol.%	1.6 vol.%	1.3 vol.%	1.0 vol.%
5 vol.%	4.6 vol.%	4.3 vol.%	3.6 vol.%
10 vol.%	9.0 vol.%	8.9 vol.%	9.9 vol.%
15 vol.%	11.6 vol.%	14.2 vol.%	16.6 vol.%

Table 3.1: Nominal and measured volume filler fraction in the whole samples set.

The difference between actual and nominal values of filler fractions is assigned to the process chosen for preparing the composites (*i.e.,* extrusion). Discrepancies are possibly due to dispersion and sedimentation of particles in specific corners of the extruder and variations of filler distribution in the processed material. More measurements are needed for confirmation. Another possible source of errors regards the densities used to determine volume fractions. Additionally, FTIR experiments have shown the presence of Fe-O groups at the surface of Fe-n nanoparticles, which indicate an oxidized layer, as well as Fe-OH bonds for Fe_3O_4 nanoparticles (see Chapter II section 1.2).

2.2 Differential scanning calorimetry

As explained in Chapter I section 1, the choice of a TPU as the composite matrix resides in its mechanical properties at room temperature and its capacity to flow above its melting point. The latter depends mainly on the fraction and nature of the HS, ensuring a good thermal stability in service while also enabling a quick phase-transition well below the polymer degradation point. However, once filled with nano-objects, TPUs are likely to behave differently, owing to interactions between polar groups along the chains (ethers, esters, urethanes) and the surface of the fillers. [5] As a result, physical properties such as glass transition (T_g), melting temperature (T_m) and rheological behavior may be modified.

DSC thermograms of our neat TPU and the three series of composites are presented in Figure 3.8 showing that soft domains exhibit a glass transition at -55°C regardless of the nature and content in magnetic fillers. A first endothermic peak is observed from 0 to 50°C corresponding to the melting of SS crystallites made of butanediol polyadipate segments PABD (see Chapter II section 1.1). While Fe_3O_4 and Fe-µ fillers do not show any particular effect on the SS melting, indicating limited interactions between the polymer and the nanoparticles, the situation is

different with Fe-n fillers whose incorporation progressively results in the disappearance of the SS melting signature. This effect must be understood based on the favorable interactions existing between Fe-n particles and the most polar segments of the TPU (PABD SS and HS), supported by the presence of Fe-O groups in FTIR measurements (see Chapter II section 1.2). In fact, increasing the content in Fe-n nanoparticles is also unambiguously seen to reduce both the melting point (appearing in the range 80-150°C) and the fraction of crystalline HS, synonymous of a significant alteration of the whole polymer network. Conversely, no significant change in the HS melting temperatures is observed when Fe_3O_4 is added to the matrix. Also, the lack of visible interaction between both SS and HS and the Fe-µ particles is further expected because of the latter's much lower specific surface due to the large ratio of particle sizes above 10 µm. All these observations are summarized in Figure 3.9, where we represent both the SS and HS melting enthalpy as a function of the filler fraction. Of particular importance for the healing process, all the crystalline domains of TPU have completed their melting above 150°C.

In order to estimate the crystalline ratio of SS and HS in the TPU, we propose an estimation of both the specific melting enthalpy of pure HS and SS based on the molecular structure of the TPU. HS are made of 2 HDI and 1 HDO segments for which the specific melting enthalpy were determined to be 110.8 J g^{-1} and 216 J g^{-1} respectively. [6] Considering their molecular weight fraction in HS, [7] one obtains in the neat TPU $\Delta H^*_{HS} \approx 138.2$ J g^{-1}. Although the SS are made of two different polymers (PPO and PABD), only the latter one is likely to crystallize. In consequences, one can directly refer to its specific melting enthalpy $\Delta H^*_{SS} \approx 123.9$ J g^{-1}. [8]

From these values and the DSC measurements presented in Figure 3.8A-C, crystalline ratios for both species appear to be mostly in the 9-10 wt.% range for SS and in the 12-14 wt.% range for HS, regardless of the filler content, except in Fe-n composites, in which the increase in filler content perturbs significantly the structure of the TPU (see Table 3.2).

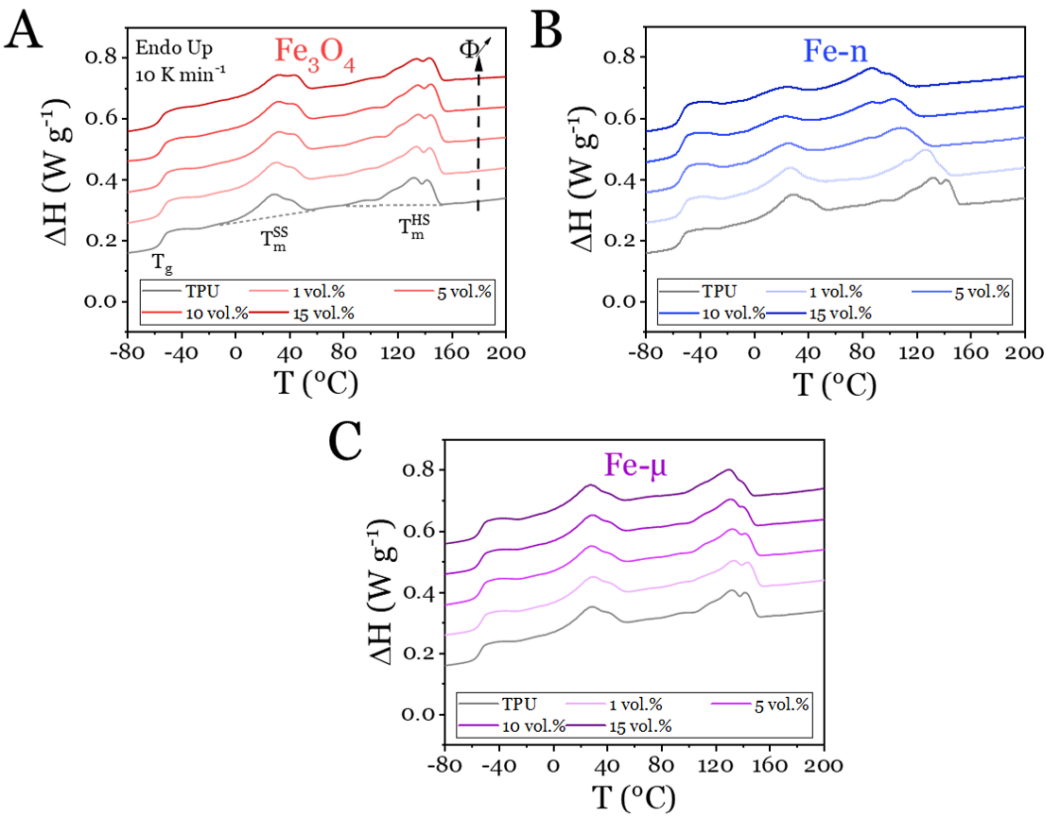

Figure 3.8: DSC thermograms series measured from the TPU matrix and composites loaded with ca. 1, 5, 10 and 15 vol.% in (A) Fe_3O_4, (B) Fe-n and (C) Fe-μ respectively. The second heating segment is shown. The heat flux is normalized by the TPU mass. Nanocomposite's data are shifted for clarity.

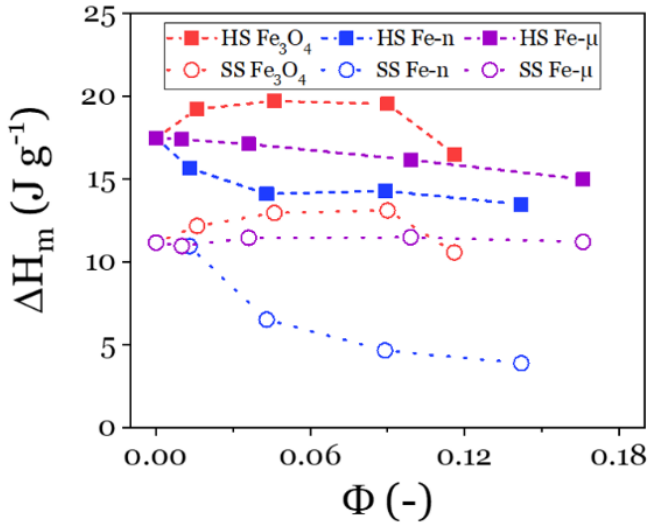

Figure 3.9: HS and SS melting enthalpy extracted from DSC thermographs in Figure 3.8, dotted lines are guides for the eye.

	Fe_3O_4		Fe-n		Fe-µ	
Sample	X_c^{SS} (wt.%)	X_c^{HS} (wt.%)	X_c^{SS} (wt.%)	X_c^{HS} (wt.%)	X_c^{SS} (wt.%)	X_c^{HS} (wt.%)
TPU matrix	9.0	12.6	-	-	-	-
1 vol.%	9.8	13.9	8.8	11.3	8.9	12.6
5 vol.%	10.5	14.3	5.3	10.2	9.3	12.4
10 vol.%	10.6	14.1	3.8	10.3	9.3	11.7
15 vol.%	8.5	11.9	3.1	9.8	9.1	10.8

Table 3.2: Crystalline HS and SS ratios calculated for the three series of composites.

3 Mechanical response

This section aims at selecting the composites with the proper viscoelastic behaviors, while also showing that they are capable of being repaired through the magnetic-stimulated healing process.

3.1 Tensile tests

The mechanical performance in service is a crucial requirement for the composites. While adding micro- or nanoparticle to the TPU matrix is expected to enhance its stiffness at low deformation (reinforcement [9]), being useful to improve wear resistance, the behavior at large amplitude may, on the other hand, be strongly impacted by the creation of defects favoring crack initiation and propagation. In Figure 3.10A-C, we present quasi-static tensile tests performed on the three series of nanocomposites revealing these effects. At low strain, the strain-stress behavior of the composites remains almost unchanged, regardless of the nature or filler content. A quantitative analysis of this region reveals different reinforcement tendencies to the Young's modulus with the increase of particle content. In particular Figure 3.11B indicates that Fe_3O_4 particles reinforce significantly more the TPU than Fe-n ones as one may have expected from their higher specific surface and pre-aggregated fractal nature favoring mechanical percolation. Besides, as expected, a notable decrease in strain at break occurs with increasing filler fraction. This is further highlighted in Figure 3.11A, gathering the whole data set in terms of energy at failure (W_{break}) versus filler fraction, showing a similar trend

regardless of the particle's nature. For the sake of clarity, we have gathered the relevant parameters derived from the uniaxial tensile experiments in Table 3.3.

From the sole tensile test point of view, the most promising composites for our study are those finding a compromise between modulus enhancement and strain at break reduction. Composites loaded with 1-5 vol.% in magnetic particles seem, in consequence, the most appropriate.

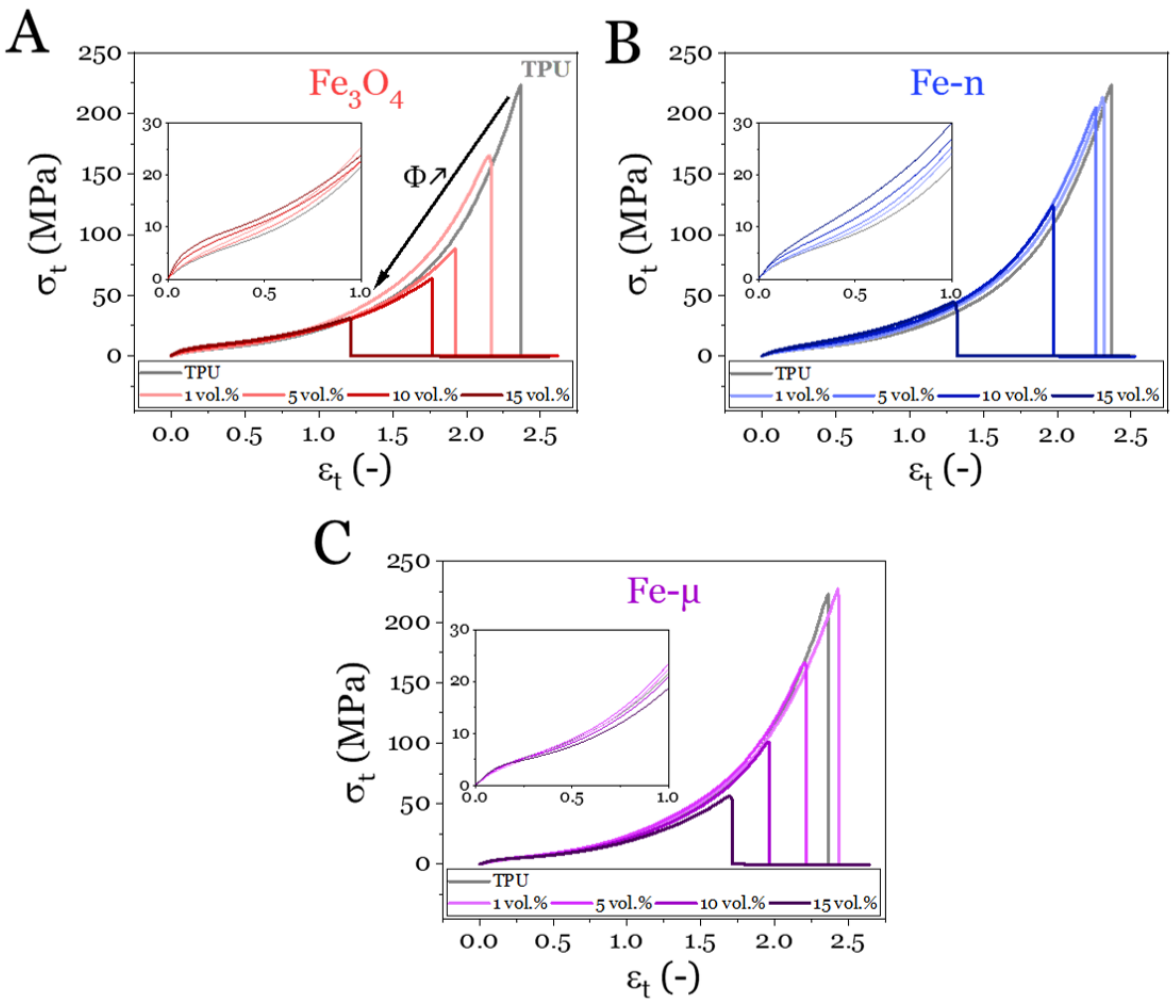

Figure 3.10: (A-C) Tensile tests (true stress vs. true strain) carried out on the TPU matrix and on composites loaded with ca. 1, 5, 10 and 15 vol.% in Fe_3O_4, Fe-n and Fe-μ respectively, performed at 10 mm min^{-1}. Inserts are zoom-ins for low strains.

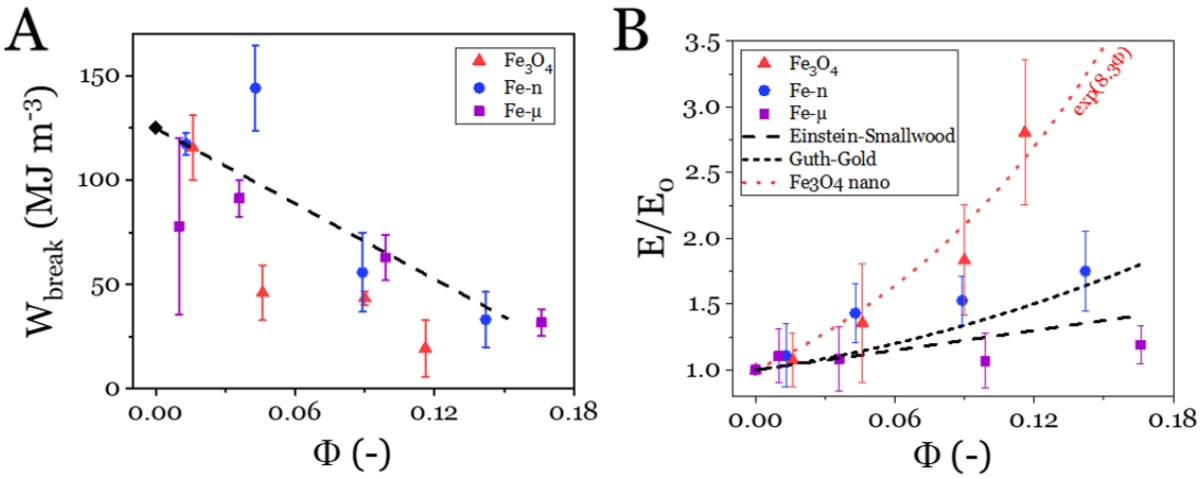

Figure 3.11: (A) Work at break as a function of the volume fraction in filler for the whole set of composites. The dotted line is a linear guide for the eye. (B) Normalized Young's modulus as a function of the filler fraction showing the reinforcement effect. Dashed lines stand for the hydrodynamic models of Einstein-Smallwood ($E/E_0 = 1 + 2.5\Phi$) and Guth-Gold ($E/E_0 = 1 + 2.5\Phi + 14.1\,\Phi^2$).

Sample	ε_{break} (-)	σ_{break} (MPa)	E (MPa)	W_{break} (MJ m^{-3})
TPU matrix	2.37	223	34	125
1 vol.% Fe_3O_4	2.3 ± 0.3	200 ± 6	37 ± 2	116 ± 16
5 vol.% Fe_3O_4	1.5 ± 0.5	53 ± 5	47 ± 9	46 ± 14
10 vol.% Fe_3O_4	1.7 ± 0.4	61 ± 4	63 ± 8	43 ± 4
15 vol.% Fe_3O_4	0.9 ± 0.6	19 ± 4	96 ± 12	19 ± 14
1 vol.% Fe-n	2.3 ± 0.2	213 ± 1	38 ± 3	117 ± 6
5 vol.% Fe-n	2.4 ± 0.3	245 ± 6	49 ± 2	144 ± 21
10 vol.% Fe-n	1.8 ± 0.6	93 ± 6	52 ± 2	56 ± 19
15 vol.% Fe-n	1.5 ± 0.5	53 ± 5	60 ± 4	33 ± 14
1 vol.% Fe-μ	2.0 ± 0.6	131 ± 9	38 ± 2	78 ± 43
5 vol.% Fe-μ	2.1 ± 0.3	155 ± 4	37 ± 3	91 ± 9
10 vol.% Fe-μ	2.0 ± 0.4	106 ± 4	37 ± 2	63 ± 11
15 vol.% Fe-μ	1.7 ± 0.3	57 ± 3	41 ± 1	32 ± 7

Table 3.3: Mechanical properties of Fe_3O_4, Fe-n and Fe-μ composites, determined through uniaxial tensile tests at 10 mm min^{-1}.

3.2 Rheological tests

TPU melting is necessary to trigger the healing process. However, it may not be a sufficient condition to make the composites flow and promote macroscopic healing or surface smoothening. Therefore, it is important to understand how the material flows above the melting point (see Figure 3.8) once all the crystallites have melted (*i.e.*, above 150°C) and how this behavior evolves with increasing particle content. Indeed, it is well known that the addition of micro- and/or nanoparticles to a polymer melt changes its rheological properties. The latter are mostly dependent on the particles fraction and dispersion as well as their interactions with the polymer chains. Series of frequency sweep measurements (*i.e.*, storage (G') and loss (G'') shear moduli as a function of the pulsation ω) were performed on the three types of nanocomposites at T =180°C above the TPU melting point ($T_m \approx$ 150°C) (see Figure 3.12A-C), where G' and G'' are displayed as full and open symbols respectively.

First, it worth to note that at 180°C, the storage modulus G' of the TPU is lower than its loss modulus G'' on the whole range of accessible ω, indicating that the molten TPU behaves as an almost homogeneous liquid-like material. In fact, the storage and loss moduli vary respectively as $G' \sim \omega^2$ and $G'' \sim \omega^1$, synonymous of a Maxwellian fluid [10] (see Chapter I section 1.2), apart at very low frequency range suggesting a slight degree of remaining phase separation. [11] The composites would need to have a similar rheological behavior as the chosen TPU matrix (above their melting point) to confirm their ability to flow, being crucial for materials healing.

Increasing progressively the particle content is likely to make the material more elastic until reaching a possible viscoelastic solid state (or "gel") satisfying $G' > G''$ with both G' and G'' being independent of ω. This usual trend is visible in Figures 3.12A-B in both Fe_3O_4 and Fe-n series where the nanocomposite melts see their elasticity growing (or G''/G' decreasing) with the particles content until reaching solid-like properties at *ca.* 15 vol.% ($G" < G'$). Nevertheless, we believe that the physical origin of such gelation is different in those two systems. Indeed, Fe_3O_4 particles are significantly smaller and organized in a different way with respect to the Fe-n ones (see Figures 3.3 and 3.4). In particular, their higher specific surface implies a larger interface with the matrix, and their pre-aggregated morphology enhances their ability to form branches likely to percolate across the TPU. In spite of a lower specific surface area, DSC thermograms in Figure 3.8B clearly underlined the preferential interactions of larger and well-spherical Fe-n particles with the TPU, likely to explain the creation of an elastic network in the 15 vol.% Fe-n filled composite, being as strong as in the case of its Fe_3O_4 counterpart. In great

contrast with Fe_3O_4 and Fe-n series, the addition of Fe-µ particles into the TPU are seen to have a limited impact on its rheology with no relevant change in neither G' nor G" (see Figure 3.12C). We assign this behavior to a much lower specific surface area and no significant interaction with the polymer chains, in good agreement with DSC results reported in Figure 3.8C. For the sake of clarity, we report in Figure 3.13 the global evolution of the storage modulus at 10 rad s^{-1} ($G'(\omega_{10})$) of the three series of composites. Nanocomposites filled with 1-5 vol.% in particles flow on a reasonably short timescale (see Figure 3.12A-C), with their final relaxation time at 180°C being shorter than 0.01 s, resulting in $G'' > G'$. From the rheological point of view, they consequently appear to be promising candidates for the design of healable materials.

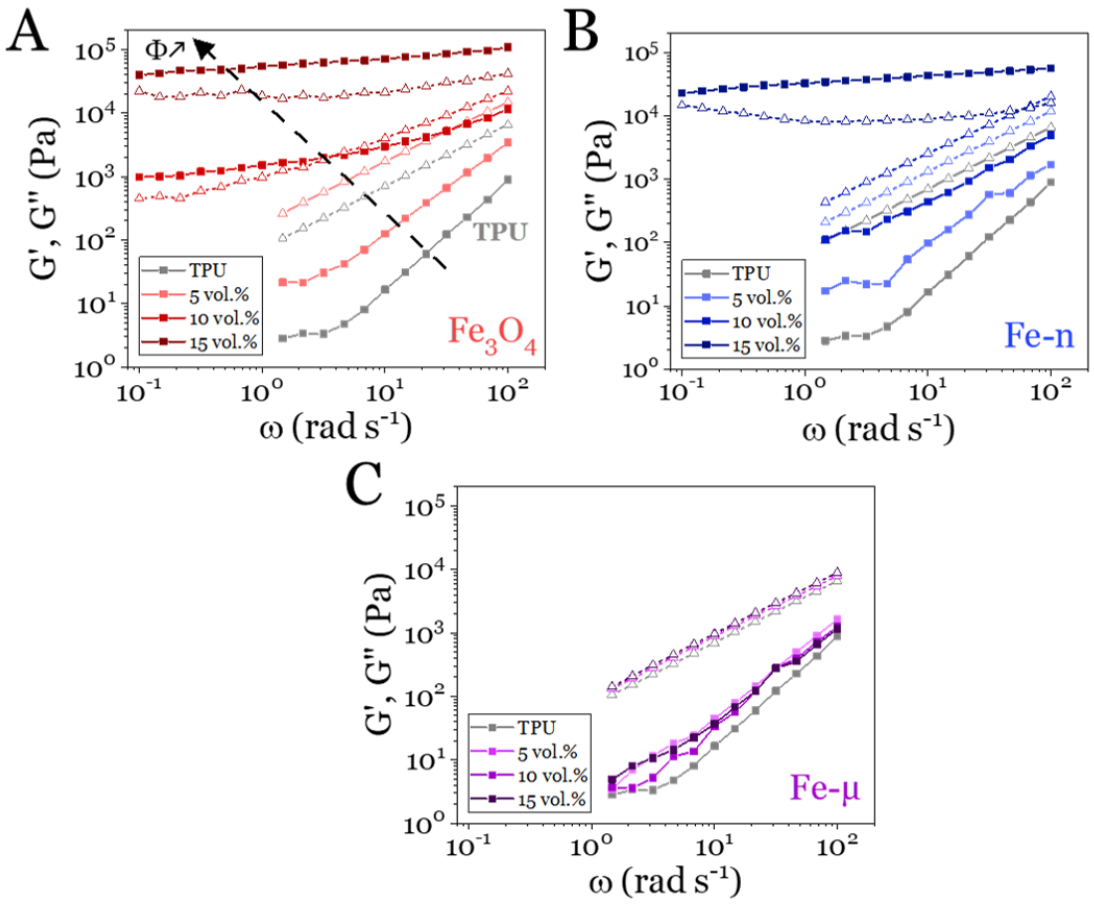

Figure 3.12: Rheological frequency sweep measurements measured at 180°C for the three series of composites ca. 1, 5, 10 and 15 vol.% in (A) Fe_3O_4, (B) Fe-n and (C) Fe-µ. Full and open symbols correspond to the storage modulus G' and the loss modulus G" respectively.

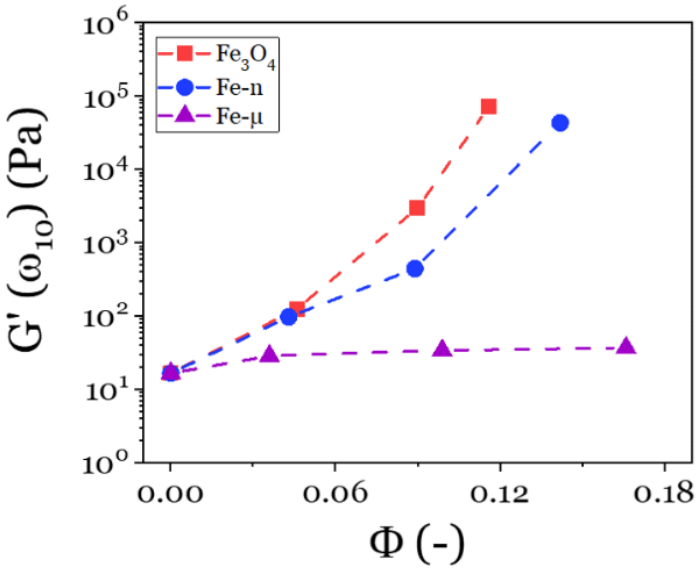

Figure 3.13: Storage modulus value at 10 rad s^{-1} and 180°C as a function of the filler volume fraction for the three series of composites – extracted from Figure 3.12. Dotted lines are guides for the eye.

In conclusion, we understand how the filler content impacts the structure and the thermomechanical behavior of the sample. We have identified the formulations which seem suitable to produce healable composites from a mechanical (both solid and liquid) point of view. Composites with 1 and 5 vol.% in fillers are, in fact, capable of flowing rapidly above the TPU melting point and have the best compromise of Young's modulus enhancement and deformation at failure (close to the neat TPU's one), regardless of the filler nature. In particular, Fe_3O_4 and Fe-n composites loaded with 5 vol.% of particles present a significant reinforcement at small deformation while keeping a reasonable strain at failure, making them promising candidates for the formulation of healable composites. The next step of our investigation consists in evaluating the ability of the composites to generate heat. In fact, while low (1-5 vol.%) particles content formulations enhance strain at failure and ability to flow, they may on the contrary suffer from a too low ability to heat under the magnetic stimulus. Because we have observed a full melting of all the crystallites around 150 °C, and a beginning of polymer degradation around 250 °C, we will now target a healing temperature around 180 °C.

References

[1] M. Nébouy, A. de Almeida, S. Brottet and G. P. Baeza, "Process-oriented structure tuning of PBT/PTHF thermoplastic elastomers," Macromolecules, vol. 51, p. 6291–6302, 2018.

[2] G. P. Baeza, A.-C. Genix, C. Degrandcourt, L. Petitjean, J. Gummel, M. Couty and J. Oberdisse, "Multiscale Filler Structure in Simplified Industrial Nanocomposite Silica/SBR Systems Studied by SAXS and TEM," Macromolecules, vol. 46, pp. 317-329, 2013.

[3] G. D. Soto, C. Meiorin, D. G. Actis, P. M. Zélis, O. M. Londoño, D. Muraca, M. A. Mosiewicki and N. E. Marcovich, "Magnetic nanocomposites based on shape memory polyurethanes," European Polymer Journal, vol. 109, p. 8–15, 2018.

[4] C. W. Lai, F. W. Low, M. F. Tai and S. B. Abdul Hamid, "Iron oxide nanoparticles decorated oleic acid for high colloidal stability," Advances in Polymer Technology, vol. 37, p. 1712–1721, 2018.

[5] E. J. Bailey and K. I. Winey, "Dynamics of Polymer Segments, Polymer Chains, and Nanoparticles in Polymer Nanocomposite Melts: A Review," Progress in Polymer Science, p. 101242, 2020.

[6] H. Landolt and R. Börnstein, Thermodynamic Properties of Organic Compounds and Their Mixtures: Enthalpies of Fusion and Transition of Organic Compounds. Subvol. A, Springer, 1995.

[7] T. Kajiyama and W. J. MacKnight, "Thermal properties of polyurethanes. Enthalpies and entropies of fusion," Polymer Journal, vol. 1, p. 548–554, 1970.

[8] I. B. Rabinovich, V. P. Nistratov, A. G. Babinkov, K. G. Shvetsova and V. N. Larina, "Thermodynamic properties of polybutyleneglycol adipate," Polymer Science USSR, vol. 26, p. 826–831, 1984.

[9] Y. Song and Q. Zheng, "Concepts and conflicts in nanoparticles reinforcement to polymers beyond hydrodynamics," Progress in Materials Science, vol. 84, p. 1–58, 2016.

[10] M. Rubinstein and R. H. Colby, Eds., Polymer Physics, Oxford University Press, 2003.

[11] M. Nébouy, A. de Almeida, L. Chazeau and G. P. Baeza, "Modeling shear-induced crystallization in startup flow: The case of segmented copolymers," Journal of Rheology, vol. 63, p. 837–850, 2019.

Chapter IV: Magnetic Induction Heating

Contents

After having performed an extensive analysis of the structure and of the thermomechanical behavior of the magnetic composites in Chapter III, we now focus on the understanding of their ability to heat under an alternating magnetic field. The objective of this chapter is to evaluate which composites can reach the temperature needed for healing to occur (i.e., above T_m) under oscillatory magnetic solicitation. First, we characterize both the electrical and the magnetic properties of the composites through broadband dielectric spectroscopy (BDS) and superconducting quantum interference device (SQUID) tests. Then, we expose the three series of composites to magnetic induction and follow the evolution over time of their temperature profiles through thermal imaging, allowing for a reliable way of following the temperature of the whole sample at a safe distance from the magnetic field lines.

1 Electromagnetic rationalization

A series of measurements need to be performed to identify the magnetic mechanisms occurring in the composites once they are submitted to an alternating magnetic field (855 kHz, *ca.* 4-6 mT). As explained in Chapter I section 2.4, the heat can be produced through two distinct mechanisms: (i) eddy currents originating from the electrons motion in conductive materials, generating heat through Joule effect and, (ii) magnetic hysteresis losses that originate from a delay in the (re)orientation of spins in the direction of the applied magnetic field. This phenomenon can involve either Néel relaxation, Brown relaxation, or magnetic walls motion according to the size of the particles and the viscosity of the surrounding matrix. Therefore, the main objective for this section is to determine the heating mechanisms taking place for each series of composites.

1.1 Broadband dielectric spectroscopy

Dielectric frequency sweeps [1] for the three series of composites measured at room temperature (*i.e.*, 25°C) are displayed in Figure 4.1A-C. Real (ε') and imaginary (ε") parts of the complex permittivity are measured with varying the frequency of the solicitation. Focusing on the imaginary part ε_r'' (solid lines), one can observe a low-f upturn generated by the long-range motion of charge carriers, related to the electric conductivity of the material. Then, a peak appears around 10-1000 Hz usually assigned to the Maxwell-Wagner-Sillar (MWS) processes [1] caused by interfaces polarization which occurs in heterogeneous materials such as semi-crystalline polymers [2] or nanocomposites. [3] Note that the increase in ε_r'' at high frequencies

indicates the beginning of the SS α-relaxation. While it is not the scope of the present work to investigate its characteristics (related to the T_g of the TPU), one could easily study their evolution by decreasing the temperature.

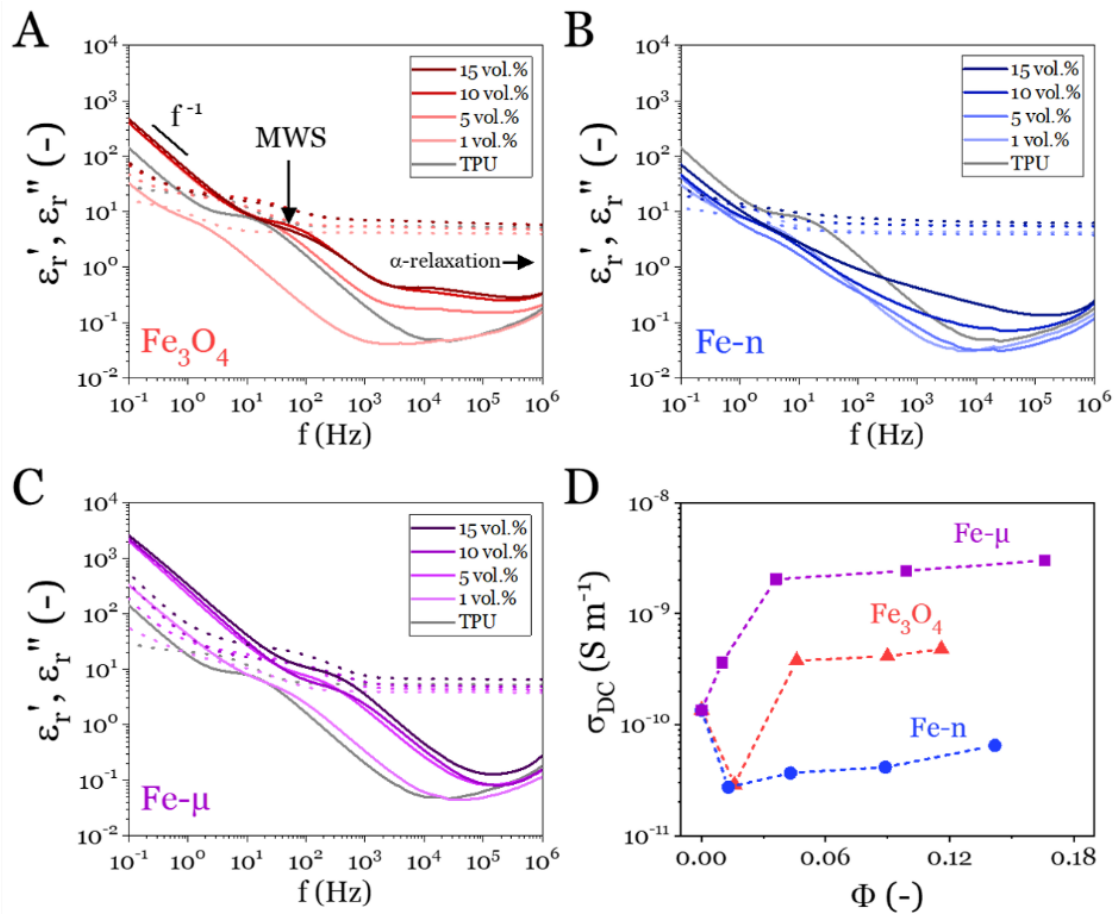

Figure 4.1: BDS measurements performed at 25 °C on the TPU matrix and the three series of composites (A) Fe_3O_4, (B) Fe-n and (C) Fe-μ based composites. The imaginary part of the complex permittivity ε_r'' is displayed in solid lines while the real part ε_r' is shown in dotted lines. (D) Direct current conductivity determined from the BDS measurements. Dotted lines are guides for the eye.

Focusing on the lowest frequencies window enables the extraction of the direct current (DC) electric conductivity (σ_{DC}) through $\varepsilon_r''(f \to 0) = \frac{\sigma_{DC}}{\varepsilon_0} f^{-1}$. Figure 4.1D shows the DC conductivity for the three series of nanocomposites as a function of the filler content. Here, the main observation is that adding conductive particles to the TPU does not make the composites electrical conductors, excluding *de facto* eddy current as a source of heat. In fact, their conductivity is not sufficient to generate Joules effect (*e.g.*, 10^7 S m^{-1} for bulk iron). Even in the case of a sufficiently high conductivity, the size of the electric path must be larger than 1

cm to produce a significant amount of heat. [4] In brief, it is clear that eddy currents will not be relevant in the framework of this study.

1.2 Magnetic characterization

ZFC-FC curves, detailed in Chapter II section 3.7, were measured to study the complex magnetization (M^*) of the composites filled with *ca.* 15 vol.% of particles as a function of temperature (see Figure 4.2A) under quasistatic conditions ($H = 4$ kA m^{-1}, $f = 0.5$ Hz).

First, we will consider the ZFC-FC curves of the Fe_3O_4 composite. The strong difference between the ZFC and the FC curves in the Fe_3O_4 composite indicates unambiguously their superparamagnetic nature (see Chapter I section 2.3.3), in agreement with their size (*i.e.*, 15 nm in average according to measurements made in Chapter III section 1.2). [5] In the work of Tanwar *et al.*, [6] Fe_3O_4 superparamagnetism is correlated to a blocking temperature close to $T_B^{Fe_3O_4} = 95$ K for monodisperse and isolated 10 nm particles at 4 kA m^{-1}. The blocking temperature, corresponding to the ZFC-FC crossover position, is however shifted to a much higher temperature (*ca.* 300 K) in our case due to the aggregation of elementary beads resulting into strong inter-aggregate dipolar interactions (see Figure 4.2A). [7-9] This phenomenon is further supported by ZFC tests measuring the magnetization loss M'' and performed at 1 kHz (see Figure 4.2B). The maximum of M'' linked to the maximal energy dissipation, corresponding to the apparent blocking temperature, is situated at $T_{agg}^{Fe_3O_4} = 200$ K. It can also be noted that the Verwey transition, which indicates the change between monoclinic and cubic crystal systems for Fe_3O_4, is detected at $T_V^{Fe_3O_4} = 100$ K. [10]

In contrast to the observation on Fe_3O_4 composites, ZFC-FC curves for Fe-n and Fe-µ composites indicate that the corresponding particles are seen as multi-domain, as expected from their sizes (75 nm and 3 µm respectively in average). Nevertheless, one can still observe in Figure 4.2B the blocking temperature of Fe close to $T_B^{Fe} = 20$ K in both powders indicating the presence of elementary nano-objects showing a superparamagnetic state. [11] This is further supported by the measurement on the Fe-n composite where a dissipation peak is seen close to 280 K in Figure 4.2B. Conversely, the magnetization loss in Fe-µ remains extremely low, indicating the predominance of a multi-domain behavior.

To summarize, the three series of composites should be able to heat under an alternating magnetic field through magnetic hysteresis losses. Under the TPU's melting point, Fe-n and

Fe-µ multi-domain magnetic particles heat through domain-wall motion, whereas Fe_3O_4 single-domain superparamagnetic particles heat through Néel relaxation.

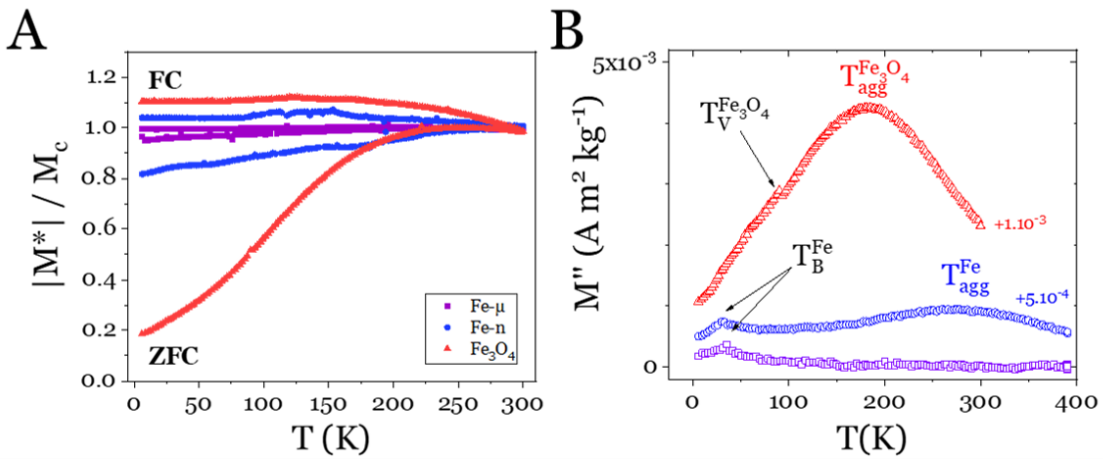

Figure 4.2: (A) ZFC and FC curves measured between 0 and 300 K on composites loaded with ca. 15 vol.% in Fe_3O_4, Fe-n and Fe-µ. The complex magnetization M^* has been normalized by the highest ZFC value M_c for the respective measurement. (B) Imaginary part of the magnetization M" (ZFC curve) as a function of the temperature revealing blocking temperatures in the same composites.

To complete the magnetic characterization of our samples, magnetization tests in $M = f(H)$, detailed in Chapter II section 3.7, were performed at room temperature under quasi-static conditions (see Figure 4.3). We tested composites filled with *ca.* 15 vol.% in Fe_3O_4, Fe-n and Fe-µ resulting in comparable magnetic susceptibility of 2.0, 1.4 and 1.1 respectively. Also, the magnetic saturation (M_s) qualitatively agrees with our expectations: (i) Fe-n and Fe-µ samples exhibit higher M_s than Fe_3O_4 ones due to the chemical nature of the particles [12] and (ii) Fe-n samples exhibit lower M_s value than Fe-µ ones because of their restricted particle size. [13] Besides, as expected for very low frequency, these curves display no significant hysteresis between the magnetization and demagnetization steps apart from the 15 vol.% Fe-n composite which exhibits a slight dissipation. Higher frequencies (above 100 kHz, like in our induction heating experiments) will enhance the hysteresis loss and thus generate a significant amount of heat (as seen in Chapter I section 2.4.2). Note that high frequency $M = f(H)$ experiments [14, 15] were not possible at high magnetic amplitude with the device we used.

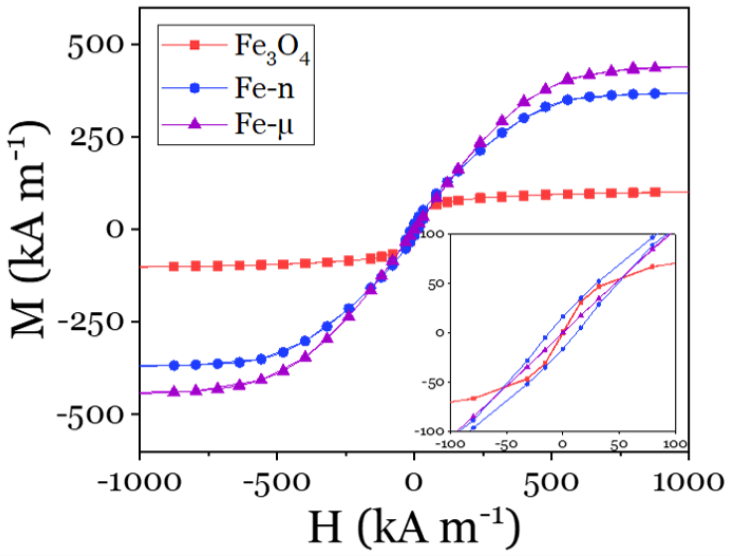

Figure 4.3: Magnetization curves performed at 300 K under a quasi-static magnetic solicitation for composites loaded with ca. 15 vol.% in Fe_3O_4, Fe-n and Fe-μ, normalized by the mass of the sample. The inset is a zoom in the origin.

2 Induction heating

We evaluate each magnetic composite's capacity to generate heat in the presence of an alternating magnetic field. Samples placed over the pancake coil of the magnetic inductor (see Chapter II section 4) were subjected to a 4-6 mT alternating magnetic field at 855 kHz, mainly using the lowest available pulse duration t_{pulse}/t_{period} (*i.e.*, 17%). We target a wide range of temperatures (*i.e.*, from 150 to 250°C) to trigger the TPU melting without significant polymer degradation, while limiting our healing processes to 30-120 s to prove the rapidity of this procedure.

To establish suitable conditions of healing and mechanical recovery, it is crucial to monitor the temperature evolution during the treatment in order to optimize flow rate and structural stability of the sample. The evolution of the temperature as a function of alternating magnetic field exposition time for the three series of nanocomposites is given in Figure 4.4A-C. The Fe_3O_4 series appears to be the simplest to rationalize since it seems to follow the case in which particles dissipate a constant amount of heat in their surrounding medium regardless of the experimental time and temperature. This well-established situation results in an increase of the temperature of the material with a continuously decreasing rate dT/dt until reaching a permanent regime.

This profile, fitted with Equation IV-1, being the 0-dimension solution of the heat equation for a constant energy flux, indicates the involvement of a single heating mechanism, assigned to the hysteresis losses originating from Néel relaxation characteristic of single-domain particles. In Equation IV-1, T_0, ΔT and τ stand respectively for the room temperature (≈ 22 °C), the amplitude of the heating process (°C) and its characteristic time (s).

$$T(t) = T_0 + \Delta T(1 - e^{-t/\tau}) \quad \text{(IV-1)}$$

While a "single heating mechanism" behavior is also observed for Fe-n and Fe-µ composites at 1 vol.%, the temperature profiles recorded at higher filler fractions are qualitatively different. In fact, it is clear that a second mechanism is triggered in both series when the materials temperature approaches the TPU melting point. This behavior is particularly visible in the case of 5 vol.% Fe-µ composite, where the appearance of the additional heating mechanism is clearly marked. This additional heat dissipation originates from the dramatic fall of viscosity at the TPU melting point favoring the rotation of magnetic particles. This motion results from the applied magnetic field generating a torque in the particles that leads to high-frequency friction with the surrounding polymer and the additional heat dissipation. [16-18]

In analogy with Fe_3O_4 data, Fe-n and Fe-µ were fitted with Equations IV-2 and IV-3 here below

$$T(t < t_m) = T_0 + \Delta T_1(1 - e^{-t/\tau_1}) \quad \text{(IV-2)}$$

$$T(t > t_m) = T_0 + \Delta T_1(1 - e^{-t/\tau_1}) + \Delta T_2(1 - e^{-(t-t_m)/\tau_2}) \quad \text{(IV-3)}$$

where t_m is the time at which melting happens, denoting the appearance of an additional heating mechanism.

Coming back to the case of Fe_3O_4, no extra heating contribution is noted in the 10 and 15 vol.% composites in spite of reaching temperatures above the melting point $T > T_m$. This result can be interpreted based on both rheological and structural information. First, Fe_3O_4 nanobeads are more aggregated so that, free rotation is hindered when the magnetic field is flipped. Second, heating temperatures above T_m can only be reached above 10 vol.% in particles, corresponding to the apparition of a G' elastic plateau at low frequency (see Chapter III section 3.2), indicating gelation, *i.e.*, very slow motion of beads and corresponding aggregates.

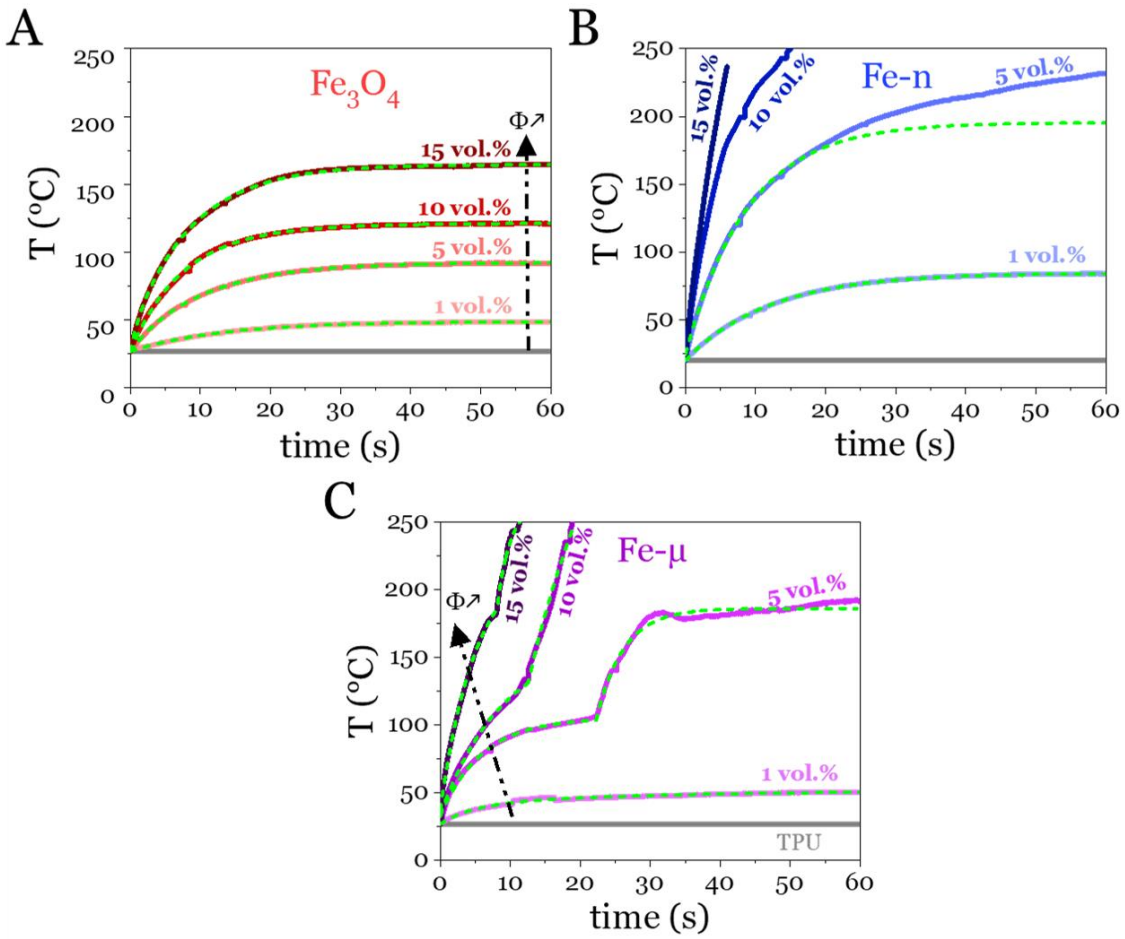

Figure 4.4: Temperature profiles as a function of time during induction heating for the three series of composites loaded with ca. 1, 5, 10 and 15 vol.% in (A) Fe_3O_4, (B) Fe-n and (C) Fe-μ respectively, the grey line stands for the neat TPU. t_{pulse}/t_{period} was fixed to 17%. Dashed lines are fitted to the data with Equation IV-1 (A-B) and with Equations IV-2 and IV-3 (C).

To confirm the direct link between the rheological behavior of a sample and its response to the alternating magnetic solicitation, we performed additional induction heating tests on the 5 vol.% Fe_3O_4 composite. It seems that increasing the pulse duration t_{pulse}/t_{period} of the magnetic field from 17% to 100% allows for the melting of the TPU to be reached (*i.e.*, for $t_{pulse}/t_{period} >$ 67%). For this composite, gelation is not reached and the material is capable to flow, allowing the motion of least aggregated nanoparticles to generate a slight extra-heating (see Figure 4.5). Note that the contribution from the extra-heating in this case is not as prominent as that of the 5 vol.% Fe-μ composite (at $t_{pulse}/t_{period} = 17\%$), due to Fe_3O_4 spherical particles being aggregated, implying lower torques values and less friction.

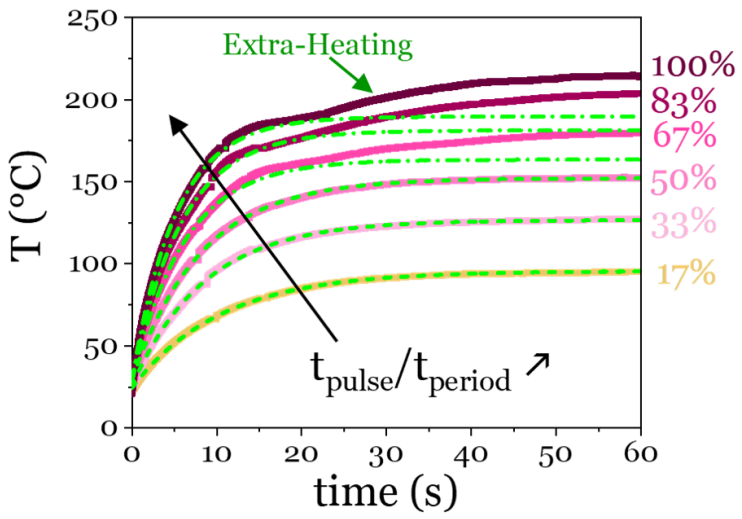

Figure 4.5: Temperature profile of a composite loaded with ca. 5 vol.% in Fe_3O_4 for increasing magnetic pulse times. The extra-heating indicates possible motion of nanoparticles above the melting of the TPU.

For the sake of comparison, we collected in Figure 4.6 all the specific absorption rates (SAR) in W g^{-1} calculated from:

$$SAR = \frac{C_p}{x_p}\frac{dT}{dt}\bigg|_{t\to 0} \qquad \text{(IV-4)}$$

where C_p and x_p are the specific heat capacity and mass fraction of fillers, determined through the DSC and the TGA measurements shown in Chapter III section 2. The specific heat capacity C_p of the samples was calculated from the DSC thermogram of the neat TPU matrix and the corresponding heat capacities of Fe and Fe_3O_4 composites.

While the SAR order of magnitude is similar for the three series of composites (30-80 W g^{-1}), Fe-n particles appear to be more efficient than Fe_3O_4 and Fe-µ ones in terms of heat generation, which is explained through a higher value of magnetic saturation and a broader hysteresis at the quasi-static frequency of the measurement. This results in a broader $M(H)$ hysteresis loop at high frequency. [19] It is further noteworthy that SAR values remain almost constant with increasing Φ regardless of the particles nature, indicating a limited impact of dipolar interactions. [4, 20-22] This is corroborated in Fe_3O_4 and Fe-n series by SAXS diffractograms showing no further aggregation of the particles with increasing Φ (see Chapter III section 1).

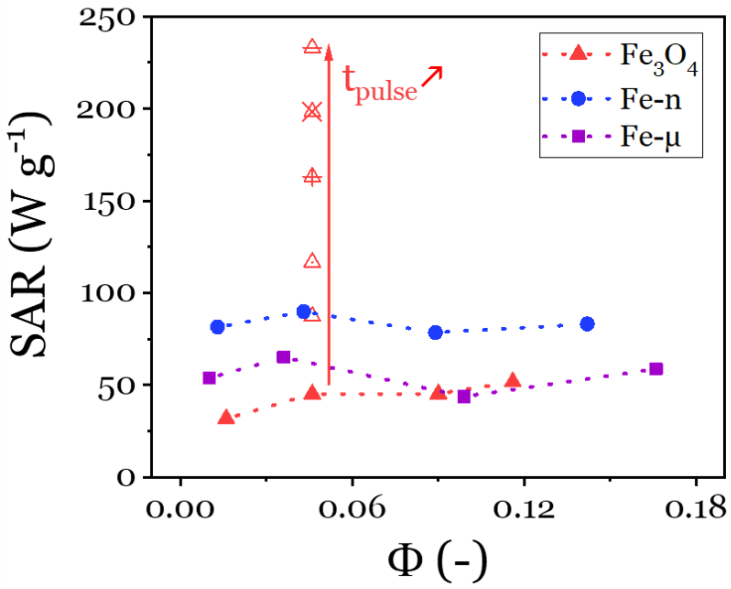

Figure 4.6: SAR as a function of the filler volume fraction for the whole set of composites. Dotted lines are guides for the eye representing the evolution of the first heating process only.

In conclusion, we have identified the mechanisms inducing heat generation for each series of composites submitted to the alternating magnetic field. Then, we have identified the possibility for an additional heating mechanism to appear during the heating process when the melting point of the matrix is reached ($T > T_m$), enabled by magnetic induced high-frequency rotation of the particles with the TPU matrix. This behavior is highly dependent on the rheology of the material and can be blocked if the viscosity is not low enough. This particular aspect will be further analyzed in chapter VI.

Besides, the thermal profiles have also enabled the selection of composites for the magnetic healing process. Composites with 5 vol.% in magnetic fillers seem to reach the desired temperature range at $t_{pulse}/t_{period} = 17\%$ while being able to flow, although 1 vol.% composites would be able to heat sufficiently if the pulse duration is increased. In contrast, composites with higher filler content (*i.e.*, 10-15 vol.%) reach the melting point too fast and gelation at high temperatures in the cases of Fe_3O_4 and Fe-n composites would hinder the healing capability. The next chapter will particularly focus on these low-filler content formulations as they appear as the best candidates to fulfill applications requirements.

References

[1] F. Kremer and A. Schönhals, Broadband dielectric spectroscopy, Springer Science & Business Media, 2002.

[2] H. R. Heydarnezhad, N. Mohammadi, A. Arbe and A. Alegria, "How Does Microstructural Design Affect the Dynamics and Rheology of Segmented Polyurethanes?," Macromolecules, vol. 53, p. 5381–5398, 2020.

[3] G. P. Baeza, J. Oberdisse, A. Alegria, M. Couty and A.-C. Genix, "A high-temperature dielectric process as a probe of large-scale silica filler structure in simplified industrial nanocomposites," Physical Chemistry Chemical Physics, vol. 17, p. 1660–1666, 2015.

[4] A. E. Deatsch and B. A. Evans, "Heating efficiency in magnetic nanoparticle hyperthermia," Journal of Magnetism and Magnetic Materials, vol. 354, p. 163–172, 2014.

[5] J. M. D. Coey, Nanoscale magnetism, Cambridge university press, 2010, p. 264–304.

[6] S. Tanwar, V. P. S. Awana, S. P. Singh and R. Pasricha, "Magnetic field dependence of blocking temperature in oleic acid functionalized iron oxide nanoparticles," Journal of superconductivity and novel magnetism, vol. 25, p. 2041–2045, 2012.

[7] O. Moscoso-Londoño, P. Tancredi, D. Muraca, P. M. Zélis, D. Coral, M. F. van Raap, U. Wolff, V. Neu, C. Damm, C. L. P. De Oliveira and others, "Different approaches to analyze the dipolar interaction effects on diluted and concentrated granular superparamagnetic systems," Journal of Magnetism and Magnetic Materials, vol. 428, p. 105–118, 2017.

[8] M. Hanzlik, C. Heunemann, E. Holtkamp-Rötzler, M. Winklhofer, N. Petersen and G. Fleissner, "Superparamagnetic Magnetite in the Upper Beak Tissue of Homing Pigeons," BioMetals, vol. 13, pp. 325-331, 1 2000.

[9] B. A. Frandsen, C. Read, J. Stevens, C. Walker, M. Christiansen, R. G. Harrison and K. Chesnel, "Superparamagnetic dynamics and blocking transition in Fe 3 O 4 nanoparticles probed by vibrating sample magnetometry and muon spin relaxation," Physical Review Materials, vol. 5, p. 054411, 2021.

[10] H. Shimoshige, Y. Nakajima, H. Kobayashi, K. Yanagisawa, Y. Nagaoka, S. Shimamura, T. Mizuki, A. Inoue and T. Maekawa, "Formation of core-shell nanoparticles composed of magnetite and samarium oxide in Magnetospirillum magneticum strain RSS-1," Plos one, vol. 12, p. e0170932, 2017.

[11] T. C. Monson, E. L. Venturini, V. Petkov, Y. Ren, J. M. Lavin and D. L. Huber, "Large enhancements of magnetic anisotropy in oxide-free iron nanoparticles," Journal of magnetism and magnetic materials, vol. 331, p. 156–161, 2013.

[12] J. M. D. Coey, Micromagnetism, domains and hysteresis, Cambridge university press, 2010, p. 231–263.

[13] A. G. Kolhatkar, A. C. Jamison, D. Litvinov, R. C. Willson and T. R. Lee, "Tuning the magnetic properties of nanoparticles," International journal of molecular sciences, vol. 14, p. 15977–16009, 2013.

[14] J. Carrey, B. Mehdaoui and M. Respaud, "Simple models for dynamic hysteresis loop calculations of magnetic single-domain nanoparticles: Application to magnetic hyperthermia optimization," Journal of Applied Physics, vol. 109, p. 083921, 2011.

[15] N. A. Usov, M. S. Nesmeyanov and V. P. Tarasov, "Magnetic vortices as efficient nano heaters in magnetic nanoparticle hyperthermia," Scientific reports, vol. 8, p. 1–9, 2018.

[16] R. Hiergeist, W. Andrä, N. Buske, R. Hergt, I. Hilger, U. Richter and W. Kaiser, "Application of magnetite ferrofluids for hyperthermia," Journal of Magnetism and Magnetic Materials, vol. 201, p. 420–422, 1999.

[17] T. Bayerl, R. Schledjewski and P. Mitschang, "Induction heating of thermoplastic materials by particulate heating promoters," Polymers and Polymer Composites, vol. 20, p. 333–342, 2012.

[18] O. Yassine, A. Zaher, E. Q. Li, A. Alfadhel, J. E. Perez, M. Kavaldzhiev, M. F. Contreras, S. T. Thoroddsen, N. M. Khashab and J. Kosel, "Highly efficient thermoresponsive nanocomposite for controlled release applications," Scientific reports, vol. 6, p. 1–7, 2016.

[19] J. M. D. Coey, Magnetic materials, Cambridge university press, 2010, p. 374–438.

[20] P. H. Linh, P. V. Thach, N. A. Tuan, N. C. Thuan, D. H. Manh, N. X. Phuc and L. V. Hong, "Magnetic fluid based on Fe3O4 nanoparticles: Preparation and hyperthermia application," in J. Phys. Conf. Ser, 2009.

[21] Y. Piñeiro-Redondo, M. Bañobre-López, I. Pardiñas-Blanco, G. Goya, M. A. López-Quintela and J. Rivas, "The influence of colloidal parameters on the specific power absorption of PAA-coated magnetite nanoparticles," Nanoscale research letters, vol. 6, p. 1–7, 2011.

[22] A. Urtizberea, E. Natividad, A. Arizaga, M. Castro and A. Mediano, "Specific absorption rates and magnetic properties of ferrofluids with interaction effects at low concentrations," The Journal of Physical Chemistry C, vol. 114, p. 4916–4922, 2010.

Chapter V: Magnetic Induced Treatment

Contents

We have identified the composites that best fit the requirements for the induction healing process. The composites with 5 vol.% in filler content present the best compromise in terms of mechanical properties while being capable of generating enough heat to reach the melting point and flow above that temperature. In this chapter, we use magnetic induction process on different composites. First, we apply the healing process to the magnetic composites previously selected and characterize their mechanical performances trough quasi-static tensile tests. Then, we demonstrate that this procedure can be expanded to other TPE-based composites. Finally, we treat the surface of 3D-printed magnetic materials, illustrating the broad range of application accessible with this technique.

1 Healing process on magnetic composites

Keeping in mind the selection of composites based on their thermomechanical behavior (*i.e.*, high elongation at failure under tensile solicitation and capacity to flow on a short time scale) as well as their capacity to reach the desired temperature range in a few tens of seconds under magnetic stimulus (see conclusions of Chapters III and IV), composites loaded with *ca.* 5 vol.% of fillers underwent the healing process (see Figure 5.1A). Tensile dumbbell samples were cut in two halves with a razor blade and reassembled in a mold with the middle section being repaired by the healing process (see Figure 5.1B).

Uniaxial tensile tests were performed on the composites loaded with 5 vol.% in Fe_3O_4, Fe-n and Fe-µ magnetic fillers (see Figure 5.2). "*Reshaped*" refers to samples hot-pressed from post-mortem pieces of materials issued from "*Original*" tests presented in Chapter IV section 3.1. On the other hand, "*Healed I*" refers to reshaped samples that have been cut in two halves and subsequently healed locally through thermal magnetic induction (see Figure 5.1B). For each type of sample, a minimum of three tensile tests were performed (see Appendix C for all *Reshaped* and *Healed I* data). The targeted healing temperature was 195 °C ± 15 °C to promote fast chain diffusion without significant polymer degradation. Accordingly, induction heating was adapted for each type of particles through t_{pulse}/t_{period} (from 17% to 67%) and healing time (45 s or 60 s).

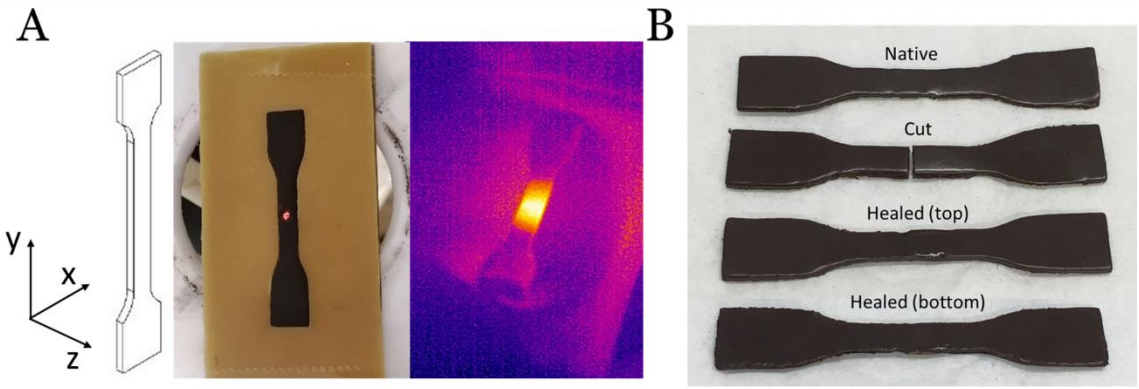

Figure 5.1: (A) Schematic representation of a dumbbell tensile sample. Photograph of the setup during the healing process. Thermal imaging indicating the zone of the sample affected by the induction heating. (B) Photograph of a sample at different stages of the healing procedure (native, cut and healed).

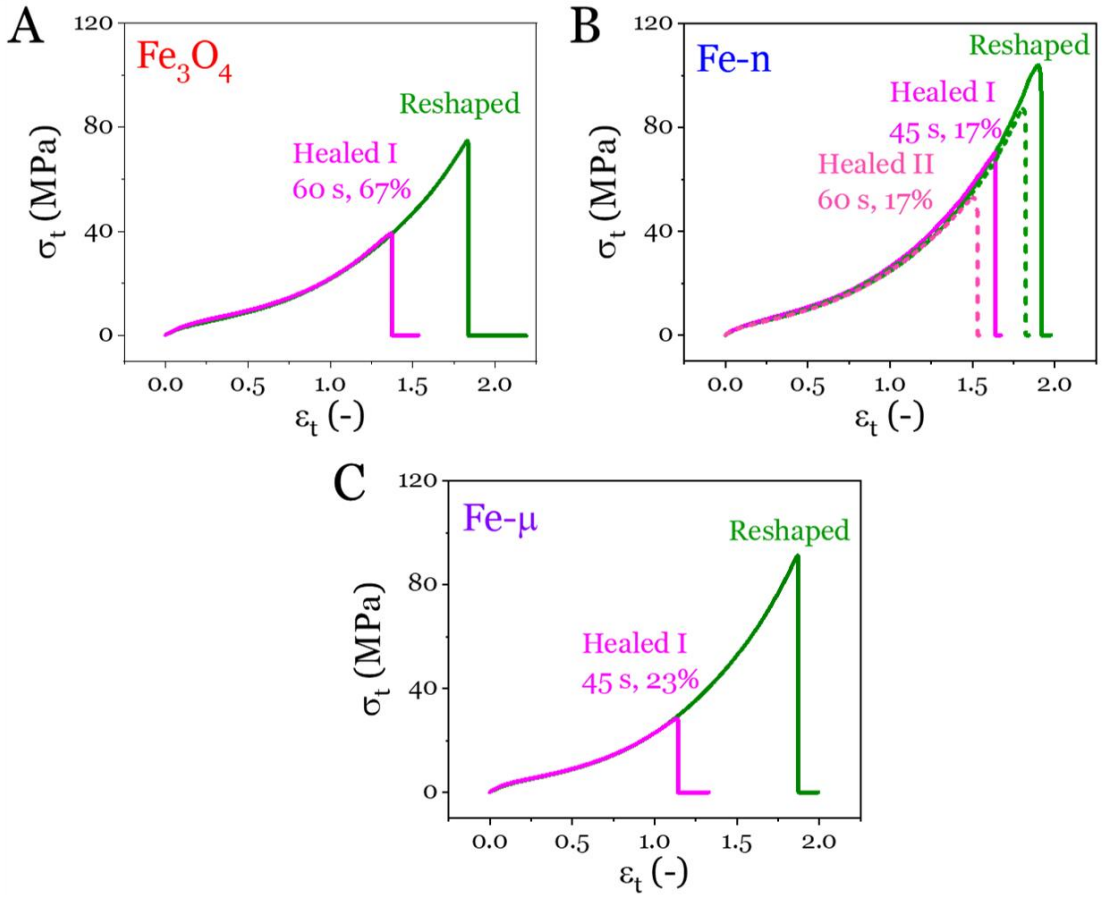

Figure 5.2: Tensile tests performed on series of nanocomposites loaded with ca. 5 vol.% in (A) Fe_3O_4, (B) Fe-n and (C) Fe-μ. See text for "Original", "Reshaped", "Healed I" and "Healed II" mentions. Heating duration and t_{pulse}/t_{period} were adapted according to the particle's heating profile. Dotted lines correspond the tensile tests of Reshaped and Healed II composites that underwent a drying step.

Strikingly, the stress-strain response of the healed materials systematically overlaps with the *Reshaped* samples up to above 1.2 true strain unit, far above the standard use of common TPU based goods. This is further emphasized in Figure 5.3 where *Original*, *Reshaped* and *Healed I* samples exhibit almost identical tensile behaviors, regardless of the particles' nature. Distinct behaviors are exclusively observed at very high strain where *Healed I* samples systematically show a lower strain at fracture than their *Reshaped* counterparts. This effect is assigned to a different microstructure around the healed zone. We believe that this is caused by the persisting phase separation within the liquid TPU. In fact, this lack of dissociation during healing acts against the memory erasure, limiting the recovery of the TPU structure once cooled down.

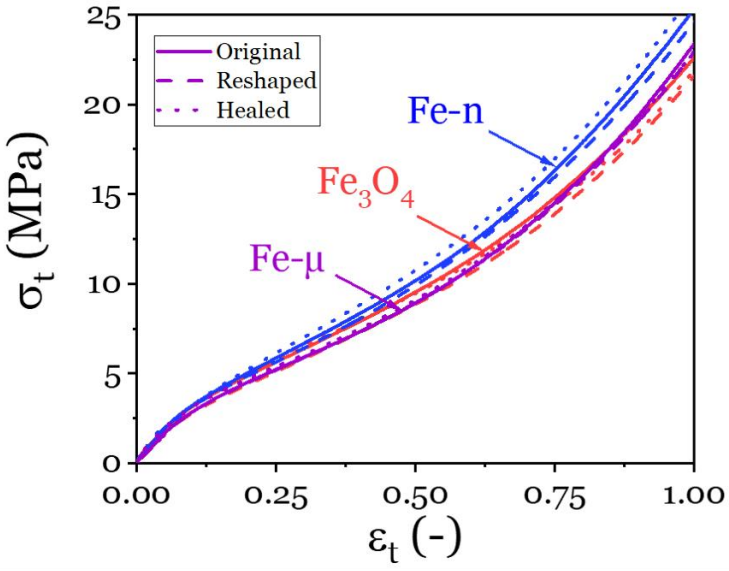

Figure 5.3: Zoom-in on tensile curves at low and moderate strain for the three series of composites, compared to the Original tensile curves presented in Chapter III section 3.1. These results systematically emphasize the quality of the healing

We performed X-ray tomography on a 5 vol.% Fe-n composite before and after the magnetic induced healing process (see Figure 5.4A and 5.4B respectively) to track the potential formation of defects during the healing procedure. Although samples looked similar at the macroscopic scale, X-ray tomography revealed the presence of large holes in *Healed I* materials, holes formed during the healing process possibly owing to evaporation of residual water in the TPU (see Figure 5.4B). Indeed, no hole was detected in mended composites when the samples were vacuum-dried before healing (see Figure 5.4C) showing complete structural recovery of the sample (hereby referred as "*Healed II*" sample). It should be noted that similar mechanical recovery was observed for hole-containing and hole-free composites after healing (see *Healed*

I and *Healed II* tensile tests in Figure 5.2B), where the elongation at break corresponds to *ca.* 85% of the *Reshaped* one. This is explained by the large size of the critical defect admissible in relatively soft rubber-based materials. Although such samples treatment (*i.e.*, vacuum drying) does not appear as crucial for tensile tests, the presence of holes may significantly impact the resistance to fatigue. Vacuum-drying seems therefore recommended before healing.

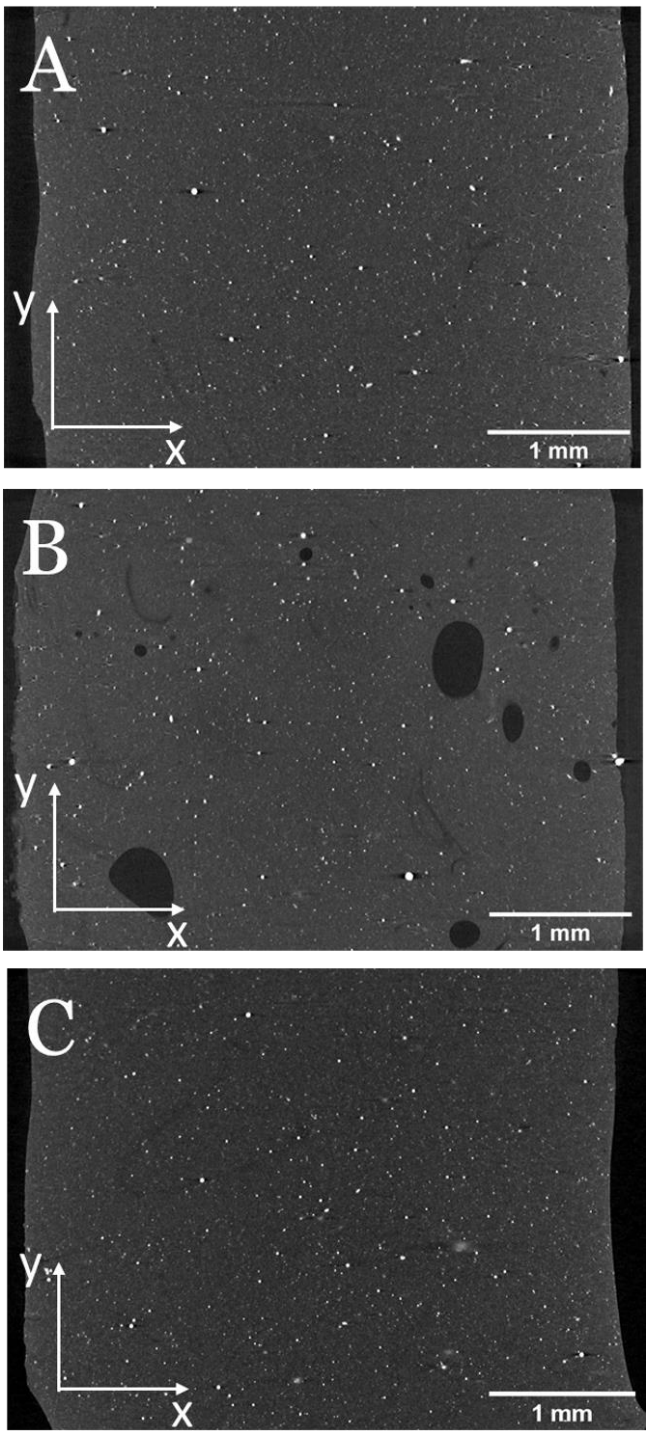

Figure 5.4: X-ray Tomography imaging performed at the mid-thickness of the samples, on the center of (A) Reshaped, (B) Healed I and (C) Healed II" ca. 5 vol.% Fe-n dumbbell samples.

Beyond the high level of mechanical recovery, determined through the strain at break, another asset of our procedure is that it is extremely fast (*i.e.*, 1 minute or less) and applicable to relatively hard polymer materials, making an importance difference with the common self-healing mechanisms (see Figure 5.5 adapted from ref. [1]). Strikingly, while we need 45-60 s to heal our materials (30-100 MPa) to 85%, the pioneer work of Cordier *et al.* on self-healable supramolecular materials demonstrated 85% recovery of the tensile properties after 180 minutes. [2] Certainly, the price to pay resides in the magnetic stimulus, yet being unavoidable to reach outstanding healing efficiency on "structural polymers".

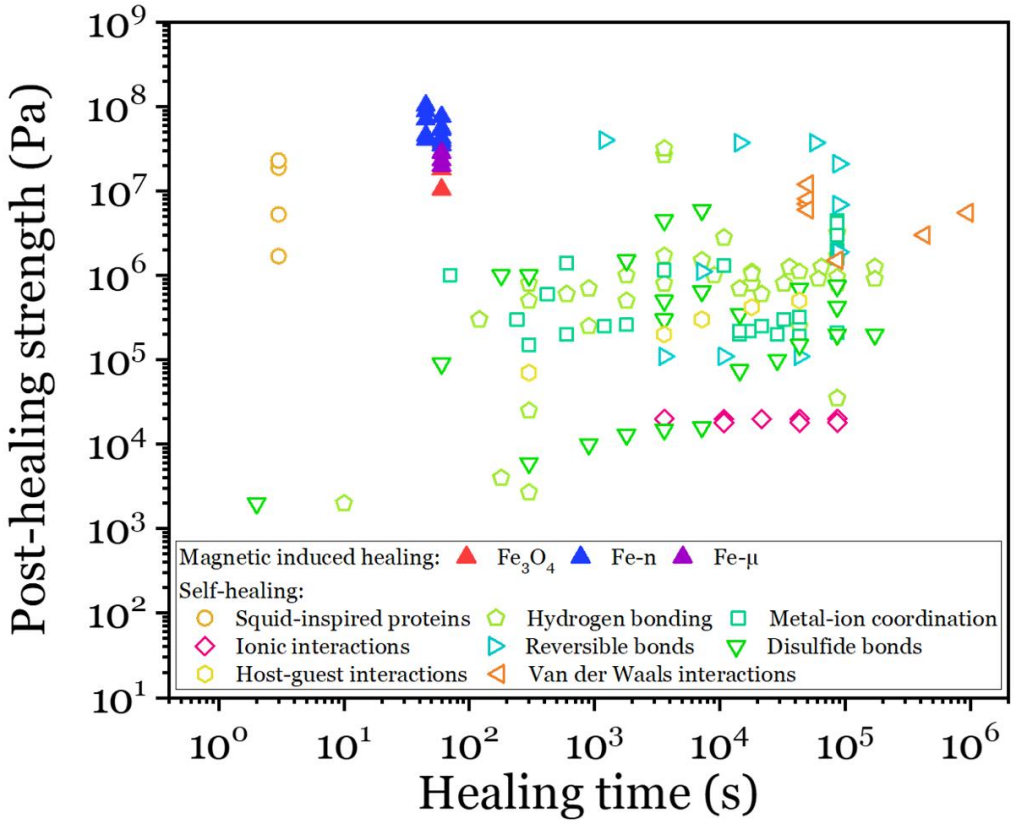

Figure 5.5: Performance of magnetic induced healing materials (this study) compared to self-healing materials, adapted from [1]. The performance of the different self-healing techniques is displayed with open patterns, while the results from magnetic induction healing are shown with full patterns.

Lastly, it is worth pointing out that Fe_3O_4 and Fe-μ based materials have slightly lower strain at failure (*Reshaped*) and are less healable (*Healed*) than their Fe-n-based counterparts (see Figure 5.2). As suggested from DSC thermograms, we believe that lower elongations at break are due to weaker interactions between the polymer chains and the particles, and lower crystallinity.

2 Healing process on an alternative TPE matrix: PBT/PTHF

To illustrate the versatility of the magnetic induced healing process, we have chosen to apply it on an alternative TPE filled with identical Fe-n responsive magnetic particles. For this experiment, we chose a commercial multiblock copolymer made of poly(butylene terephthalate) (PBT) and polytetrahydrofuran (PTHF) segments, for its structural and mechanical similarity to the commercial TPU used in the present study. This multiblock copolymer, containing 30 wt.% in PBT hard segments, is hereafter labeled as HS30 (see Figure 5.6).

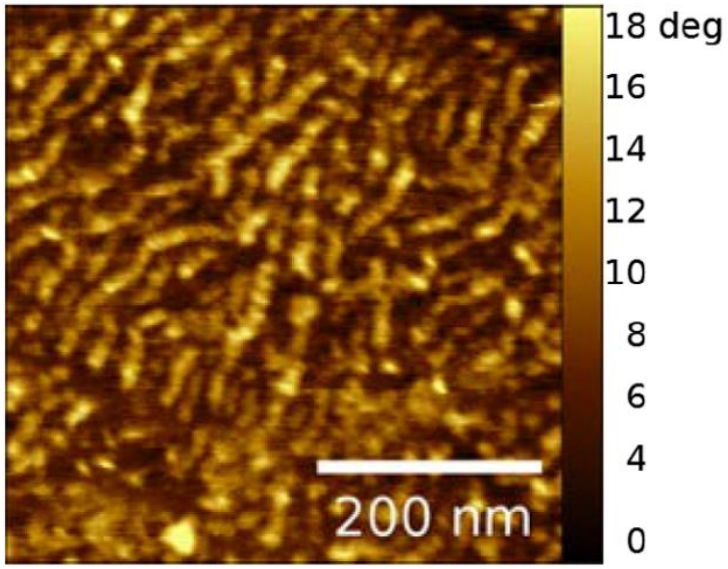

Figure 5.6: AFM micrograph of a hot-pressed HS30 sample (top view), adapted from [3].

Dumbbell-shaped samples made of HS30 filled with 5 vol.% Fe-n were prepared through extrusion and subsequent hot-pressing at 200 °C. Three samples were completely cut in their center, dried and then healed at different t_{pulse} / t_{period} ratios targeting a desired temperature of 200 ± 10 °C (see Figure 5.7A). Similarly to the temperature profiles of TPU (Desmopan 85085A) based composites shown the previous chapter, an additional heating contribution appears at *ca.* 150 °C, that is when the HS30/Fe-n composites start to melt, further confirming our global interpretation in terms of particles motion.

Tensile tests were then performed on healed and native composites used as references (see Figure 5.7B). These initial tests, which have not been optimized in terms of healing time,

t_{pulse} / t_{period} ratios nor setup configuration, already show a *ca.* 60% recovery in elongation at break, confirming that this material could also be successfully repaired. The insert shows identical behavior at low strain amplitude, which is the relevant region for targeted applications.

Our methodology can therefore be applied regardless of the nature of the magnetic filler and of the TPE, although the importance of the full multi-physics characterization must be emphasized as it ensures a reliable understanding of the mechanisms taking place in the material, serving to optimize the healing procedure.

Interestingly, it can also be noted that the heating rate increases if multiple induction heating cycles are performed at the same t_{pulse} / t_{period}, under the condition that the melting point is reached. For example, the HS30 based composite was subjected to two consecutive heating cycles with a cooling intermediate step at room temperature (see Figure 5.7C), leading to an increase in the value of SAR, being 45 and 75 W g^{-1} for the first and second step respectively. Possible movement of particles in the molten material might have reorganized in different arrangements of particles, impacting favorably their response to the alternating magnetic field and therefore their heat generation. [4] Multiple healing steps will thus change the temperature profiles, which must be taken into account to perform reliable healing processes. Consecutive induction heating steps do not affect the material's capacity to be repaired through healing, as the magnetic composite will still reach the temperature required (*i.e.*, its melting point).

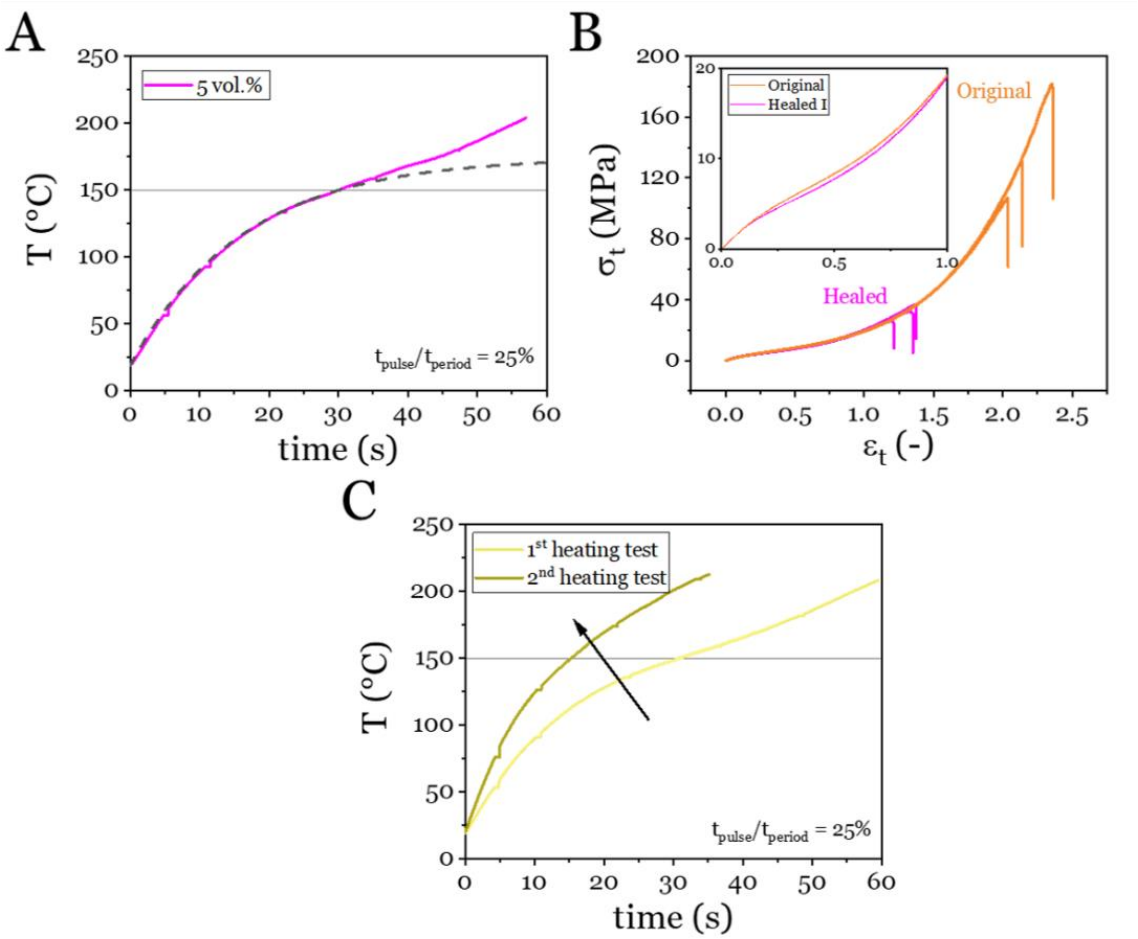

Figure 5.7: (A) Temperature profiles corresponding to the healing of a HS30 TPE loaded with 5 vol.% Fe-n particles. The pulse duration t_{pulse} / t_{period} was set to 25 %. (B) Tensile tests performed on Original and Healed I composites loaded with 5 vol.% Fe-n particles. Insert corresponds to a zoom-in at strains below 1. (C) Temperature profiles of two consecutive magnetic heating tests performed on the HS30 composite loaded with 5 vol.% Fe-n particles with the same pulse duration t_{pulse} / t_{period} = 25 %.

3 Induction heating applied on 3D-printed objects

In this section, we present an additional opportunity offered by our technology regarding the post-treatment of objects produced through fused filament deposition. These 3D-printed objects present topographic defects, that are sometimes smoothened through solvent vapor treatments (*e.g.*, post-processing acetone vapor polishing). [5] Here, the solid-to-liquid phase transition triggered by the magnetic field enables the melting of the surface, with the viscosity and the surface tension of the resulting liquid driving the surface quality. The contactless nature, the rapidity, the limited penetration of the magnetic field indicates that our technique can be applied to the surface of a 3D-printed object while maintaining its internal structure intact. Furthermore,

the possibility to use co-deposition to tailor the location of the nanoparticles is a strong asset in view of a possible upscaling at the industrial level.

Objects, such as dumbbells and pyramids, were produced through fused filament fabrication using a Tobeca T333 device (Tobeca, France). The machine was also equipped with a Tobeca pellets extruder replacing the filament-based feeding of the printing tip with a chamber intended to hold the pellets (see Figure 5.8A). Note that this device requires sufficiently small pellet-like pieces for a regular flow (see Figure 5.8B). Additionally, this eliminates the need for an additional step for the production of a filament.

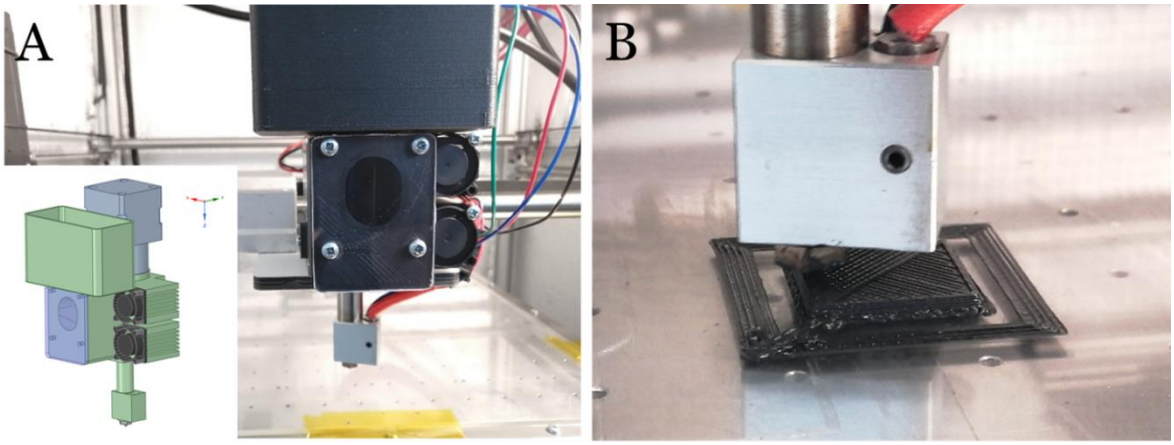

Figure 5.8: (A) 3D printer equipped with a chamber designed to feed pellets/granules to the 3D-printer. (B) Printing of a pyramid based on the 5 vol.% Fe-n composite.

One series of TPU-based composites filled with Fe-n nanoparticles were produced through extrusion. Then their filler fraction was confirmed through TGA (see Figure 5.9). The composites were processed in small pellet-like pieces (*i.e.*, 3-4 mm in length) to fit inside the melting chamber. Then, thermal characterization of such composites through DSC was performed verifying their characteristic temperatures, proving once again the complete melting of the material above 160 °C (see Figure 5.10A). This series of thermograms are in agreement with those performed on previously introduced hot-pressed Fe-n composites (see Chapter III section 2.2). The rheological characterization through frequency sweeps at 180 °C shows the proper behavior which would ensure the required flow of the material for both the deposition through 3D-printing and the post-processing treatment of the surface (see Figure 5.10B).

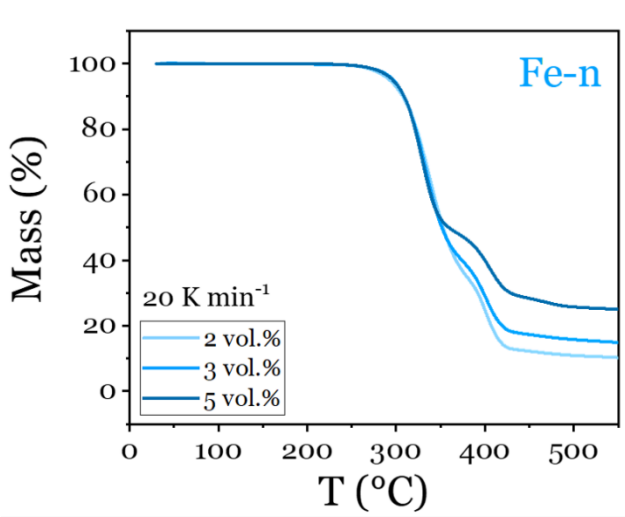

Nominal fraction	TGA Fe-n
2 vol.%	2.0 vol.%
3 vol.%	2.8 vol.%
5 vol.%	4.7 vol.%

Figure 5.9: Thermogravimetric analysis performed on composites filled with Fe-n nanoparticles. Nominal and actual volume filler fractions are shown in the table.

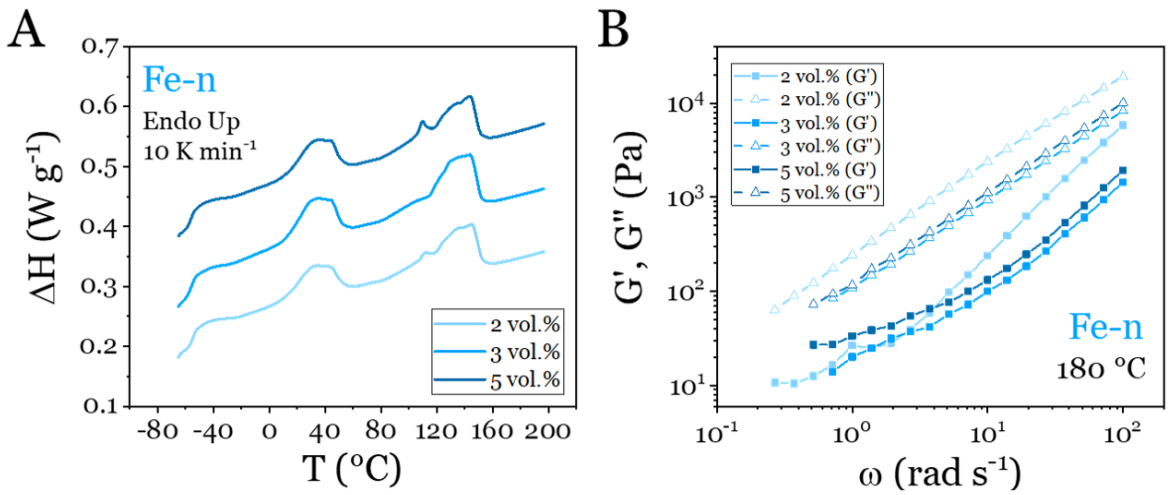

Figure 5.10: (A) DSC thermograms series measured for the series of Fe-n composites. The heat flux is normalized by the TPU mass. Data are shifted vertically for clarity, with 2 vol.% composite taken as the reference. (B) Rheological frequency sweep measurements measured at 180°C for the Fe-n composites. Full and open symbols correspond to the storage modulus G' and the loss modulus G" respectively.

For the sake of heat generation, the formulation chosen for the final pieces consists of the Desmopan 85085A TPU matrix reinforced with 5 vol.% in Fe-n nanoparticles. Firstly, we produced 2 cm x 2 cm and 4 cm x 4 cm square based pyramids optimizing the printing parameters. The temperature of the nozzle and the printing stage were set to 210 °C and 50 °C respectively and the printing rate was set to 50 mm s^{-1} for optimal results.

To illustrate the potential of this approach, we first manually applied the magnetic field on a lateral face of a truncated pyramid (see Figure 5.11) made of TPU based Fe-n composites. While the surface imperfections related to the manufacturing process (*i.e.*, due to the filament deposition) are well visible on the left-hand side, a much smoother surface is obtained after only a few seconds of irradiation (right hand-side). The top surface is displayed to show the internal architecture and to prove that no particular change occurred within the object during treatment. While the surface treatment was performed by hand, this proof-of-concept is intended to show that this procedure could be automated using a robotic arm and improved using a coil conceived for the specific geometry of each different piece.

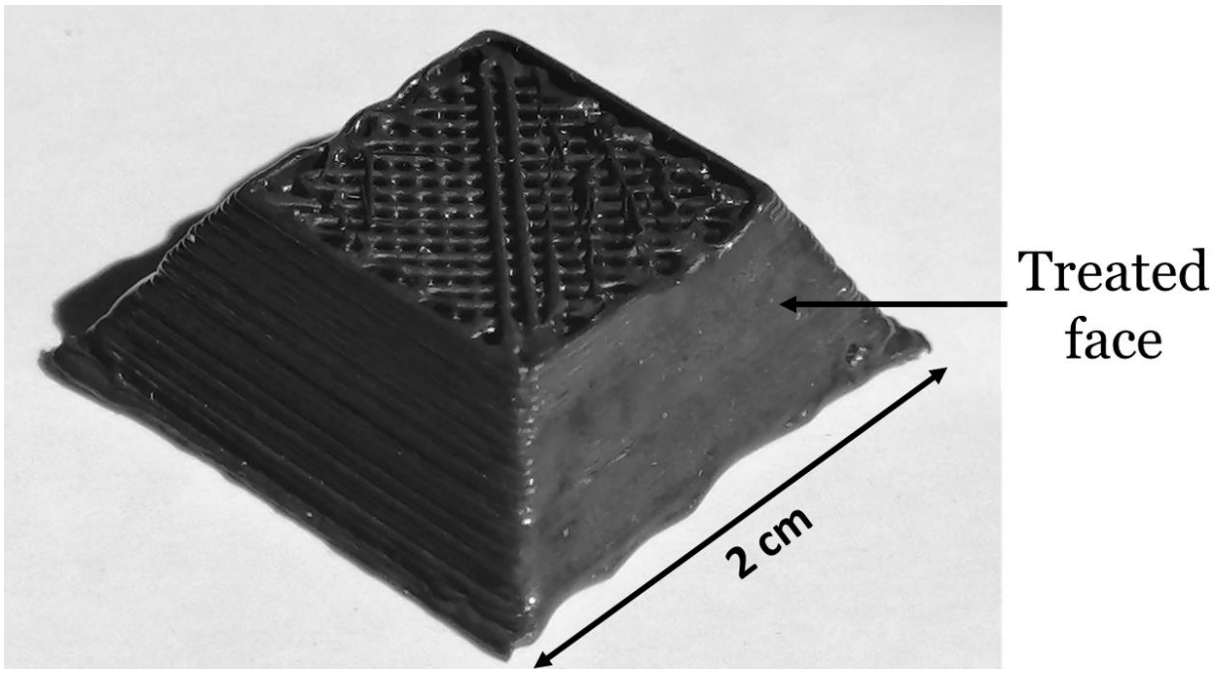

Figure 5.11: Impact of the smoothening procedure on the topography of a truncated pyramid with untreated (left) and treated (right) faces.

We repeated this procedure in Figure 5.12, where we treated a porous dumbbell-shaped sample. Note that the untreated sample (see Figure 5.12A-B) clearly illustrates the presence of defects on the surface. Here again, after a few seconds the matter is densified resulting in a much shinier surface, demonstrating the possibility to reach an “injected look” within a short time (see Figure 5.12C-D).

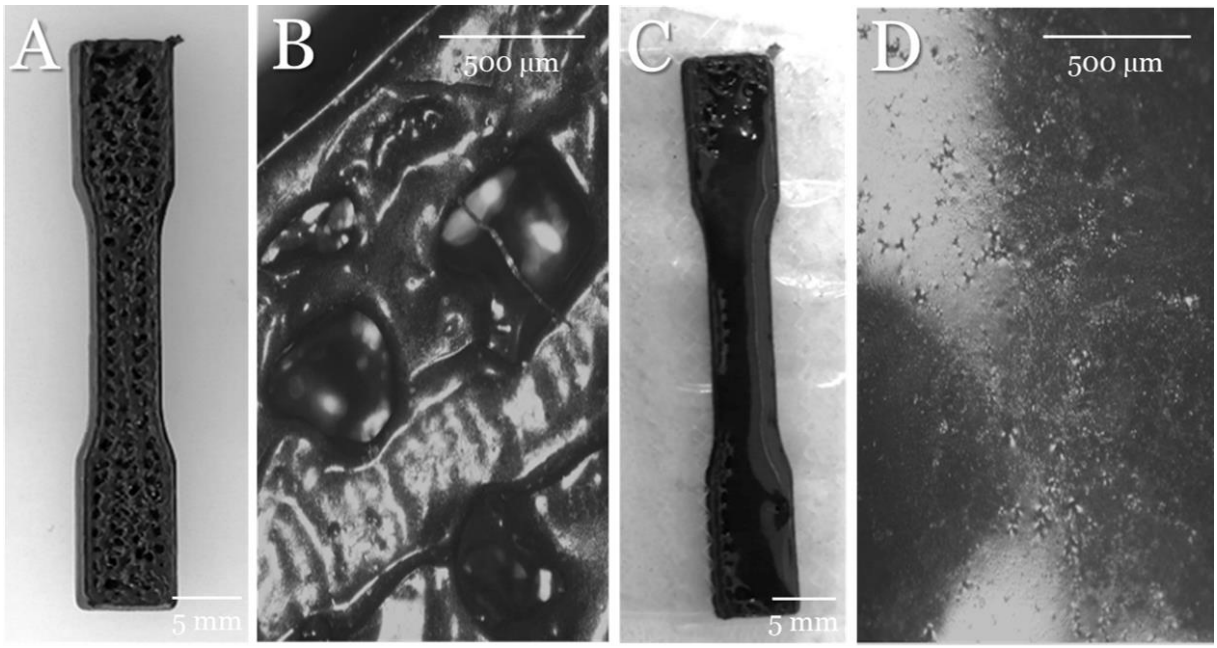

Figure 5.12: Impact of the smoothening procedure on the topography of a 3D-printed dumbbell-shaped sample. (A) Untreated 3D-printed sample and (B) its corresponding optical micrograph. (C) Treated sample and (D) its corresponding optical micrograph.

In conclusion, we performed the magnetic induction healing process on selected composites (loaded with 5 vol.% in magnetic particles) ensuring proper thermomechanical characteristics and induction heating response required for repairing. We have characterized the mechanical response of such samples and shown satisfactory recovery of the mechanical properties. The versatility of this technique has been proven as it can be successfully applied to a range of TPE composites filled with magnetic particles with different dimensions and chemistry, precisely tuning the induction heating parameters to fit with the material's solid-to-liquid phase transition. The surface treatment of a magnetic composite, loaded with 5 vol.% in Fe-n nanoparticles, has been tested, showing a clear improvement of the surface while avoiding any effect on the internal structure of the object. Optimizing this procedure is certainly one of the major perspectives of this work, strongly related to possible industrial applications. (Note that a patent has been submitted in December 2020 and is in revision at the time of writing).

References

[1] A. Pena-Francesch, H. Jung, M. C. Demirel and M. Sitti, "Biosynthetic self-healing materials for soft machines," Nature Materials, vol. 19, p. 1230–1235, 2020.

[2] P. Cordier, F. Tournilhac, C. Soulié-Ziakovic and L. Leibler, "Self-healing and thermoreversible rubber from supramolecular assembly," Nature, vol. 451, p. 977–980, 2008.

[3] M. Nébouy, A. de Almeida, S. Brottet and G. P. Baeza, "Process-oriented structure tuning of PBT/PTHF thermoplastic elastomers," Macromolecules, vol. 51, p. 6291–6302, 2018.

[4] E. C. Abenojar, S. Wickramasinghe, J. Bas-Concepcion and A. C. S. Samia, "Structural effects on the magnetic hyperthermia properties of iron oxide nanoparticles," Progress in Natural Science: Materials International, vol. 26, p. 440–448, 2016.

[5] C. Neff, M. Trapuzzano and N. B. Crane, "Impact of vapor polishing on surface roughness and mechanical properties for 3D printed ABS," in 2016 International Solid Freeform Fabrication Symposium, 2016.

Chapter VI: Nanoparticles Movement during Induction Heating

Contents

In Chapters IV and V, we introduced the idea of an additional heating mechanism appearing during the magnetic induction process, being triggered by the drop of viscosity of the host polymer. In this case, magnetic nanoparticles submitted to the oscillatory magnetic field may become mobile, first resulting into high-frequency rotation leading to mechanical friction, and second, to translation being at the origin of the emergence of dipolar chains (see below). While the rotation of spherical particles on themselves does not generate any structural modification of the composites, making this phenomenon hardly quantifiable, [1] the translation is expected to play a major role on their spatial distribution. In this chapter, we thus focus on the characterization of the translational motion of nanoparticles that we use to rationalize the corresponding extra-heating process. Our experiments consist of using ultra small-angle X-ray scattering (USAXS) and X-ray photon correlation spectroscopy (XPCS), performed in-situ during induction heating, together with a follow-up of the temperature through thermal imaging. These experiments have been conducted on the ID02 beamline at ESRF Grenoble in 2021.

Here again we have made the choice of investigating the 5 vol.% Fe-n composite, whose temperature profile has shown the additional friction-induced heating mechanism strongly suggesting particles motion. First, the structural changes of the sample are confirmed through time-resolved USAXS and Focused Ion Beam - Scanning Electron Microscope (FIB-SEM) in parallel with its corresponding temperature profile. Then, X-ray photon correlation spectroscopy (XPCS) basics are presented prior to the characterization of the sample subjected to the magnetic field over a long period of time.

1 Electron microscopy and time resolved USAXS

The significant extra-heat generation detected in Fe-n and Fe-μ composites (see Figure 4.4) at the TPE melting strongly suggested the possibility for the nanoparticles to move under the application of the oscillatory magnetic field. In contrast, low filler content Fe_3O_4 composites (see Figure 4.5), subjected to a magnetic field with $t_{pulse}/t_{period} \geq 67\%$, suggested a limited extra-heating contribution through the motion of its pre-aggregated particles.

We use FIB-SEM to illustrate the change in particle arrangement in Fe-n composites before and after 1 min magnetic induction heating. To characterize them through FIB-SEM, samples, previously metallized with gold, required a two-step milling procedure on the bulk nanocomposite to analyze a section perpendicular to the surface of sample. This procedure uses

high and fine current beams (4 nA and 80 pA respectively) to analyze a polished surface using a backscattered electron (BSE) detector.

FIB-SEM is used on the cross-section of a dumbbell-shaped composite containing *ca.* 5 vol.% in Fe-n (see Figure 6.1A for a micrograph performed prior to induction heating). In this micrograph, there is no visible arrangement nor alignment of particles in any direction. Then, a cross-section of a healed 5 vol.% Fe-n composite displays a clear alignment of particles (see Figure 6.1B for a micrograph exposed to 1 min of induction heating). High-frequency magnetic field enables the particles diffusion, resulting into the creation of dipolar chains likely to impact the heating efficiency and the mechanics of materials healed several times. This is emphasized by the fact that the healed sample was subjected to the alternating magnetic field for 1 min following the corresponding temperature profile in Figure 4.4B, showing that a plateau is not reached during the experiment, meaning that the structure is still evolving at this point.

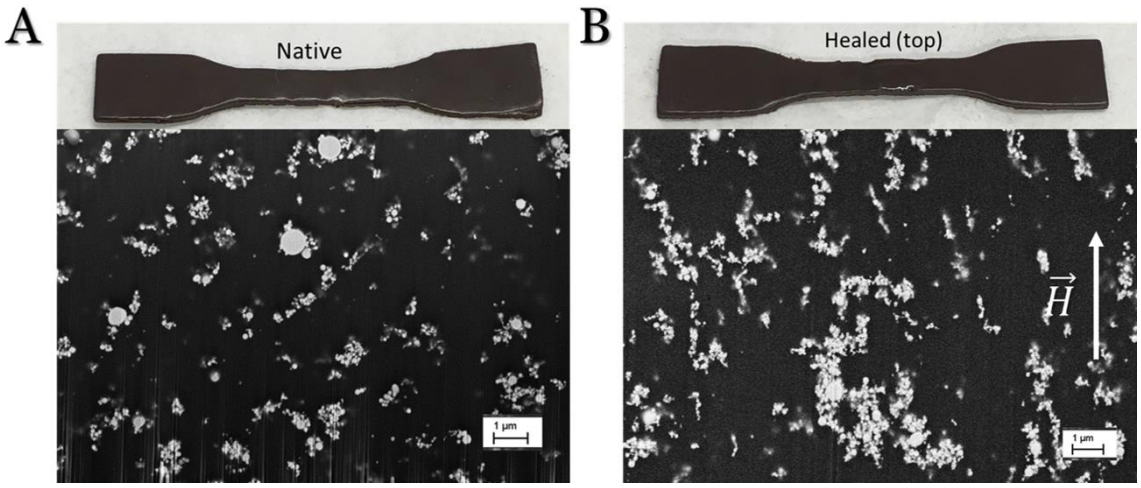

Figure 6.1: Photographs and FIB-SEM micrographs (section perpendicular to the top surface of the dumbbell-shaped) from a composite containing ca. 5 vol.% Fe-n, (A) before and (B) after 1 min of healing.

To deepen our understanding on particle motion, time-resolved USAXS experiments were performed on a sample subjected to the alternating magnetic field at $t_{pulse}/t_{period} = 63\%$ over a long duration (*i.e.*, 20 minutes) to reach a steady-state structure.

The set-up for this experiment consists of coupling the two-turn coil configuration of the magnetic inductor and the infrared camera with the ESRF ID02 beamline. Disk-shaped samples (0.5 mm in thickness and 4 mm in diameter) are suspended at the center of the coil within a Teflon fiber composite strip using Kapton tapes, keeping all metallic objects at a safe distance

from the coil (see Figure 6.2). The sample is suspended slightly above the coil to prevent any obstruction of the X-ray beam. As the magnetic sample is placed vertically at the center of the coil, magnetic field lines traversing the material are approximately vertical (see Figure 6.2A). The thermal measurement of the samples is ensured with the same IR camera as the previous induction heating experiments.

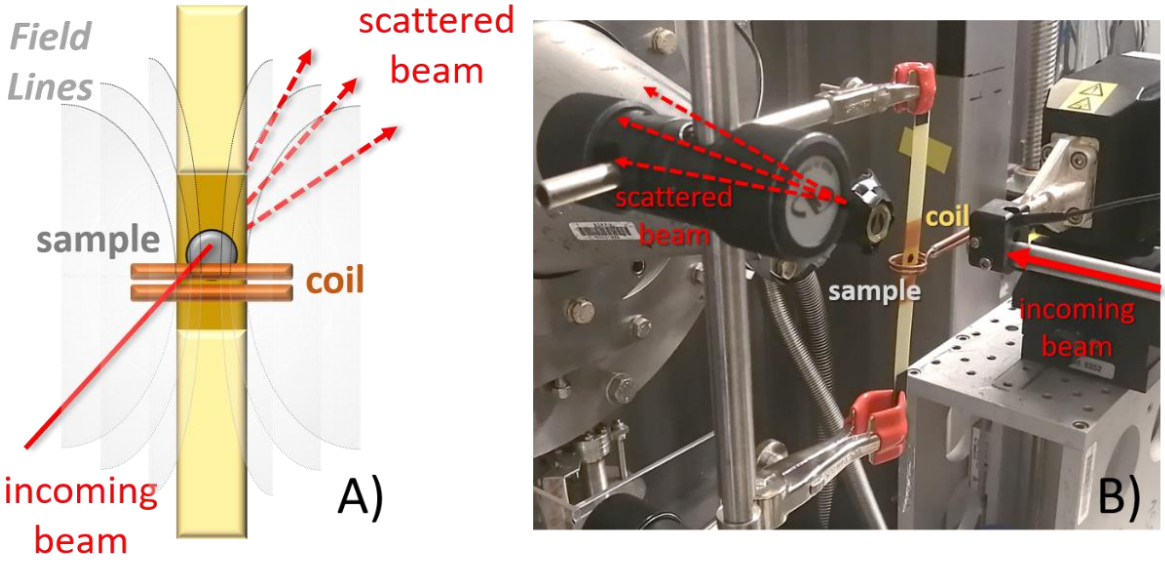

Figure 6.2: Experiment set-up (A) Schematic representation illustrating the sample in regards to the magnetic field lines generated by the two-turn coil and the X-ray beam. (B) Photograph of the set-up on the ID02 beamline.

Time-resolved USAXS were performed in a pinhole ultra-small-angle X-ray scattering geometry at an X-ray wavelength λ of 0.995 Å and a sample to detector distance of 30.7 m, allowing for measurements down to the μm^{-1} q range. The 2D X-ray speckle patterns were recorded with an Eiger 500K detector. USAXS spectra were acquired every 30 seconds starting immediately before the activation of the magnetic field and for the total duration of the experiment (*i.e.*, 20 minutes). Qualitatively, there is a change in the structure resulting from the comparison of speckle shape distribution in the 2D patterns. The first speckle acquisition made before the activation of the magnetic field shows an isotropic distribution of intensity speckles in its 2D pattern (see Figure 6.3A), whereas the speckle image acquired at 19 min shows an anisotropic speckle distribution in the 2D pattern (see Figure 6.3B). The scattering intensity recorded prior to the experiment (see Figure 6.3C) shows the same intensity decay along the horizontal and vertical direction with a dependence in $q^{-2.7}$. The intensity decay becomes anisotropic for long times with a dependence in q^{-3} for the horizontal direction and in $q^{-2.5}$ for

the vertical one, indicative of a preferential alignment of particles occurring over the duration of the experiment.

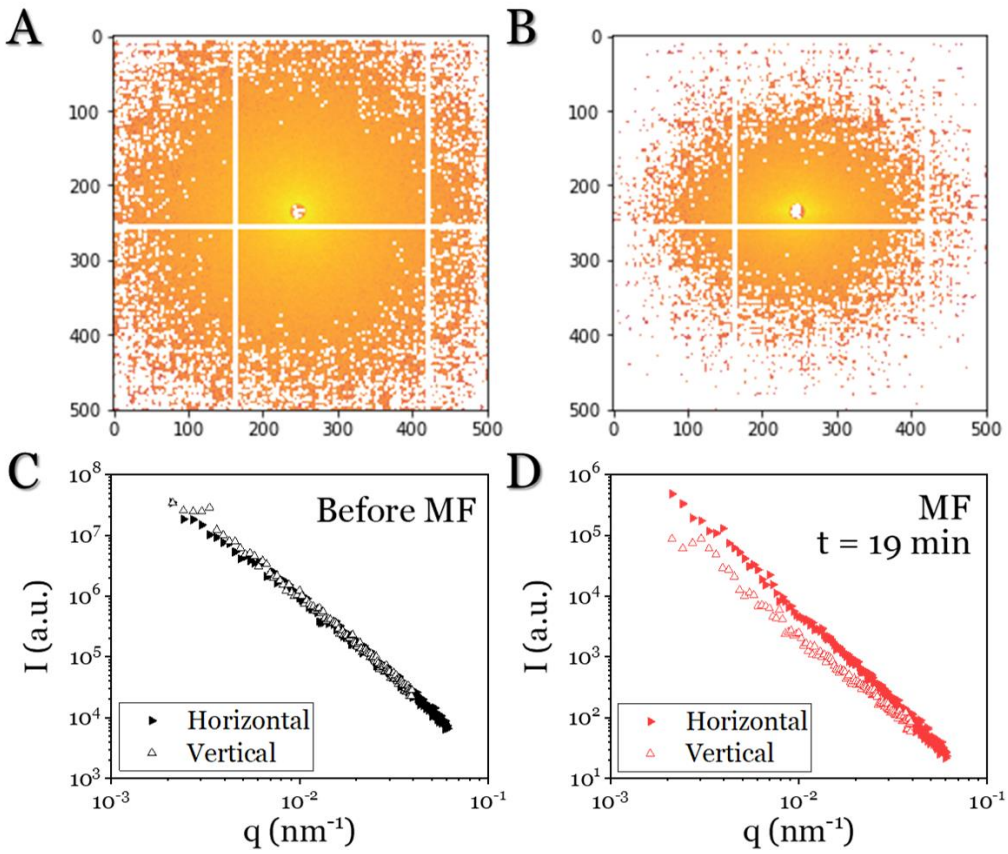

Figure 6.3: Evidence for particles alignment. (A-B) 2D X-ray scattering patterns measured immediately before the magnetic solicitation and after 19 minutes of heating ($T > 180$ °C in both cases) respectively. (C-D) Corresponding scattering intensity integrated over horizontal and vertical directions of the 2D detector (angle ±5°).

Interestingly, the derivative of the USAXS intensity signal $d\log(I(q))/d\log(q)$, over the full duration experiment and using the full range of q (*i.e.*, $2{\cdot}10^{-3}$ to $6{\cdot}10^{-2}$ nm^{-1}) gives us a higher insight into the evolution of the structure with time (see Figure 6.4A). During the magnetic induced heating, the initial change of the derivative along the vertical and the horizontal directions and points out a different behavior of the sample along the two directions, with a preferential alignment of the particles in the vertical direction (*i.e.*, parallel to the magnetic field lines). Afterwards, at 3 min 20 s, the slope remains constant indicating that the overall structure of the sample is stable in time even if it is not fixed as there are still limited particle movements at the nanoscale.

Strikingly, if we focus on the temperature profile of the same experiment (see Figure 6.4B), we observe a 210°C peak at the same time where the scattering intensity derivative signal becomes stable. After this peak, the temperature slightly decreases until it reaches a 187°C plateau for the rest of the experiment. This behavior tells us that the contribution of the particle movements to heat generation reduces once the sample structure has reached his new equilibrium state under magnetic field, thus explaining the lower temperature found at plateau. In addition, we can infer that, after the initial transient phase, the stable heat generation is mainly due to magnetic hysteresis losses with particle friction playing a reduced role, which confirms the stability of the overall structure.

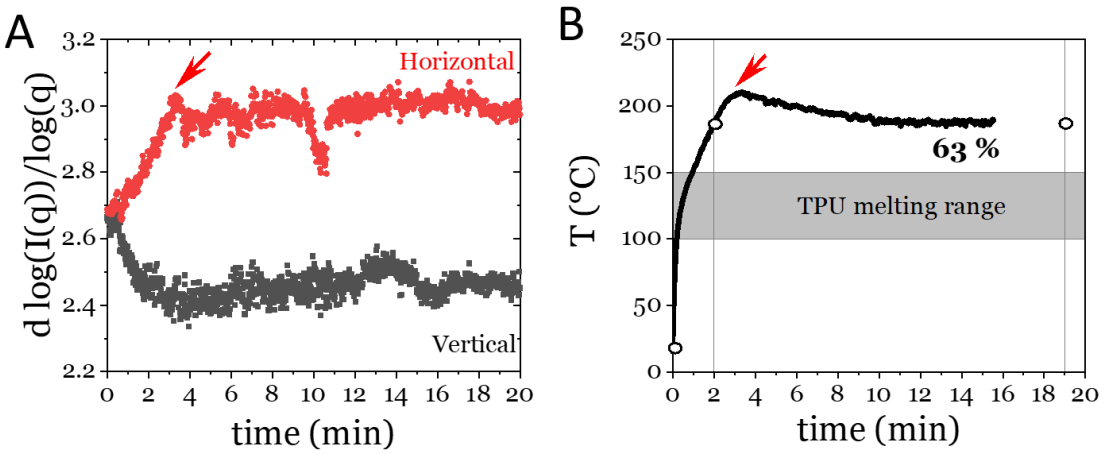

Figure 6.4: Correlation between structural anisotropy and heating kinetics upon induction heating. (A) Absolute value of the SAXS signal derivative in log-log scale $d\,log(I(q))/d\,log(q)$ *for* $0.0065 < q < 0.0215$ *nm*$^{-1}$ *as a function of time for both horizontal and vertical integration directions. (B) Sample temperature measured from IR-camera as a function of time. The grey zone represents the TPU melting range as measured by DSC. The inductor is set to* $t_{pulse}/t_{period} = 63\%$*. Arrows indicate the time at which the temperature reaches its maximum value,* $t = 3$ *min 20 sec. White dots indicate the XPCS measurements after 2 and 19 min, both satisfying* $T = 186 \pm 1$ *°C.*

To summarize, there seems to be two important steps during this induction heating experiment. At the start of the experiment, the temperature follows the typical monomodal exponential curve expected from induction heating of a system at solid state. Then, at the melting point (reached at ~20 s), friction-induced heating appears as an additional heating mechanism enabled by the sudden drop in viscosity, allowing for more heat to be generated. Driven by the magnetic field, the system structure evolves through the motion of particles within the matrix, eventually leading to the formation of vertical dipolar chains. [2] The movement of magnetic particles occurs up to the point where a new dynamic equilibrium (at ~3 min 20 s) is found, with the

dipolar chains limiting the particles mobility. At this point, the overall structure under magnetic field has become stable.

In the next section, we will investigate the validity of this scenario by studying the dynamic behavior of our sample under magnetic field. We will provide evidence of a modification of particles mobility during the entire experiment, from the initial viscosity drop to the slowdown caused by the formation of dipolar chains.

2 X-ray photon correlation spectroscopy (XPCS)

2.1 Basics principles of XPCS

XPCS allows us to study the dynamical behavior of materials at the 1 nm - 1µm lengthscale through successive SAXS measurements and appropriate data treatment. It is often used to characterize the evolution of hierarchical structure of the complex fluid (*i.e.*, block copolymers, colloidal gasses, gels or nanocomposites) over time. XPCS relies on the interaction of the analyzed material with X-rays. The interactions between a partially coherent monochromatic X-ray beam and a disordered material generate a speckled intensity pattern. By analyzing the temporal fluctuations of the intensity pattern, information on the material dynamics are obtained. Typically, 2D detectors are employed in order to collect in a single image the intensity pattern over a range of scattering wave vectors q at different time intervals τ as illustrated in Figure 6.5 below.

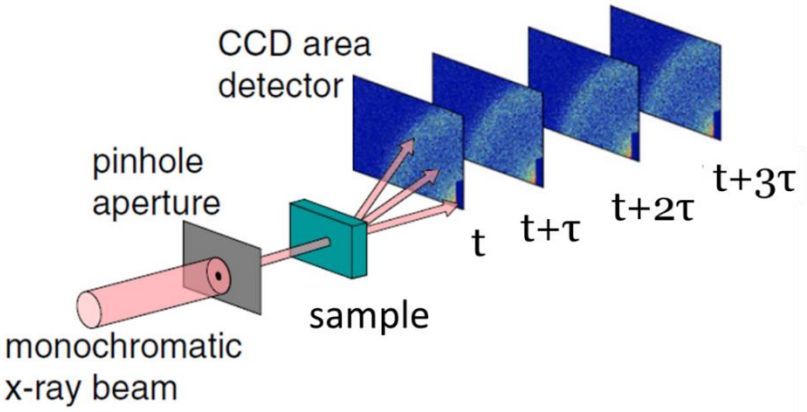

Figure 6.5: Schematic representation of an XPCS measurement. The pinhole aperture selects a coherent portion of the incident monochromatic X-ray beam, resulting in a speckled scattered intensity over a range of scattering vector collected at specific time intervals τ to perform the time autocorrelation functions. Figure adapted from [3].

The analysis of the temporal intensity fluctuation is usually carried on by focusing on the intensity autocorrelation function g_2 measured as function of the scattering vector q and time delay τ:

$$g_2(q,\tau) - 1 = B\frac{\langle I_p(q,t)I_p(q,t+\tau)\rangle_{t,\varphi}}{\langle I_p(q,t)\rangle_{t,\varphi}\langle I_p(q,t+\tau)\rangle_{t,\varphi}} - 1 \qquad \text{(VI-1)}$$

where $B \geq 1$ is a normalization factor chosen such that $g_2 - 1(\tau \to 0) = 1$, $I_p(q,t)$ is the q and time-dependent intensity measured by the p-th pixel and the brackets indicate the time average ($\langle ... \rangle_t$) and the azimuthal average ($\langle ... \rangle_\varphi$) over a ring of pixels centered around the transmitted beam position and characterized by the same magnitude of q.

The decay of the autocorrelation function, at $2\pi/|q|$ close to the typical particle size, is characteristic of the motion of particles inside the matrix and can be fitted empirically with a Kohlrausch-Williams-Watts (KWW) function [3]:

$$g_2 - 1 = exp\left(-\left({}^{t}/_{\tau_c}\right)^{\beta}\right) \qquad \text{(VI-2)}$$

where τ_c and β are the characteristic time of the decorrelation and the KWW exponent respectively. τ_c corresponds to the time for which half of the scattered X-rays are no longer correlated to the first pattern $g_2 - 1 = 0.5$. Considering the biggest Fe-n particle sizes R_p (see Figure 3.4), we have worked at $|q| < \pi/R_p$ with the highest q used in the measurement being 0.02 nm^{-1}. Note that when $\beta < 1$, we speak about a stretched exponential, often reminiscent of polydispersity effect [4] whereas when $\beta > 1$, the compressed exponential indicates the suddenness of particles motion [3, 5, 6]. Figure 6.6 illustrates examples of stretched and compressed exponentials determined through the KWW function for a given time τ_c.

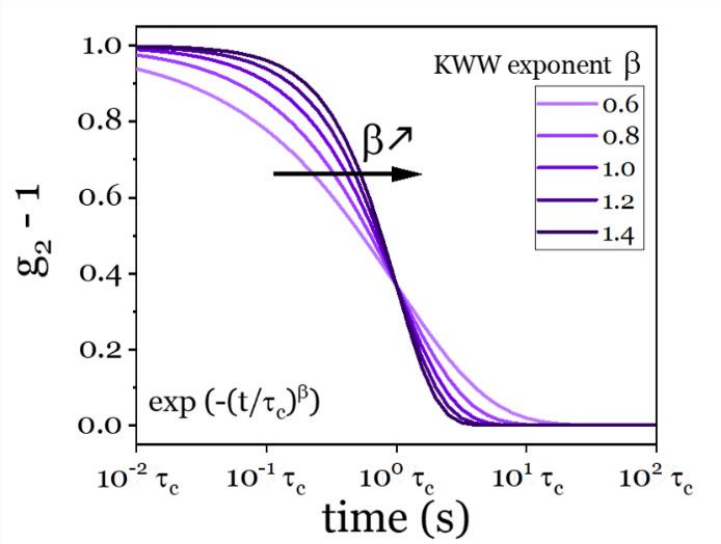

Figure 6.6: Graphical representation of the KWW function for different values of the exponent β, calculated between for times $10^{-2}\ \tau_c$ and $10^{2}\ \tau_c$.

2.2 Characterization of magnetic-field-induced sample dynamics by XPCS

To characterize particle motion, we perform a series of XPCS measurements on the 5 vol.% Fe-n composite. The first measurement is performed around room temperature, without any thermal and magnetic solicitation (see Figure 6.7). As expected from a measurement made under the material's melting point, it shows a perfect correlation (*i.e.*, with the autocorrelation function equal to 1), confirming that there is no particle motion at characteristic times lower than 100 seconds.

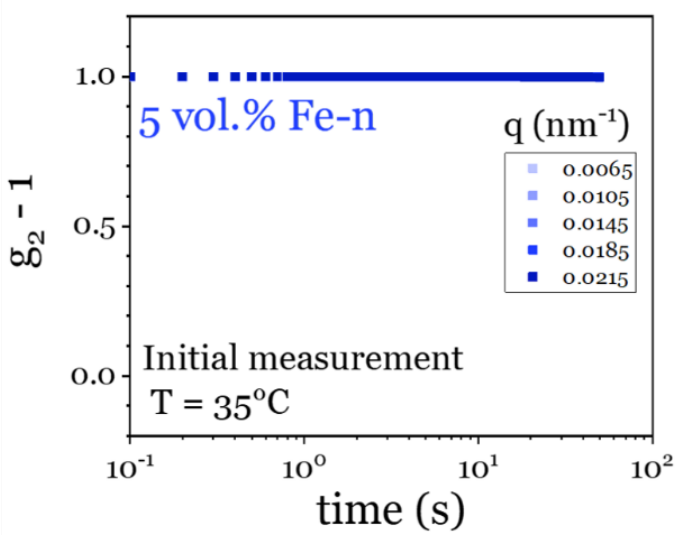

Figure 6.7: XPCS autocorrelation function measured on a 5 vol.% Fe-n composite at 35°C.

Then, a series of measurements are performed on the composite heated above its melting point (~180°C) without any magnetic field being applied. This allows us to characterize the dynamics of the nanoparticles due solely to the temperature, with the objective to have a reference when the magnetic stimulus is added. A heating stage is used to heat the sample at 180°C. The measurements were made at different q values, from 0.0065 to 0.0215 nm^{-1}, once the temperature stabilized at 180°C (*i.e.*, after 5 min).

The detected speckle image resulting from the interaction between the incident X-ray beam and the sample (see Figure 6.8A) is integrated along the vertical and horizontal direction (parallel and perpendicular to the gravity direction respectively) with an angle of ±5° to determine the two autocorrelation functions shown in Figure 6.8B. We found that the two autocorrelation functions do not superimpose as expected for an isotropic material. The reason for this behavior is to be attributed to the liquid nature of the sample when heated above the melting point. Indeed, we observed the material slowly flowing in the vertical direction, thus explaining the faster decorrelation of the $g_2 - 1$ in the vertical direction. An additional proof of the gravity-induced flow can be found in the β value (≈ 2) and q^{-1} dependence of the characteristic decorrelation time obtained from the fitting of the autocorrelation function obtained along the vertical direction (see Appendix D). In this case, the ballistic behavior is due to the gravity-induced macroscopic convective flow of the sample. As a consequence, to overcome the gravity effect in our analysis of the sample dynamics, we investigated only the scattering function obtained from the horizontal integration.

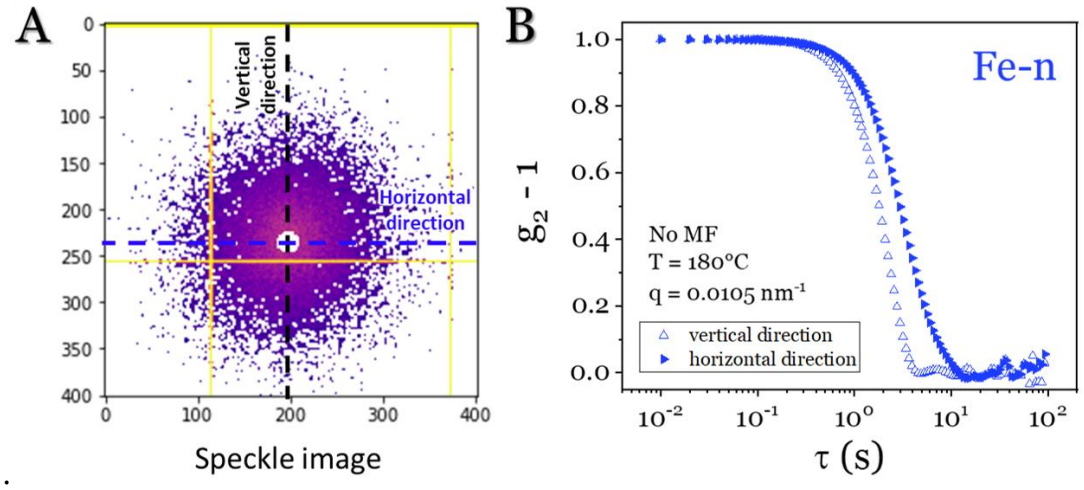

Figure 6.8: XPCS measurements. (A) Speckle image where horizontal and vertical directions (angle ±5°) used for the data integration are reported. (B) Autocorrelation function measured on a 5 vol.% Fe-n composite heated at 180 °C with a heating stage (no magnetic field).

In Figure 6.9A we report the autocorrelation functions obtained from the horizontal integration at different q values, from 0.0065 to 0.0215 nm^{-1}, while in Figure 6.9B, we show the time τ as function of q. The dependence of τ_c with q expected for purely diffusive movement (*i.e.*, Brownian motion) and for ballistic movement should display slopes of -2 and -1 respectively. [7] The dynamics obtained are indicative of an unusual behavior, with a slope of -0.66, which we believe is due to the interactions between Fe-n nanoparticles and the TPU matrix and possibly to the incomplete dissociation of the TPU matrix above T_m.

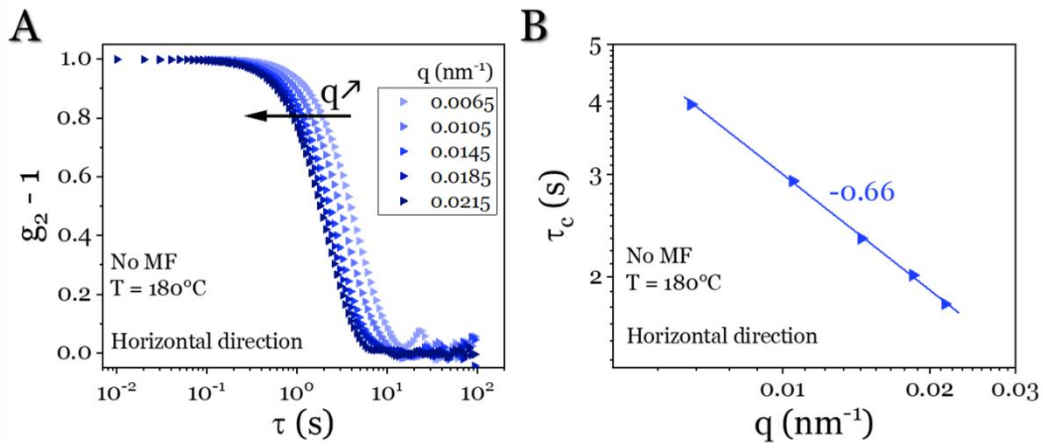

Figure 6.9: (A) XPCS autocorrelation function for different q values, measured on a 5 vol.% Fe-n composite at 180°C with no magnetic field (resistive heating). (B) Characteristic time τ_c as a function of the q.

Once characterized the dynamics of the selected composite at 180°C, we can now focus on the analog experiment in which the heat is generated by our oscillatory magnetic field instead of the heating stage. XPCS measurements are performed during the 20-min long experiment introduced in Chapter VI section 1, using the same set-up as for the SAXS measurements (see Figure 6.2) and following the temperature profile in Figure 6.3B. Based on our previous results from the time-resolved USAXS experiments, two measurements of the material dynamics at ~186°C have been considered as the most relevant ones (see the white dots in Figure 6.4B showing the time and temperature of the measurements):

- At 2 min, to study the dynamics of an evolving structure at short times, above the TPU's melting point but before reaching the dynamic equilibrium.
- At 19 min, to study the dynamics of a stable structure at long times, above the TPU's melting point.

For the short time dynamics, in the same q range (*i.e.*, 0.0065 to 0.0215 nm^{-1}), the dynamics of the nanoparticles are clearly faster (around 20 times faster than the resistive heating), with characteristic times τ_c ranging between 0.07 and 0.2 s (see Figure 6.10A). This agrees with the expected behavior of the particles at this stage, with the dynamics being strongly accelerated and mainly controlled by the magnetic field. On the other hand, dynamics, measured after 19 min) are slower, with their characteristic times τ_c between 0.54 and 2.4 s (see Figure 6.10B). Being at a dynamic equilibrium, the motion of particles is not driven only by the magnetic field. As the dynamics are closer to those of the experiments controlled with a heating stage (heating without magnetic field), we can deduce that particle motion is mostly controlled by the coupling of the effects of the magnetic field and the temperature, with the particles being close to a stable arrangement.

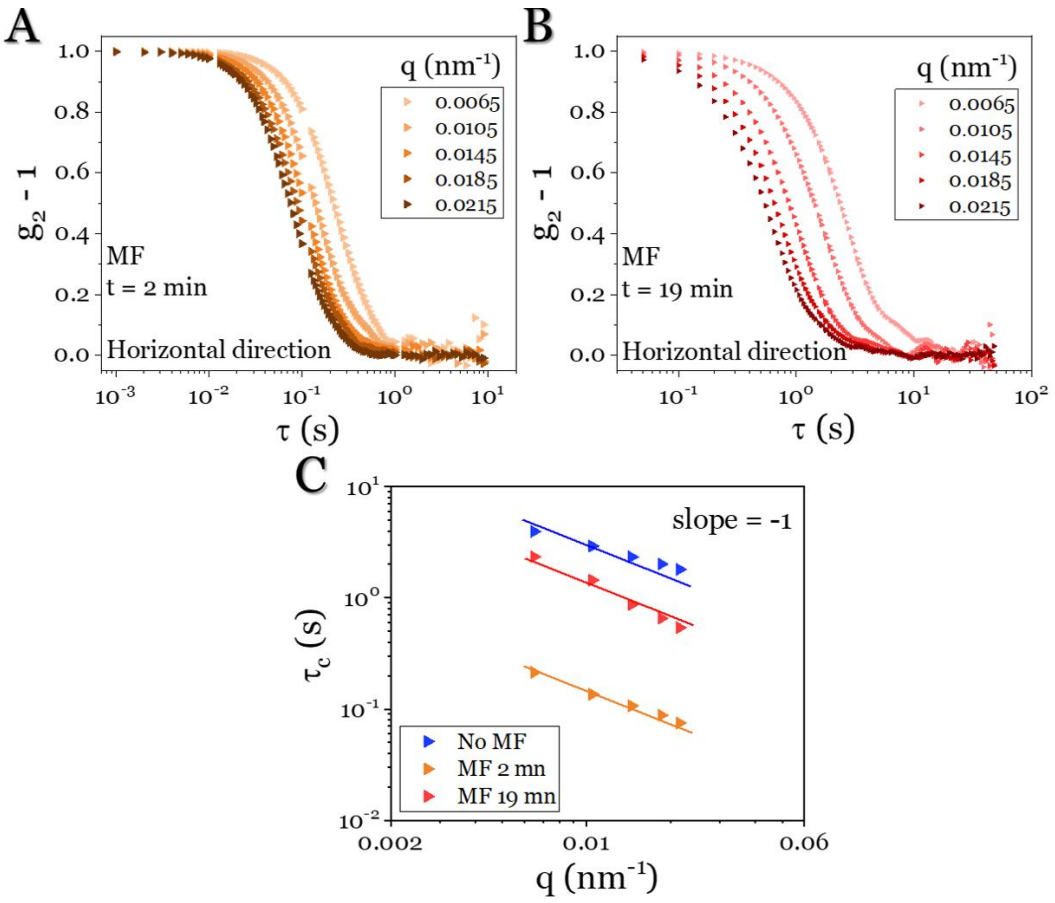

Figure 6.10: XPCS autocorrelation function q-dependence under induction heating. (A-B) Signals were measured at different q values after 2 and 19 min respectively. (C) Corresponding characteristic time q-dependences; the case of resistive heating (No MF – absence of magnetic field) is added for comparison.

This is further emphasized in Figure 6.10C, which gathers the dependence of the different characteristic times τ_c with q, for all three XPCS measurements. Slopes of -1 are added to help in comparing the different results. The test performed at 2 min, shows a variation of τ_c with a slope of -0.85 indicating a quasi-ballistic movement of particles (higher than in the heating stage case since the magnetic field drives the motion of NPs). Dipolar interactions between the nanoparticles is a driving force, which leads to nanoparticles being attracted to each other on a non-randomized manner. Conversely, the test performed at 19 min, shows a variation of τ_c with a slope of -1.2, indicative of mostly ballistic behavior. The interpretations are limited by the non-negligible polydispersity in size and the complexity of the matrix with which Fe-n particles are known to interact favorably (see DSC thermograms in Figure 3.8B).

In conclusion, the dynamics of a selected sample have been characterized through the coupling of leading technology experiments with the magnetic inductor. This experiment finally confirms our hypothesis of the origin of an additional heating mechanism appearing during the induction heating test under particular conditions. Moreover, the possibility of following the dynamics over 20 min (*i.e.*, a relatively long period of time in the scope of this thesis), allowed for a more precise understanding of particle diffusion and the creation of a dynamic equilibrium in the structure. An improvement to this experiment would be conceivable by performing similar tests on composites made with well-defined monodisperse colloids, allowing for a clearer quantification and understanding of the dynamics of magnetic particles in the composites.

References

[1] M. Suwa, A. Uotani and S. Tsukahara, "Alignment and small oscillation of superparamagnetic iron oxide nanoparticle in liquid under alternating magnetic field," Journal of Applied Physics, vol. 125, p. 123901, 2019.

[2] E. C. Abenojar, S. Wickramasinghe, J. Bas-Concepcion and A. C. S. Samia, "Structural effects on the magnetic hyperthermia properties of iron oxide nanoparticles," Progress in Natural Science: Materials International, vol. 26, p. 440–448, 2016.

[3] R. L. Leheny, "XPCS: Nanoscale motion and rheology," Current opinion in colloid & interface science, vol. 17, p. 3–12, 2012.

[4] P. A. Hassan, S. Rana and G. Verma, "Making sense of Brownian motion: colloid characterization by dynamic light scattering," Langmuir, vol. 31, p. 3–12, 2015.

[5] M. L. Ruegg, A. J. Patel, S. Narayanan, A. R. Sandy, S. G. J. Mochrie, H. Watanabe and N. P. Balsara, "Condensed exponential correlation functions in multicomponent polymer blends measured by X-ray photon correlation spectroscopy," Macromolecules, vol. 39, p. 8822–8831, 2006.

[6] A. Madsen, R. L. Leheny, H. Guo, M. Sprung and O. Czakkel, "Beyond simple exponential correlation functions and equilibrium dynamics in x-ray photon correlation spectroscopy," New Journal of Physics, vol. 12, p. 055001, 2010.

[7] E. B. Trigg, L. Wiegart, A. Fluerasu and H. Koerner, "Dynamics of Polymerization and Gelation in Epoxy Nanocomposites via X-ray Photon Correlation Spectroscopy," Macromolecules, vol. 54, p. 6575–6584, 2021.

General Conclusions

Conclusion

The primary objective of this thesis has been met by developing strong phase-changing thermoplastic elastomer composites, using commercially available components, capable of being repaired through magnetic induction. After the full structural, thermomechanical, and magnetic characterization of the magnetic composites, we were able to understand their behavior and set the conditions to be respected for magnetic induced healing to be possible. We selected the most interesting composites based on their induction heating capabilities under an alternating magnetic field for specific applications (*i.e.*, induction healing, surface treatment of 3D-printed samples).

Through structural and thermomechanical characterization (Chapter III), we understood the impact of the magnetic particles on the TPU matrix and make a preliminary selection of the composite formulations with the mechanical characteristic needed at the solid and the liquid states. The selected composites, loaded with 1-5 vol.% in magnetic particles, are capable of flowing under reasonable timescales above the TPU's melting point (relaxation time sorter than 0.01 s) while also showing a good compromise between mechanical reinforcement and appropriate deformation at failure (strain at failure above 2.0). With the thermal characterization of the composites, we defined the temperature range of interest (150 to 250 °C) to enable the flow of the material through the full melting the crystallites while avoiding polymer degradation.

For each series of magnetic composite, the predominant heating mechanisms were identified, and their corresponding heating profile was measured for the given set-up (Chapter IV). The insufficient conductivity of the composites, measured through broadband dielectric spectroscopy, proved that eddy currents are not generated during the induction heating. At the solid state, superparamagnetic magnetite (10-25 nm Fe_3O_4) composites generate heat due to magnetic relaxation losses (*i.e.*, Néel relaxation), whereas ferromagnetic iron (40-140 nm Fe-n and 40-50 µm Fe-µ) composites heat through domain wall motion (*i.e.*, realignment of magnetic domains within the particle), as expected from their respective particle sizes.

The heating profiles were remarkably insightful as they gave the first indications for the possibility of having an additional heating mechanism appearing once the melting point of the

matrix has been reached. In agreement with the individual rheological behavior of the materials at the molten state, we were able to explain the differences in temperature profiles and the appearance of the extra-heating, highly dependent on the viscosity of the TPU and its evolution during the experiment. The additional heating mechanism only appears if the composites generate enough heat to reach the TPU's melting point and if the viscosity is sufficiently low to enable heat generation through friction between the particles and the matrix. The additional heat dissipation comes from the fall of viscosity once the TPU's melting point is reached, favoring the rotation of magnetic particles that generate heat through mechanical friction.

We sought to confirm the hypothesis on particle motion during an induction heating test. This concept was studied in depth in Chapter VI through X-ray photon correlation spectroscopy at the ESRF coupling our induction heating set-up to the X-ray beamline. We studied the dynamics of magnetic particles in the matrix above the melting point. We developed a good understanding of the role of particle diffusion with time and its effect on the heat generated, confirming the observation of the additional heating mechanism and its origin. Over 20 min experiments, the structure of sample evolved at high temperature, causing alignments of particles in the direction of the magnetic field lines until the newly-formed dipolar chains prevent more mobility.

At the minimal pulse duration available, the composites with 5 vol.% in magnetic particles respond to the specifications needed for magnetic induced healing to take place, capable of reaching the melting point, while being able to flow above their melting point. While composites filled with 1 vol.% in magnetic content are also capable of flowing above the TPU's melting point, they do not generate enough heat to reach this temperature. On the other hand, composites filled with 10-15 vol.% in magnetic content, heat too fast for a reliable treatment of the material and the flow of those filled with Fe_3O_4 and Fe-n particles would be hindered by gelation effects.

Based on the previous sorting of composites, we performed the magnetic induction healing process on the magnetic composites loaded with 5 vol.% in magnetic particles (Chapter V). The mechanical recovery, through the magnetic induction healing process, was determined by comparing healed dumbbell-shaped tests samples to recycled ones. Through the optimization of the process, we found an overlap in stress-strain response even above 1.2 true strain unit and satisfactory 85% recovery of the strain at failure for the treated composites (30-100 MPa) in 45-60 s. We then illustrate the versatility of this concept can easily be extended to other thermoplastic elastomers as the solid/liquid thermal and rheological requirements are similar.

Then, our interest is focused on the use of induction heating to improve the surface of samples, through the solid-to-liquid transition, prompting the smoothening of the surface and correcting minor surface defects, while avoiding internal damage to structure. 3D-printed composites loaded with 5 vol.% in Fe-n were processed in different shapes through fused filament deposition to test evaluate the improvement of the surfaces of each piece.

Outlooks

In this work, we have shown the interest of a complete multi-physics approach in characterizing composites for magnetic induced healing, using commercially available components (both for the TPU matrix and the magnetic nanoparticles). The choice of these low-cost materials was purposely made to highlight the affordability of this technique, matching the scope of the POMMADE project funded by the Carnot Institute I@L. However, the polydispersity in size and in shape of the magnetic particles and their assembly into aggregates might hinder for a complete interpretation of the results. This is particularly true for ultra-small-angle X-ray scattering USAXS and X-ray photon correlation spectroscopy XPCS experiments. In upcoming works, we believe that the use of well-defined colloids dispersed in the TPU matrix would lead to a more reliable analysis of the response to the magnetic solicitation, through the multi-physics characterization. Moreover, the surface of such colloids could be functionalized to increase or decrease its compatibility with the matrix. It would lead to the modification of the thermal, mechanical and rheological properties of the magnetic composites and thus, their response to the magnetic stimulus.

The versatility of magnetic induction presents an advantage as the properties could potentially be tuned for different responses depending on the intended application. As proven by recent experiments on silicone-based composites, crosslinking can be triggered for their process, through magnetic induction and the ensuing heat generation. Beyond the possibility of working with other matrices, we can also produce composites with other magnetic fillers. In particular, the use of magnetic powders (Fe_3O_4), synthesized with recycled materials from the steel industry, has also brought our attention. Their incorporation would emphasize even more the "green" trend of moving towards recyclable, reusable and repairable materials by stating that the components used to make our composites are already the product of recycling.

From the industry-oriented approach, the procedures for magnetic induced healing and surface treatment could be optimized and standardized for upscaling. We can work on conceiving

different coil geometries intended to treat specific sample shapes and sizes. The efficiency of heat generation can be increased by modifying the frequency or the magnetic field amplitude applied to the sample. Another possible application for magnetic induction would be through the magneto-responsive patching of defects on a material. Once again, the development these processes would immensely benefit from the tuning of properties, as both have particular requirements in terms of rheology and mechanical response.

Appendices

Appendix A: Details on magnetic induction tuning

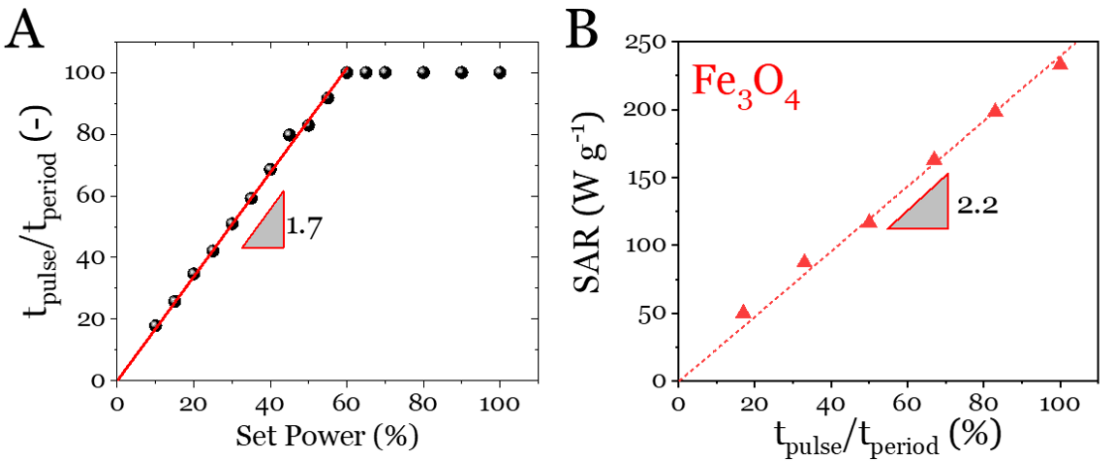

Figure A.1: (A) Ratio of the oscillating signal over time t_{pulse}/t_{period} (signal illustrated in Figure 2.14B-C) as a function of the power set on the inductor. The ratio increases linearly up to 60% in set power, at which the full signal is emitted by the magnetic inductor. (B) SAR measured (1st heating mechanism only) from a composite loaded with ca. 5 vol.% in Fe_3O_4 as a function of the t_{pulse}/t_{period} ratio.

Appendix B: Reliability of thermal infrared measurements

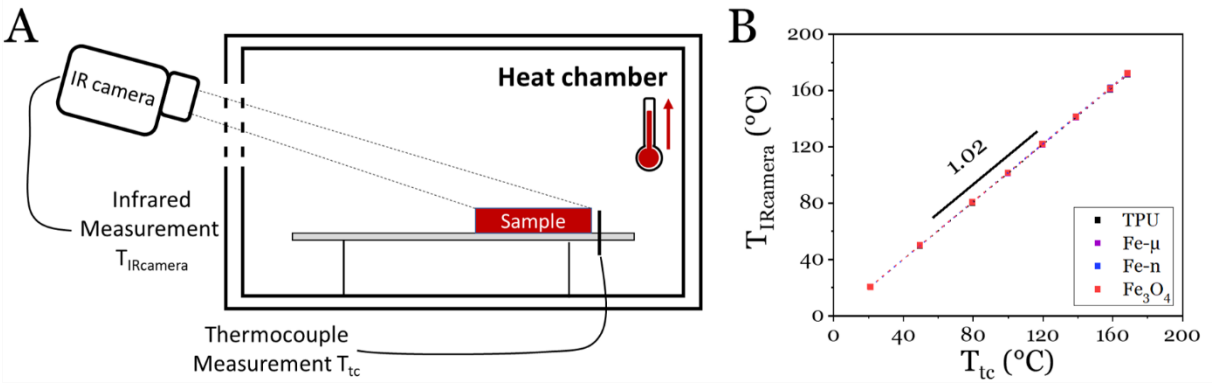

Figure A.2: (A) Schematic representation of the infrared and thermocouple measurements on samples heated inside a heat chamber with an ocular aperture. (B) Comparison between measurements taken with a thermocouple T_{tc} and with the infrared camera for the TPU matrix and composites loaded with 15 vol.% in Fe_3O_4, Fe-n and Fe-µ particles.

Appendix C: Tensile data – Reshaped, Healed I and Healed II samples

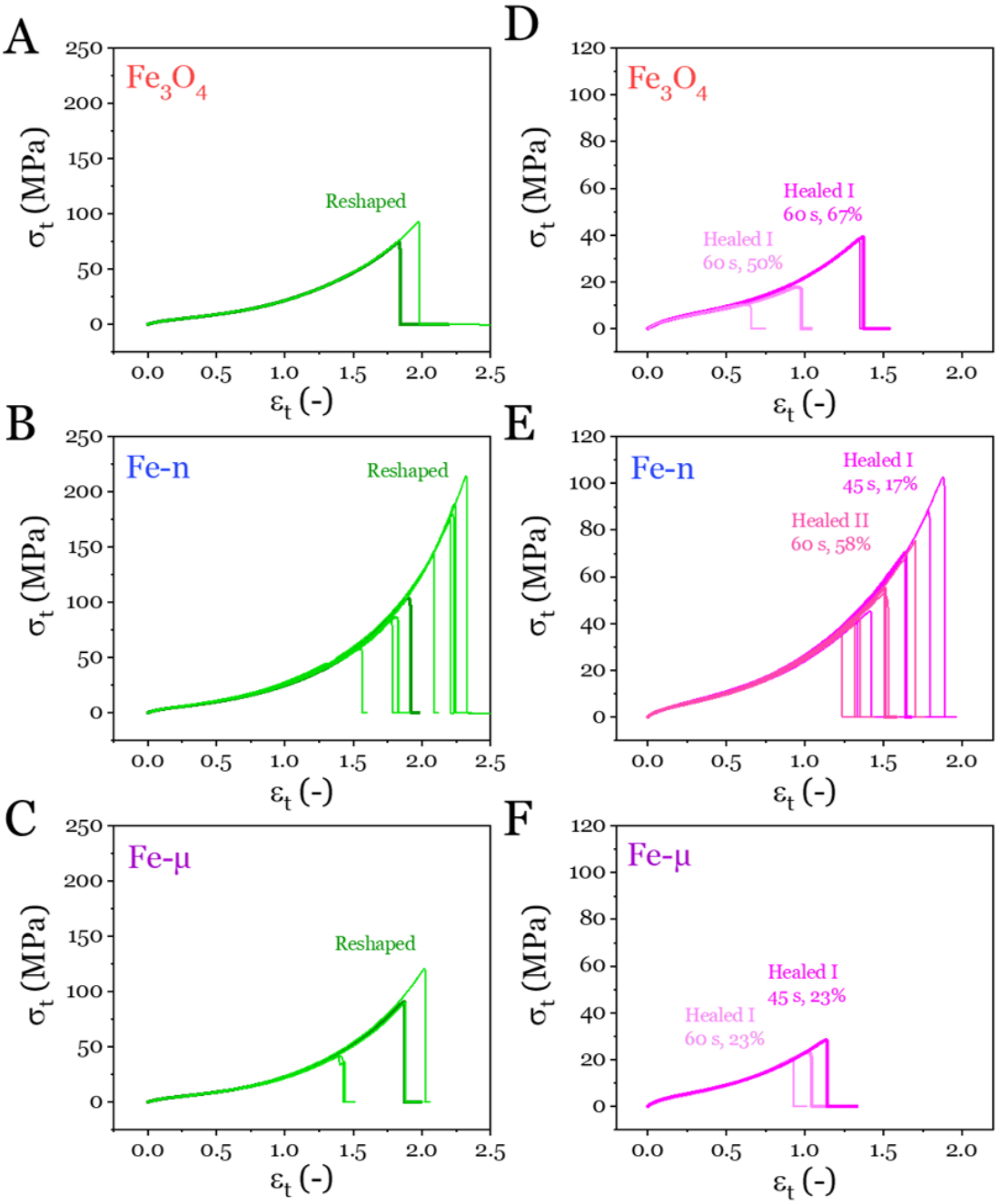

Figure A.3: (A-C) Tensile tests (true stress vs. true strain) done on "Reshaped" composite samples loaded with ca. 5 vol.% in Fe_3O_4, Fe-n and Fe-μ respectively. (D-F) Tensile tests performed on "Healed I" and "Healed II" composites loaded with ca. 5 vol.% in Fe_3O_4, Fe-n and Fe-μ respectively. Darker and thicker lines correspond to the tensile tests displayed in Figure 5.2.

Appendix D: Autocorrelation functions through horizontal and vertical directions – resistive heating

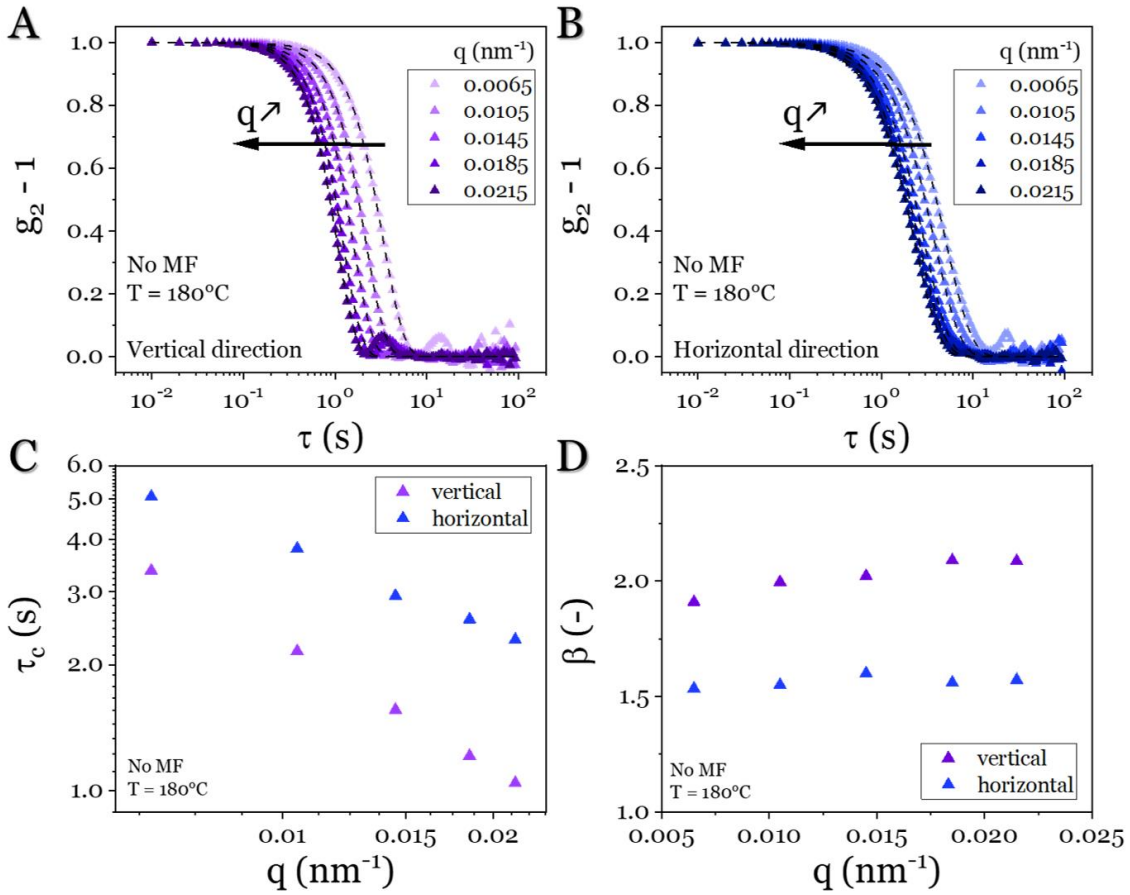

Figure A.4: XPCS measurements on a 5 vol.% Fe-n composite heated at 180 °C with a heating stage (no magnetic field). (A-B) Autocorrelation function in the vertical and horizontal directions respectively. (C-D) Characteristic time of the decorrelation τ_c and the KWW exponent β used for fitting the curves through the KWW function.

FOLIO ADMINISTRATIF

THESE DE L'UNIVERSITE DE LYON OPEREE AU SEIN DE L'INSA LYON

NOM : GRIFFITHS
(avec précision du nom de jeune fille, le cas échéant)

DATE de SOUTENANCE : 30 juin 2022

Prénoms : Pablo

TITRE : Magnetic induction healing of thermoplastic elastomer composites: multi-physics characterization

NATURE : Doctorat

Numéro d'ordre : 2022LYSEI061

Ecole doctorale : Matériaux de Lyon

Spécialité : Matériaux

RESUME :

Au cours du XXe siècle, les polymères se sont développés à une vitesse très importante, due à leur facilité de production et à leur versatilité, permettant le développement de différentes classes de matériaux suivant l'application visée. En raison de leur popularité, la production de polymères a entraîné une énorme quantité de déchets. En particulier, les élastomères vulcanisés ont récemment souffert d'une mauvaise réputation à cause de leur incapacité à être refondus ou réutilisés. Sur de longues périodes, leur dégradation mécanique se fait par des sollicitations cycliques et l'effet de l'environnement. Cependant, ils restent très largement utilisés dans plusieurs secteurs industriels en raison de leurs propriétés physiques uniques. Un défi majeur consiste donc à trouver des matériaux alternatifs capables d'être réutilisés, réparés et recyclés, répondant à des exigences très élevées en termes de module d'élasticité, de ténacité, de résistance à l'usure, de stabilité chimique et de coût.
Les élastomères thermoplastiques, basés sur des copolymères à blocs multiples, possèdent les propriétés mécaniques requises pour des applications structurelles et peuvent être réutilisés ou recyclés. La réparation de ces matériaux est possible, au-dessus de leur température de fusion, à travers la dissociation des segments rigides, qui déclenche la transition solide-liquide. Nous proposons d'atteindre cette température en chargeant une matrice élastomère thermoplastique avec des (nano)particules générant de la chaleur par induction magnétique à haute fréquence, pour un traitement thermique rapide et sans contact.
D'abord, la caractérisation multi-physique a permis une compréhension complète des mécanismes agissant sur le composite sous un champ magnétique oscillatoire. Ensuite, la capacité de réparation de ces matériaux a été évaluée, en étudiant leur comportement mécanique via des expériences de traction uniaxiale jusqu'à leur rupture. Finalement, l'optimisation du processus de cicatrisation magnétique a été effectuée afin de maximiser la récupération des propriétés mécaniques et minimiser les défauts structurels induits.

MOTS-CLÉS : élastomères thermoplastiques, nanocomposites, transition de phase, chauffage par induction magnétique,

Laboratoire (s) de recherche : MATEIS, INSA Lyon

Directeur de thèse : Sylvain MEILLE

Co-directeur de thèse : Guilhem BAEZA

Président de jury :

Composition du jury : Annette SCHMIDT, Eric BEAUGNON, Constantino CRETON, Anne-Caroline GENIX, Sylvain MEILLE, Guilhem BAEZA, Gildas COATIVY, Françoise MECHIN